

Energy Loss of Quarks by Gluon Radiation in Deconfined Matter

**Energieverlust von Quarks durch Gluonenstrahlung
in Deconfinement Materie**

Diplomarbeit
zur Erlangung des akademischen Grades
Diplom-Physiker

vorgelegt von
Ronny Thomas
geboren am 7. Februar 1978 in Dresden

Institut für Theoretische Physik
Fachrichtung Physik
Fakultät für Mathematik und Naturwissenschaften
der Technischen Universität Dresden



November 2003

Eingereicht am 27. 11. 2003

1. Gutachter: Prof. Dr. Gerhard Soff
2. Gutachter: Prof. Dr. Burkhard Kämpfer

Abstract

The induced soft gluon radiation processes of light and heavy on-shell quarks passing an amorphous colour-neutral deconfined medium are compared in a perturbative approach on tree level. Therefore the potential model of Gyulassy and Wang is applied, and its validity is numerically verified with respect to one gluon emission from single quark-quark scattering. The processes of single and double scattering with one gluon being emitted are investigated in detail by analytical and numerical means in the scalar QCD approach. Subtle dependencies on a variety of parameters are outlined and, in particular, the dead cone effect for specific kinematical situations is analysed. Comparisons to the QED situation and calculations of spinor QCD results as well as studies of different gauges are presented. The importance of destructive interferences in multiple scatterings, the Landau-Pomeranchuk-Migdal effect, can be considered in the double scattering case; numerical problems with these calculations are discussed.

Kurzfassung

Die Prozesse weicher Gluonenabstrahlung von leichten und schweren "on-shell" Quarks, die ein amorphes farbneutrales "deconfinement" Medium passieren, werden im störungstheoretischen Ansatz auf dem Niveau von "tree level" Diagrammen verglichen. Dazu wird das Potenzialmodell von Gyulassy und Wang angewandt und dessen Gültigkeit in bezug auf die Emission eines Gluons in der Quark-Quark Einfachstreuung verifiziert. Die Einfach- und Doppelstreuungsprozesse, bei denen ein Gluon emittiert wird, werden mittels analytischer und numerischer Methoden im Rahmen der skalaren QCD genauer untersucht. Dabei werden subtile Abhängigkeiten von einer Vielzahl von Parametern hervorgehoben und insbesondere der "dead cone" Effekt für spezifische kinematische Situationen analysiert. Vergleiche mit QED Situationen und Berechnungen von Resultaten mittels Spinor-QCD sowie Studien verschiedener Eichungen werden dargestellt. Die Bedeutung destruktiver Interferenzen bei Mehrfachstreuungen, der Landau-Pomeranchuk-Migdal Effekt, kann im Fall der Doppelstreuung betrachtet werden, wobei numerische Probleme mit derartigen Berechnungen diskutiert werden.

Contents

1	Introduction	7
2	Energy Loss of Partons and the Search for the Quark-Gluon Plasma	11
2.1	Motivation	11
2.1.1	Theoretical Concepts	11
2.1.2	Experimental Situation	14
2.2	Dead Cone Factor	16
3	Radiation of Fast Particles Passing an Amorphous Medium	19
3.1	Classical Electromagnetic Radiation	19
3.1.1	Landau-Pomeranchuk-Migdal Effect	19
3.1.2	Ter-Mikaelian Effect	23
3.2	Quantum Description: Cross Section and Radiation Amplitude	24
3.2.1	General Cross Section	25
3.2.2	Radiation Amplitude	25
3.3	The Potential Model	27
3.4	Divergences	27
4	Single Scattering with One-Gluon Emission	29
4.1	Kinematical Situation and Declarations	29
4.2	Radiation Amplitude in QED	36
4.3	Radiation Amplitude in QCD	40
4.3.1	Abelian Diagrams	41
4.3.2	Non-Abelian Diagrams	43
4.4	Elastic Factorisation and Non-Abelian Contributions	50
4.5	Potential Model versus Quark-Quark Scattering	59
4.6	Summary	63
5	Double Scattering with One-Gluon Emission	65
5.1	Elastic Scattering	65
5.1.1	Integration in Cylindrical Coordinates	66
5.1.2	Integration in Spherical-like Coordinates	67
5.2	Inelastic Scattering	67
6	Summary and Outlook	71
	Appendix	72

A	Remarks on Colour Algebra	73
B	Feynman Rules	77
C	Gauge Invariance	79
C.1	General Restrictions	79
C.2	Tests of Gauge Invariance	80
C.2.1	Gauge Invariance for Polarization Vectors	80
C.2.2	Gauge Invariance for the Gluon Propagator	82
C.3	Polarization Matrix	86
D	Gunion-Bertsch Limit	91
D.1	Elastic Scattering	91
D.2	Inelastic Scattering	93
D.2.1	Single Contributions to Gluon Radiation	93
D.2.2	Total Matrix Element	98
E	The C++ Program	101
F	Conventions and Notations	105
G	Dead Cone Factor for Arbitrary Angles	107
H	Scalar versus Spinor Calculation	109
	Bibliography	113

1 Introduction

Nuclear matter in ground state is built up from nucleons, two sorts of hadrons, protons and neutrons, whose interaction is dominantly determined by the strong interaction. The fundamental theory which describes this strong interaction on the level of quark and gluon degrees of freedom is Quantum Chromodynamics (QCD). It is based on the existence of constituent elementary particles, the quarks, which are assumed to exist as six different types. These so-called flavours in increasing order of the current mass parameter are the up, down, strange, charm, bottom and top quarks. They carry different electromagnetic charges and are fermions with spin $\frac{1}{2}$. In contrast to the electromagnetic analogue Quantum Electrodynamics (QED), this theory is a non-abelian gauge theory expressed by colour charges which are not only assigned to the quarks but also to the corresponding exchange particles. These gauge bosons are called gluons and can interact with each other, contrary to photons in QED. Quarks and gluons all together are often termed partons. Quarks have not been found isolated but always bound in colour-less combinations in hadrons, either as quark-antiquark pairs $q\bar{q}$, these are mesons, or confined in three quark states as baryons qqq , which include the proton and the neutron.¹

Under conditions of high temperatures or high densities strongly interacting matter is proposed to appear in new phases. This is shown in Fig. 1.1 where the proposed QCD phase diagram is sketched depending on the temperature T and the baryon chemical potential μ . The conditions required to explore such regions in the laboratory are only realized in collisions of heavy ions at relativistic velocities, whereby these situations are comparable to the early stages of the history of the universe, that means shortly after the Big Bang. Cold dense hadron matter is relevant for neutron stars.

In the course of relativistic heavy-ion collisions in the centre of mass frame (CMS) the colliding nuclei are Lorentz-contracted in their direction of motion. In high energetic collisions the individual constituent nucleons are resolved in partons which scatter and deposit a considerable amount of energy in the mid-rapidity region with respect to the beam axis $y \sim 0$.² This energy density corresponds to a particular temperature assuming thermalization takes place at a sufficiently short time scale.

With rising temperature of strongly interacting matter one expects quarks and gluons to become the relevant degrees of freedom instead of hadrons. Following the situation for electrons and photons in QED such a deconfined phase is usually called the quark-gluon plasma (QGP). The transition is expected at a critical temperature of $T_c \sim 170$ MeV, however it is not yet clear how this transition, shown as "cross-over shape" in Fig. 1.1, would behave.

Due to a remaining intrinsic longitudinal motion of the matter's constituents and the large pressure of the strongly interacting matter, after a stage of maximum density the system expands. Because of this expansion a supposed plasma state subsequently cools down below T_c and hadrons are formed (this is the chemical freezeout), due to further expansion thermal equilibrium cannot

¹Currently the pentaquark is a highly discussed exotic baryon state, e.g. [Hic03].

²The reader may refer to Eq. (C.14) for a definition of rapidity.

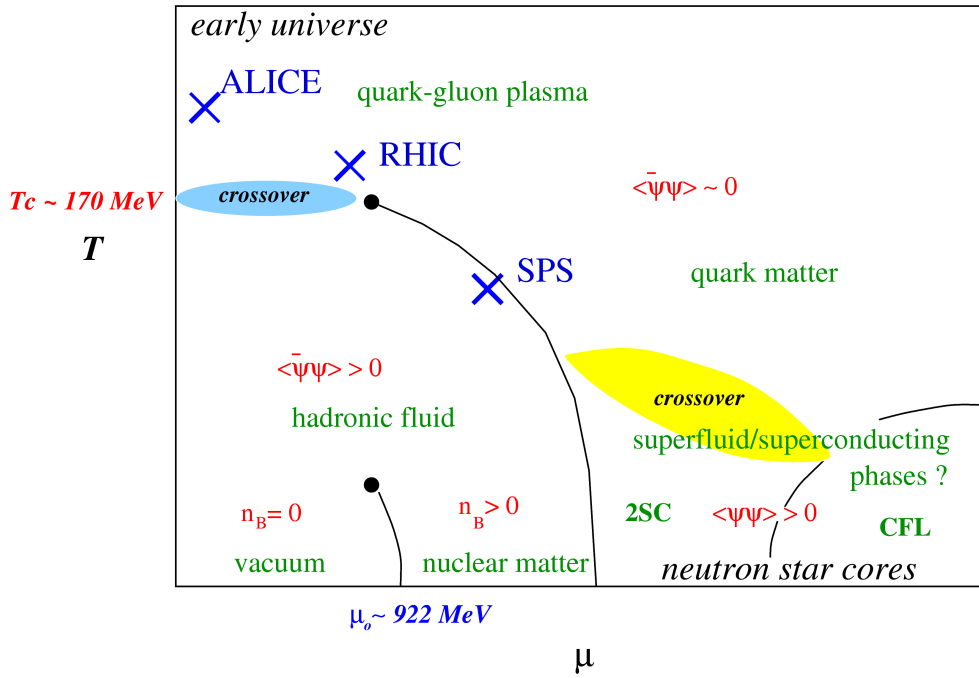


Figure 1.1: The proposed QCD phase diagram taken from [Han01].

be maintained (this is the thermal freezeout), and afterwards the hadrons move away and can be detected individually.

Besides the denotation of different phases, phase transition lines and critical points in Fig. 1.1, the expectation value of $\bar{\psi}\psi$ is additionally displayed. Chiral symmetry, the symmetry with respect to left- or right-handness of the quarks, is spontaneously broken in nuclear matter, thus a large value of the chiral condensate $\langle \bar{\psi}\psi \rangle$ accounts for the considerably higher dynamically created constituent masses of quarks. The smaller current masses of quarks are the relevant parameters if the quarks become the degrees of freedom since chiral symmetry is believed to be restored for high temperatures and densities, expressed as $\langle \bar{\psi}\psi \rangle \sim 0$ for negligible masses of the up and down quarks $m_{u,d} \rightarrow 0$. The phenomena deconfinement (quantified by the expectation value of the Polyakov loop) and chiral symmetry restoration are in QCD related and happen at the same temperature. The proposed phase diagram contains some more possible phases, superfluid or superconducting phases and quark matter, but since these are not important for our problem they are not discussed here. For more details on the phase diagram we refer the interested reader e.g. to [Han01].

It is worth emphasising that relevant heavy-ion collision experiments are marked by crosses in the proposed phase diagram for QCD in Fig. 1.1. As indicated above in order to investigate the QCD phase diagram, especially the deconfinement transition as well as chiral symmetry restoration, strongly interacting matter is explored at high energy densities. The first of such experiments were carried out at the Alternating Gradient Synchrotron (AGS) in Brookhaven and at the Super Proton Synchrotron (SPS) at CERN. More promising experiments with ultra-relativistic heavy-ion collisions currently being performed at the Relativistic Heavy Ion Collider (RHIC) at Brookhaven National Laboratory, New York, and planned at the Large Hadron Collider³ (LHC) at CERN, Geneva,

³This is denoted by the ALICE (A Large Ion Collider Experiment) detector in Fig. 1.1.

will provide data which allow the search for deconfined matter.⁴ Therefore it is of great importance to fully understand the hadronic processes but also to predict modifications of hadronic observables which arise if deconfined matter was created. There is a long list of possible observables which are sensitive to the transient creation of QGP [QM02, Won94]. We mention here modified flow patterns, di-lepton signals, J/Ψ suppression and energy loss [QM02]. The latter one is related to the focus of the present thesis.

The basic physical idea behind this problem is that in case deconfined matter was produced in a heavy-ion collision, partons with large transverse momentum with respect to the collision axis propagate through the medium and therefore can be used to probe the created phase. One believes radiative energy loss to be an important mechanism for modifications of the high energetic parton. This is outlined in more detail in Chapter 2.

In this thesis we focus on very basic scattering processes accompanied by gluon radiation of a quark passing a deconfinement phase which might subsequently alter the results of the hadronization. Considerable attention is paid to the different gluon emission patterns for light or heavy quarks.

The thesis is organised as follows. In Chapter 2 we introduce how the search for the quark-gluon plasma is connected to hadron spectra from high-energy heavy-ion collisions. The problem of parton energy loss by induced gluon radiation and its consequences for hadronic observables have been studied extensively, so that different approaches are available and will be summarized. With [Kov03, Gyu03] one can find comprehensive review articles and a considerable amount of additional references about these studies. The problem of radiation from heavy quarks is motivated.

Aspects of the radiation off fast particles traversing an amorphous medium are discussed in Chapter 3 where we focus on electrodynamics. Further the quantity "radiation amplitude", which is an important subject of our investigations, is introduced. Finally the potential model of Gyulassy and Wang [Gyu94, Wan95] is specified.

The results for the radiation pattern obtained numerically for the single scattering case are presented in Chapter 4. Especially we compare results from QED to different contributions from QCD. As particular point we mention our treatment of induced radiation. The previous work (cf. [Kov03, Gyu03]) treats the corresponding evaluation of matrix elements for the radiation process by analytical means, thereby resting on several approximations. In contrast to this, we evaluate diagrams from the very beginning by a numerical procedure. In doing so we can exactly account for the kinematics, in particular in treating finite energies and quark masses; the full colour structure is included. The present thesis is to be understood as a first exploratory study of the evaluation of Feynman diagrams within QCD relevant for energy loss. Our numerical code for this evaluation is written in C++. The idea for such a treatment of matrix elements emerged from the studies in e.g. [Tit99, Bar01], where hadronic processes are described by such a large number of diagrams which prevents the usual calculation of squared matrix elements by trace theorems. Analogue techniques are implemented, for instance, in [Kra02].

Afterwards in Chapter 5 the case of double scattering is discussed. Problems which arise in the numerical approach are explained. The last Chapter 6 is summary and outlook. Apart from this some results are referred to appendices together with descriptive supplements.

⁴Typical energies available in CMS in collisions with S, Pb or Au ions are 2 AGeV for AGS, 18 AGeV for SPS, 200 AGeV at RHIC and 5500 AGeV at LHC. Here, A stands for the nucleon number.

2 Energy Loss of Partons and the Search for the Quark-Gluon Plasma

2.1 Motivation

In the search for the quark-gluon deconfinement phase a variety of different signals has been suggested which might give information about this phase and especially should help to identify such a state experimentally. In this work we concentrate on the problem of energy loss by gluon radiation off quarks passing an amorphous medium. More precisely, the question how the mass of an on-shell quark modifies such emission processes will be the subject of investigation. In the following chapter these ideas are further motivated.

2.1.1 Theoretical Concepts

Unlike in QED the energy loss of a parton is not measurable directly since partons are not observed as free particles in the experiment. Moreover one has to question the effect of parton energy loss on subsequently built hadrons, that means on jet formation and properties which are experimentally accessible.

It is generally believed that at RHIC or LHC energies nucleus-nucleus collisions will reveal new physics compared to proton-nucleus or proton-proton collisions due to the significant size proportional to $A^{1/3}$ of the incident particles. Deviations from geometrical scaling of various observables, that means a violation of scaling from proton-proton collision to the collision of two nuclei by the number of binary nucleon-nucleon pairs, evidence this fact. This can be used to access properties of the deconfined matter, e.g. parton densities.

Among non-linear modifications of QCD evolution equations due to higher partonic density, initial state partonic energy loss, medium modifications and multiple independent hard parton interactions in one hadron collision, final state partonic energy loss is expected to modify high p_{\perp} ¹ observables which offer a link to characterize the details of matter produced in a collision. In particular the effect that the yield of produced hadrons in an ultra-relativistic heavy-ion collision is suppressed with respect to the yield scaled from nucleon-nucleon collisions is also called "jet quenching" and was already proposed as signal for high density matter about ten years ago, see e.g. [Wan92]. For a short summary of the underlying physics we refer to [Bai03].

Induced radiative energy loss has been suggested as more important effect in nuclear collisions than elastic scattering, see e.g. [Gyu03]. Note that elastic final state energy loss has been already proposed by J.D. Bjorken in 1982 to lead to jet attenuation or even extinction; others have suggested

¹The momentum $p_{\perp} \equiv p_T$ is the transverse momentum of observed particles measured perpendicular to the heavy ion collision axis.

di-jet acoplanarity as further consequence, see [Gyu03] and references therein. The corresponding experimental situation is described in 2.1.2.

Because of the high multiplicity of produced hadrons, jets contain not only the leading particle but also particles from radiated gluons, this is why a direct measurement of the energy loss effect is difficult to isolate. Instead, an analysis of particle distributions within a jet turns out to be more accurate. The fragmentation is assumed to occur in the vacuum, hence the energy loss of the parton is reflected in the energy loss of the hadron.

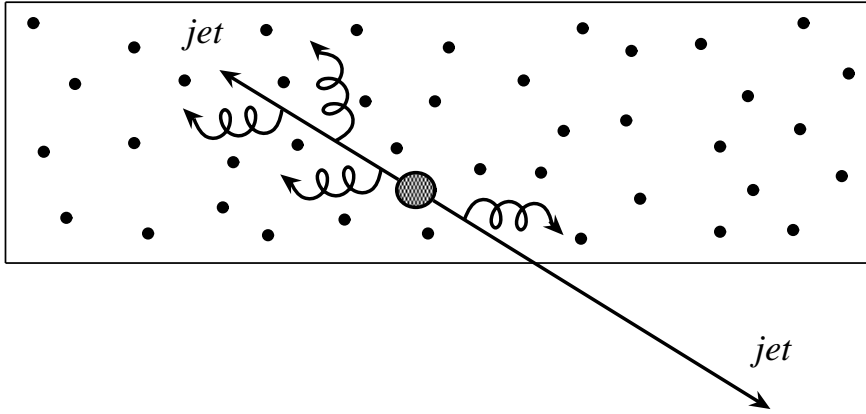


Figure 2.1: A di-jet (e.g. $\bar{q}q$) is created in a primary hard collision of two gluons. Briefly afterwards, softer interactions produce the QGP through which the jets move. The jet going a longer distance through the medium can experience a stronger attenuation or even may be extinguished. In this picture the latter case of an away-side missing jet is shown.

The parton energy loss can produce a pattern of jet attenuation, which includes information on the initial effective gluon rapidity density dN_g/dy if local thermal equilibrium is assumed. Therefore the idea of jet tomography [Gyu02b] is to reproduce quenching data selecting the most appropriate dN_g/dy distribution. Basically this is the direct analogue to conventional X-ray tomography. The energy loss effect might even lead to partial absorption of jets, that means to an so-called away-side missing jet, see Fig. 2.1.

Note in addition that parton energy loss cannot only lead to the suppression of high p_T hadron yields but can also generate azimuthal anisotropy of large p_T spectra in non-central collisions. This is a geometrical effect caused by the azimuthal dependence of the distance that a parton has travelled before hadronization. Consequently, the energy loss of this parton is a function of the azimuthal direction and so the large transverse momentum spectra of observed hadrons will be as well [Wan01a, Gyu01b].

Aside from this, jet imbalance or acoplanarity is expected [Bla86, App86]. In a collision where two opposite jets propagate outwards from the collision zone their momenta would be confined to a plane. However, because of parton energy loss of the jet particles, an imbalance of the transverse momenta can occur.

To make the problem of radiative energy loss of a jet parton easier treatable a potential model was introduced by Gyulassy and Wang [Gyu94, Wan95], explained in more detail in Section 3.3. This

model has been applied to the problem of final state radiative energy loss and discussed within several theoretical approaches. We present some of their key ideas and summarize crucial differences.

Two different analytic limits have been considered in the literature. Both apply the high-energy limit, where no deflection of the initial parton is assumed. These approaches essentially differ in their assumptions for the density of the deconfinement medium. The effect of the density can be encoded in the mean number of scatterings of the jet in medium or also termed the opacity $\bar{n} = L/\lambda$, where L is the size of the traversed medium and λ denotes the average mean free path of the parton.

A continuous theory which may be applied for dense deconfined matter, hence $\bar{n} \gg 1$, has been considered by Baier, Dokshitzer, Mueller, Peigné and Schiff (BDMPS) [Bai97a]. Based on asymptotic energy the solution of a Schrödinger like equation led to the conclusion that the energy loss ΔE grows with the medium thickness L as L^2 independent of the initial energy. This result is achieved for a static medium, however it was investigated further that in matter expanding according to Bjorken's hydrodynamical model energy loss can be even larger [Bai98a]. Note, that this ansatz has not been proven to be successful in realistic nuclear collision scenarios. There one finds that the jet parton suffers only a few scatterings (see also Section 2.1.2).

In contrast an approach for such thin media, an expansion in the opacity, has been worked out by Gyulassy, Levai and Vitev [Gyu00a] in the high-energy eikonal approximation. That means assuming a parton which remains on a straight-line trajectory it is possible to evaluate all relevant diagrams for an arbitrary number of elastic and inelastic interactions recursively. On the level of probabilities this recursion is carried out via a reaction operator. Details of this reaction operator approach, which is frequently called the GLV formalism, can be found in [Gyu00a, Gyu01, Gyu02a]. We emphasize that this approach is capable to include kinematical constraints and involves the interference effects with the production amplitude of the parton. This restricts a direct comparison of this approach with our results, since interference effects with the production process will not be studied here.

In combination with the LPM effect, explained in Section 3.1.1, which reduces \bar{n} to a smaller number of effective scatterings, the first order of the opacity expansion plays a very important role for the general question of radiative energy loss. The rapid convergence of the opacity expansion allows to reproduce the L^2 dependence of the energy loss from first order in opacity [Gyu00b]. The prediction of the GLV formalism in first order opacity is

$$\Delta E_{\text{GLV}}^{(1)} = \frac{C_R \alpha_s}{N(E)} \frac{L^2 \mu^2}{\lambda_g} \log \frac{E}{\mu},$$

where C_R is a colour factor, α_s the strong coupling constant, μ the Debye screening mass, λ_g the mean free path of a gluon, E the initial energy of the parton and $N(E)$ a numerical factor which decreases with higher energies and approaches the asymptotic value $N(E) \rightarrow 4$ for $E \rightarrow \infty$ [Gyu00b]. Hence the relative energy loss is predicted to be slowly decreasing proportional to $\log(E)/E$ for higher initial energies. For finite energies however $N(E)$ suppresses this behaviour. This shows the importance of finite kinematical boundaries and suggests that numerical approaches can be very instructive. Note that Wiedemann has independently developed an opacity expansion [Wie00b]. A path integral approach was first worked out by Zakharov [Zak98].

The QCD analogue of the TM effect, see also Section 3.1.2, was considered in [Mül99, Käm00] and [Djo03b]. In the last-mentioned work it was pointed out that a modified dispersion relation of the gluon may be the reason for a reduction of energy loss of high momentum charm quarks.

Another feature of this problem is that energy loss and energy gain mechanisms can compete with each other. The concept of detailed balance was discussed by Wang and Wang [Wan01b]. Especially hadron spectra for transverse momenta $p_T < 2 \text{ GeV}/c$ are influenced by the collisional energy gain [Mül03].

In the eikonal approximation, possible for high projectile energies, it was assumed, that the independently propagating partons only acquire a phase while they interact with a target. They do not change their transverse position and thus maintain on a straight-line trajectory. This strong assumption is not necessary for a numerical analysis at lower energies.

2.1.2 Experimental Situation

High transverse momentum spectra of pion production in Au + Au collisions at $\sqrt{s_{NN}} = 130$ GeV at RHIC reveal a steeper slope in central collision data than for peripheral collisions, see Figs. 2.2, for moderate high p_T neutral pions, i.e. $p_T \approx 1.5 - 4.0$ GeV/ c . This was discussed in [Lev02] with preliminary PHENIX data.² Using the GLV formalism it was found in [Lev02] that the quenching effect on the pion yields in central collisions can be explained by an opacity $L/\lambda_g \sim 3 - 4$ for a static deconfined medium. As mentioned above, here L is the size of the medium and λ_g is the mean free path of the gluon, which enters since gluon rescattering diagrams become important.

In general the pion yields in central collisions are suppressed with respect to $p + p$ data scaled with the number of binary collisions, which points to strong medium effects. This is interpreted

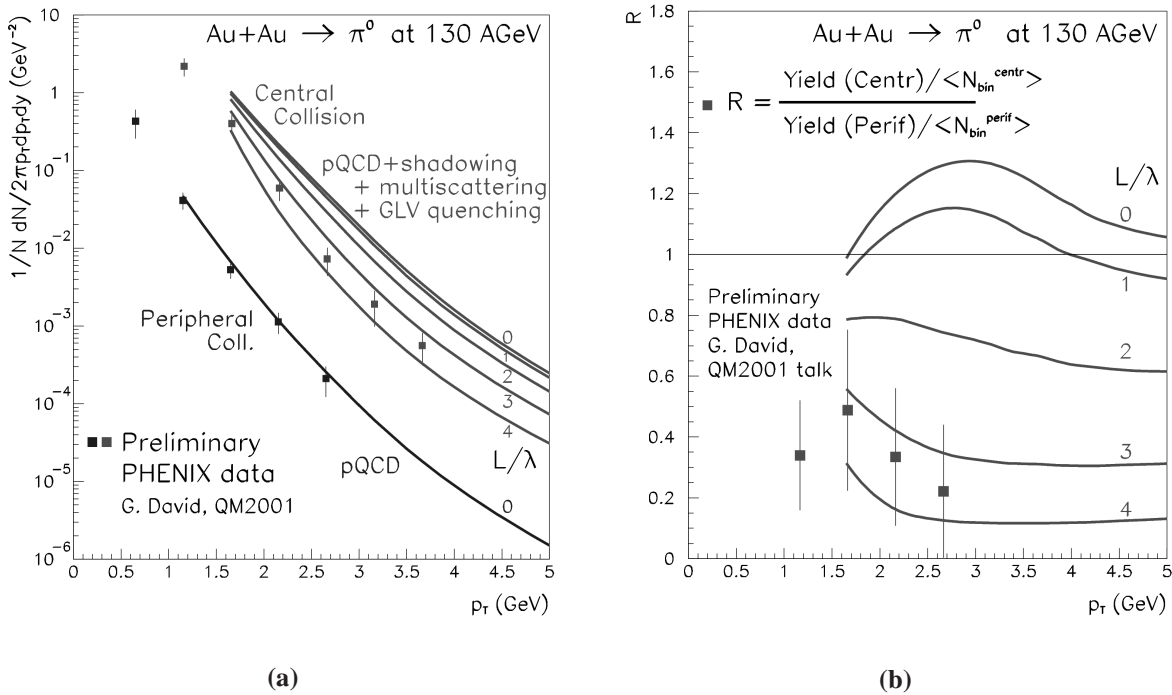


Figure 2.2: Transverse momentum spectra (a) of π^0 produced in Au + Au collisions. For central collision data the predictions including jet quenching for different values of opacity are exhibited. The central collision data show a steeper fall-off than in peripheral collisions. This is the observed jet quenching. The normalized ratio of central to peripheral pion yields (b) reveals the jet quenching in central collisions. These figures, taken from [Lev02], indicate an opacity $L/\lambda_g \sim 3 - 4$.

as jet quenching, that means a higher energy loss prior to hadronization due to the higher density formed in central collisions. These observations are also confirmed by more recent neutral pion

²The final data are published in [Adc02a].

production data from RHIC for $\sqrt{s_{NN}} = 200$ GeV [Adl03] as can be seen in Fig. 2.3. In this figure different centrality selections are compared and reveal that jet quenching is stronger if the collisions are more central. Note in addition that jet quenching has also been observed for charged hadrons, see e.g. [Adc03] for results of p_T dependent charged hadron suppression at RHIC for energies $\sqrt{s_{NN}} = 130$ GeV.

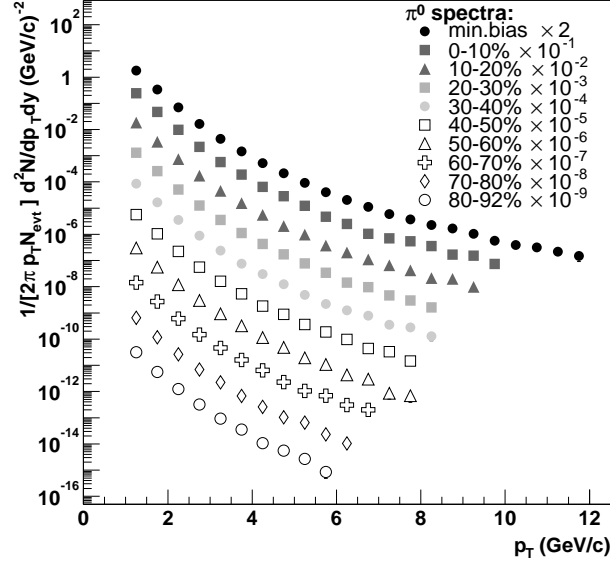


Figure 2.3: π^0 spectra as a function of transverse momentum for different centralities in Au + Au collisions at $\sqrt{s_{NN}} = 200$ GeV. This figure taken from [Adl03] exhibits that jet quenching increases with centrality.

The observation of disappearing away-side jets is a qualitative new phenomenon compared to $d + A$ collisions. The missing jet is interpreted as caught by a created deconfined phase of quarks and gluons that has a higher stopping power than nuclear matter. This was already shown in Fig. 2.1.

Data of transverse momentum spectra from semileptonic decays of open charm, $D \rightarrow e^- X$, reveal information on p_T spectra of D -mesons (charmed mesons) and thus for charm quarks, see Fig. 2.4. Surprisingly no significant energy loss is realized for charm quarks. This was termed "null effect" by Gyulassy [Djo03a]. An analysis of these data with respect to the strength of the possible energy loss effect by the charm quark seems to point at best to tiny energy losses [Gal03].

The important influence of the quark mass on the energy loss pattern, that is to say the qualitative difference between results for heavy or for light quarks due to the so-called dead cone suppression, has been discussed by Dokshitzer and Kharzeev [Dok01] and is introduced in the next section.

This interpretation of data and the theoretical prediction of the dead cone suppression motivate us to reconsider the gluon radiation spectra in the potential model in detail. This is done numerically and allows especially to abandon the high-energy limit, massless partons and the soft radiation assumption. Furthermore all non-abelian diagrams and all interferences, except interferences with the radiation amplitude, are included.

Encouraged by the suggestions from experimental data and theory that only few final state interactions are relevant, which points to the case of thin media, we will focus on single and double scattering processes using a C++ program, which had to be written.

Advantages of this method are further that the full colour algebra can be dealt with, in contrast to the assumptions which use combinations of colour structures from different diagrams in the eikonal

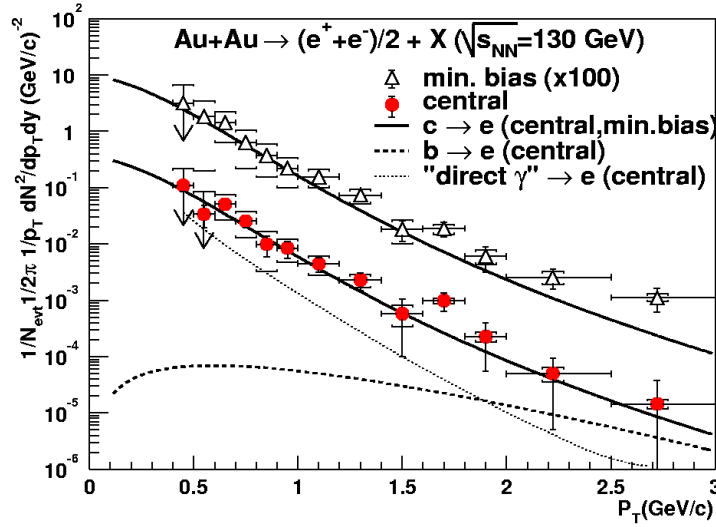


Figure 2.4: Electron spectra compared to the expectations from open charm decays. Shown are data for central and minimum bias collisions. The figure is taken from [Adc02b]. Following the analysis of these data [Gal03] suggests at best tiny energy losses of charm quarks.

limit. Besides this the calculations can be carried out for scalar but also for spinor quarks to elucidate the importance of spin flip effects.

2.2 Dead Cone Factor

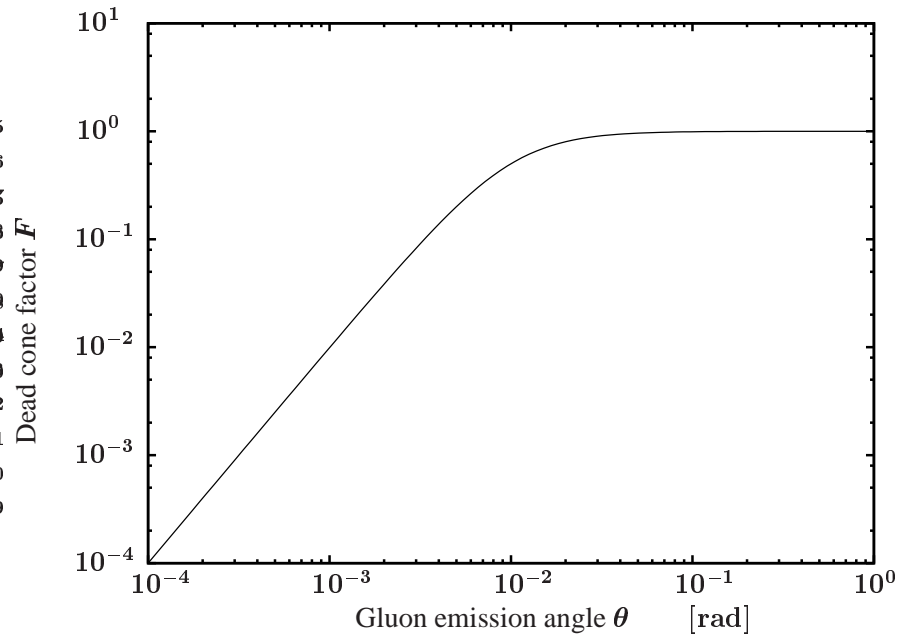
The probability for gluon emission off heavy quarks in projectile direction can be strongly reduced at angles $\theta < \theta_0$ by a suppression factor which corrects the matrix elements derived in the approach of Gunion and Bertsch [Gun82] for massless, high energetic quarks, see also next sections and Appendix D. Here $\theta_0 = m/E$ where m indicates the mass and E the energy of the incident heavy projectile quark. This factor was determined by Dokshitzer and Kharzeev [Dok01] for small angles as

$$F = \frac{k_{\perp}^2}{k_{\perp}^2 + \omega^2 \theta_0^2} = \frac{\sin^2 \theta}{\sin^2 \theta + \theta_0^2} \quad (2.1)$$

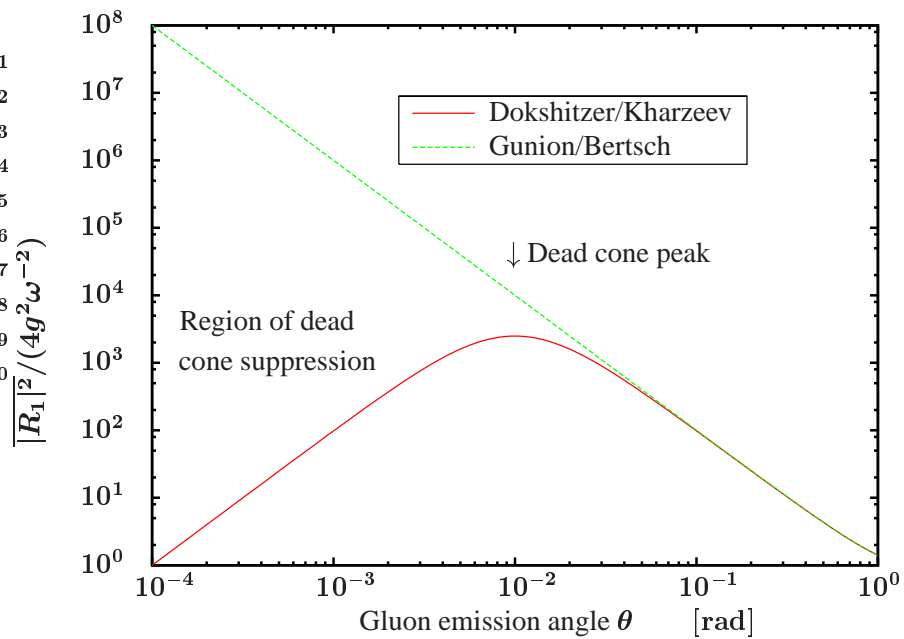
and is termed "dead cone factor".³ Its general form is depicted in Fig. 2.5. Dokshitzer and Kharzeev [Dok01] have estimated that the gluon radiation pattern differs qualitatively for heavy and light quarks. However, their discussion is restricted to small angles and the relevant angular regions are not specified quantitatively. Moreover, this estimate is valid for soft gluons, that means it focuses on abelian diagrams only, and cannot handle intermediate gluon energies. These shortcomings can be analysed only by a numerical computation, which is the main motivation for the present work.

Figure 2.5(a) shows the dead cone factor F itself. In order to motivate the terminology, which will be referred to in our further analysis, we depict the angular dependence of the squared radiation amplitude $|\overline{R}_1|^2$. Qualitatively this quantity describes the probability of gluon emission and this probability has to be multiplied by the dead cone factor if mass effects are taken into account. In Fig. 2.5(b) the consequences of the factor F are compared to the results by Gunion and Bertsch

³In Appendix G more explanations on the derivation of the "dead cone factor" are given.



(a)



(b)

Figure 2.5: Illustration of the (a) general form of the dead cone factor F as a function of the emission angle θ for $\theta_0 = 0.01$. Multiplied by the typical $1/\sin^2 \theta$ radiation pattern for massless projectiles (b) reveals the suppression of emission off heavy particles compared to Gunion and Bertsch [Gun82], which equals the term $\sin^{-2} \theta$, and suggests the sketched terminology.

[Gun82] restricted to the θ dependence. Therefore the typical $1/\sin^2 \theta$ dependence of the radiation amplitude, see Appendix D, is multiplied by F^2 , since the squared matrix elements are relevant. Hereby the so-called dead cone peak is situated at θ_0 and implies to denote θ_0 as dead cone angle. Below θ_0 , the characteristic angle in this problem, radiation becomes suppressed due to the non-vanishing mass of the projectile.

3 Radiation of Fast Particles Passing an Amorphous Medium

Following the previous motivation of energy loss off quarks by induced gluon radiation in deconfined matter of quarks and gluons we focus on important aspects of radiative energy loss from an electromagnetic point of view. Finally we show how the radiation from light and heavy quarks can be compared qualitatively.

3.1 Classical Electromagnetic Radiation

For simplicity and as an introduction to the problem of radiative energy loss in an amorphous medium we recover the analogue problem in classical electrodynamics, e.g. [Jac98]. Particles which carry electromagnetic charge are subject to radiative energy loss if they are accelerated. The following discussion is restricted to the electron, the generalization to arbitrary charges is straightforward, that is to say the electron charge e had to be replaced by the appropriate charges. We consider fast particles, that is to say particles which move with a velocity $|\vec{v}|$ close to the speed of light c ¹, $|\vec{v}| \rightarrow c$.

In this classical context we discuss two effects which modify the degree of radiative energy loss, namely the Landau-Pomeranchuk-Migdal effect and the Ter-Mikaelian effect, e.g. [Ter72, Bai98c]. The terminology for the further consideration of the strong interaction problem is motivated.

3.1.1 Landau-Pomeranchuk-Migdal Effect

In a situation with successive multiple scatterings of an electron the spectrum of emitted radiation depends on the distance between neighbouring scattering centres. For small distances a suppression of radiation with respect to the sum of each scattering considered separately appears. This is known as Landau-Pomeranchuk-Migdal effect (LPM effect). We present a classical approach to this phenomenon [Pav97, Mül99]. The energy spectrum radiated by moving charges is found from the Liénard-Wiechert potential of the electron in motion. We begin the discussion with equation (14.67) in [Jac98], which describes the differential intensity I as a function of energy ω and solid angle Ω as

$$\frac{d^2 I}{d\omega d\Omega} = \frac{e^2 \omega^2}{4\pi^2 c} \left| \int_{-\infty}^{\infty} \vec{n} \times (\vec{n} \times \vec{\beta}) e^{i\omega(t - \vec{n} \cdot \vec{r}(t)/c)} dt \right|^2, \quad (3.1)$$

where

$$\vec{n} = \frac{\vec{k}}{|\vec{k}|}, \quad \vec{\beta} = \frac{\vec{v}(t)}{c}. \quad (3.2)$$

¹We write explicitly c at this stage, but work in conventional units $c = \hbar = 1$.

Here, $\vec{v}(t) = \frac{d\vec{r}(t)}{dt}$ is the velocity of the charge moving along the trajectory $\vec{r}(t)$ and \vec{k} is the wave vector, which obeys the dispersion relation $\omega = |\vec{k}|$. Relations for cross products of vectors allow to transform this into a more appropriate structure

$$\frac{d^2 I}{d\omega d\Omega} = \frac{e^2 k^2}{4\pi^2} \left| \int_{-\infty}^{\infty} [\vec{n} \times \vec{v}(t)] e^{i\omega t - i\vec{k} \cdot \vec{r}(t)} dt \right|^2. \quad (3.3)$$

In what follows we are interested in the soft photon approximation, $\omega \rightarrow 0$. Furthermore, we consider a dilute medium. Then the scattering process can be simplified by an abrupt change in the direction of the electron's velocity at the scattering point. Outside the scattering centres the particle is assumed to move on a straight line with constant velocity. Given these simplifications, one can exploit Eq. (3.3) to achieve a transparent understanding of the radiation process. In doing so we consider first the single and double scattering processes in some detail in order to generalize afterwards the important aspects to the case of multiple scatterings. Note, that the integration over infinite times in Eq. (3.3) is to be covered by a suitable convergence factor $e^{-\epsilon|t|}$ in the integrand and the subsequent limit $\epsilon \rightarrow 0$ has to be performed finally.

Single Scattering

The situation for a single scattering process is depicted in Fig. 3.1.

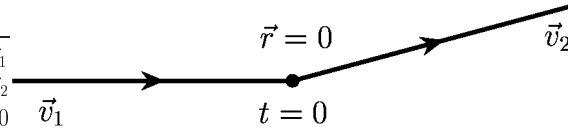


Figure 3.1: Single scattering.

After integration of Eq. (3.3) the phase factors vanish in the limits $t \rightarrow \pm\infty$. The intensity spectrum of emitted radiation

$$\left(\frac{d^2 I}{d\omega d\Omega} \right)_{\text{s.s.}} = \frac{e^2}{4\pi^2 c^2} \left| \frac{\vec{n} \times \vec{v}_1}{\left(1 - \frac{\vec{n} \cdot \vec{v}_1}{c}\right)} - \frac{\vec{n} \times \vec{v}_2}{\left(1 - \frac{\vec{n} \cdot \vec{v}_2}{c}\right)} \right|^2 \quad (3.4)$$

is focused in the direction $\vec{n} \parallel \vec{v}_{1,2}$ because in this case the denominators in Eq. (3.4) become small, so to say they yield large contributions to the radiation. Thus the spectrum is strongly peaked into the forward direction of an ultra-relativistic electron ($|\vec{v}| \rightarrow c$). It becomes also evident from this expression that only with a change in the velocity of the electron emission appears, otherwise the radiation vanishes.

Double Scattering

From the spectrum for double scattering in Fig. 3.2 one derives, that the dominant contributions in the soft photon limit result from the integral parts before the first scattering and after the last interaction, which correspond to the first and the third term in Eq. (3.5), respectively,

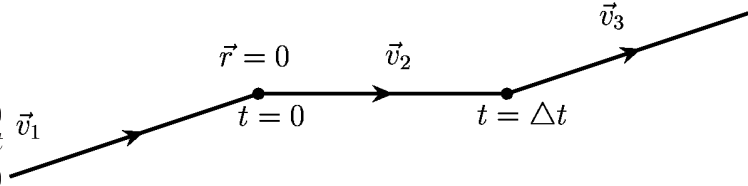


Figure 3.2: Double scattering.

$$\left(\frac{d^2 I}{d\omega d\Omega}\right)_{\text{D.S.}} = \frac{e^2}{4\pi^2 c^2} \left| \frac{\vec{n} \times \vec{v}_1}{\left(1 - \frac{\vec{n}\vec{v}_1}{c}\right)} + \frac{\vec{n} \times \vec{v}_2}{\left(1 - \frac{\vec{n}\vec{v}_2}{c}\right)} \left(e^{i\omega \left(1 - \frac{\vec{n}\vec{v}_2}{c}\right) \Delta t} - 1 \right) - \frac{\vec{n} \times \vec{v}_3}{\left(1 - \frac{\vec{n}\vec{v}_3}{c}\right)} e^{i\omega \left(1 - \frac{\vec{n}\vec{v}_3}{c}\right) \Delta t} \right|^2. \quad (3.5)$$

The intermediate contribution, namely the second term in Eq. (3.5), can be expanded for small ω (soft photon limit). This yields a condition which allows for neglecting the second part in the sum of Eq. (3.5)

$$\frac{1}{\omega \left(1 - \frac{\vec{n}\vec{v}_2}{c}\right)} \equiv t_f \gg \Delta t. \quad (3.6)$$

Here the formation time t_f for the radiation is introduced. Additionally the same condition can be expressed in terms of the travelled distance d between the scatterings. Then the condition for destructive interference reads

$$l_f \equiv \frac{|\vec{v}_2|}{\omega \left(1 - \frac{\vec{n}\vec{v}_2}{c}\right)} \gg d, \quad (3.7)$$

where the formation length l_f is defined. Hence, one expects a suppression of radiation if the spatial separation of the two scattering centres is small enough.

Technically termed, the emission process described by Eq. (3.5) is decomposed into a pre-emission term from the first scattering, a post-emission term from the first scattering, pre-emission from the second scattering and post-emission from the second scattering. Condition (3.7) evidences that a large formation length implies a destructive interference where the post-emission of the first scattering and the pre-emission of the second scattering nearly cancel. Comparison with Eq. (3.4) highlights that under these conditions the double scattering looks effectively like a single scattering. Usually this is called LPM effect.

Physically it is clear that in the soft photon limit the long wavelengths of emitted radiation do not resolve the very details of the scattering centres, and this part of the spectrum must be correspondingly equivalent to a single scattering spectrum.

In the opposite case $l_f \ll d$ however note that the spectrum in Eq. (3.5) can be rearranged and then looks like the sum of two independent scatterings each in the form Eq. (3.4), one from \vec{v}_1 to \vec{v}_2 and the second one from \vec{v}_2 to \vec{v}_3 . This is due to the large fluctuations in the exponential factors, which allow for the neglect of interference terms connecting both scattering processes.

Multiple Scattering

A similar physical picture as for double scattering can be found in the generalized case of soft radiation from multiple scatterings at N centres displayed in Fig. 3.3. One expects a certain number of scattering centres to contribute destructively to the overall spectrum. Fig. 3.3 visualizes that

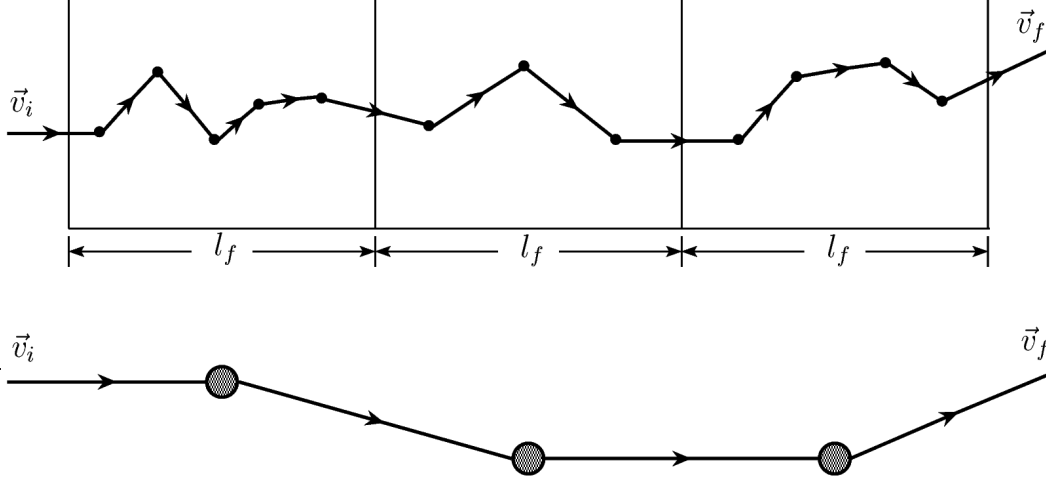


Figure 3.3: Multiple scattering. In the LPM regime scattering centres situated within one formation length l_f act as one single effective scattering centre denoted by the filled circles in the lower graphic.

on average the electron on its path through an amorphous medium experiences particular numbers of scatterings which together act as effective scatterings. The length it traverses in the target of thickness L while one effective scattering is taking place is the formation length l_f . In generalization of Eq. (3.7) the formation length

$$l_f = \frac{|\vec{v}_{\parallel}|}{\omega \left(1 - \frac{\vec{n}\vec{v}_{\parallel}}{c}\right)} \quad (3.8)$$

is determined by the parallel component \vec{v}_{\parallel} of the electron's velocity, that means the projection into the initial direction of the particle. Clearly, this requires that the actual distance of neighbouring scattering centres is small compared to l_f , $d \ll l_f$. As we have discussed in the double scattering case, the radiation spectrum from such an effective scattering centre looks like one generated by a single scattering event, thus the net radiation pattern can be obtained as superposition of $N_{\text{eff}} = \frac{L}{l_f}$ effective single scattering spectra, assuming $l_f < L$.

Hence, for $N_{\text{eff}} < N$ we obtain a suppression effect in the radiation spectrum

$$\left(\frac{d^2I}{d\omega d\Omega}\right)_N = N_{\text{eff}} \cdot \left(\frac{d^2I}{d\omega d\Omega}\right)_{\text{S.S.}}, \quad (3.9)$$

in contrast to the Bethe-Heitler limit², where the radiation from N -times multiple scattering is additive in the number of scatterings, $N_{\text{eff}} \rightarrow N$. The subscript S.S. in Eq. (3.9) indicates that an average single scattering process is meant.

²Note, that Bethe and Heitler have first considered bremsstrahlung for a relativistic electron in Born approximation, e.g. [Lan80].

We will further comment on the main condition of the LPM effect. In Eq. (3.4) we have seen the radiation to be concentrated into the electron direction inside a cone with opening angle $\Theta_{\text{rad}} = \gamma^{-1} = \frac{m}{E}$, which implies that electron and photon will be separated only after a certain time of flight, or formation length l_f . The mass of the electron is m and E its energy. The electron and the photon will propagate independently if the electron is scattered out of its radiation cone, $\overline{\Theta_{\text{scat}}^2} \gg \Theta_{\text{rad}}^2$. Here $\overline{\Theta_{\text{scat}}^2}$ stands for the mean squared scattering angle of the electron. An estimate of this scattering angle in a random walk picture relates $\overline{\Theta_{\text{scat}}^2}$ to l_f to yield $l_f \sim \frac{E}{\sqrt{\omega}}$ [Pav97]. Therefore the spectrum Eq. (3.9), and thus also the energy spectrum $\frac{d\epsilon}{d\omega}$, becomes proportional to $\frac{\sqrt{\omega}}{E}$ in the LPM regime with $\overline{\Theta_{\text{scat}}^2} \gg \Theta_{\text{rad}}^2$, otherwise, for $\overline{\Theta_{\text{scat}}^2} < \Theta_{\text{rad}}^2$, in the Bethe-Heitler limit the spectrum is constant with respect to the initial energy E and the frequency ω of the emitted radiation.

In summary, in the true sense the LPM effect is the destructive interference of radiation from a certain number of scatterings arranged within a formation length l_f , whereby the electron having passed l_f is scattered out of its radiation cone due to multiple scattering. Besides this meaning one often meets other destructive interference effects to be termed LPM effect. A description of both effects, the LPM effect and the Ter-Mikaelian effect, to be considered below, on quantum-mechanical grounds has been developed by Migdal.

3.1.2 Ter-Mikaelian Effect

Besides the radiation suppression effect of multiple scatterings the polarization of the medium influences on bremsstrahlung off ultra-relativistic electrons. It was found by Ter-Mikaelian that this effect can further reduce the radiation spectrum especially in the soft frequency limit. We present an explanation based on classical coherence arguments following the method of Galitsky and Gurevich [Gal64].

Here the formation length l_f given by Eq. (3.8) in Section 3.1.1 can be identified with a coherence length l , which is the path length the emitting particle travels over which the radiation remains coherent. The geometrical condition to maintain coherence defines the coherence length

$$l(\omega, \theta) = \frac{\lambda}{2} \cdot \frac{v \cdot \overline{\cos \theta_s}}{1/\sqrt{\epsilon} - v \cdot \overline{\cos \theta_s} \cdot \cos \theta} \quad (3.10)$$

as the electron's path length where the phase difference equals $\frac{\pi}{2}$, or $\frac{\lambda}{2}$ in terms of the wavelength λ . This coherence length depends on the emission angle of radiation θ , its frequency ω or wave length λ , θ_s denotes the multiple scattering angle of the electron and $\overline{\cos \theta_s}$ the average value, but most importantly here $\frac{1}{\sqrt{\epsilon}}$ stands for the increased phase velocity of the emitted bremsstrahlung. The dielectric constant ϵ takes into account the polarization effects of the medium. Note that this expression corresponds to Eq. (3.8) for the formation length l_f apart from a constant factor π if we focus on the LPM effect in Eq. (3.10) by setting $\epsilon = 1$ for the vacuum, $\lambda = \frac{2\pi}{\omega}$ and $|\vec{v}_{\parallel}| = v \cdot \overline{\cos \theta_s}$.

In order to target the polarization effect we state that the radiation intensity per unit frequency interval $I(\omega)$ can be expressed in terms of the Bethe-Heitler expression $I_{\text{BH}}(\omega)$,

$$I(\omega) = q \cdot I_{\text{BH}}(\omega), \quad (3.11)$$

modified by a reduction factor

$$q = \frac{l(\omega, 0)}{l_0(\omega, 0)} = \frac{l^*}{l_0^*}, \quad (3.12)$$

which is the ratio of the forward emission coherence lengths $l^* \equiv l(\omega, 0)$ in medium and $l_0^* \equiv l_0(\omega, 0)$ in the absence of medium effects, that means for $\epsilon = 1$ and $\cos \theta_s = 1$. Using Eq. (3.10) and the familiar relations

$$\epsilon = 1 - \frac{\omega_0^2}{\omega^2} \quad (\omega \gg \omega_0), \quad (3.13)$$

$$\overline{\theta_s^2} = \frac{E_s^2 l_0^*}{E^2 X}, \quad (3.14)$$

together with expansions of $\frac{1}{\sqrt{\epsilon}}$ and $\cos \theta_s$ under the assumptions $\epsilon \approx 1$ and $\cos \theta \approx 1$ one then obtains

$$q(E, \omega) = \left(1 + \frac{E^2 \omega_0^2}{m^2 \omega^2} + \frac{E^2 E_s^2}{m^4} \frac{q}{X\omega} \right)^{-1}. \quad (3.15)$$

Here the parameter ω_0 is the plasma frequency and formally corresponds to a mass term for the photon, E is again the energy of the electron and m its mass. Furthermore, X is a characteristic radiation length and E_s a typical energy scale, both arising from the Bethe-Heitler spectrum.

The reduction effect is purely due to medium polarization if

$$1 + \frac{E^2 \omega_0^2}{m^2 \omega^2} > \frac{E^2 E_s^2}{m^4} \frac{q}{X\omega}. \quad (3.16)$$

Then the reduction factor becomes

$$q = \frac{\omega^2}{\omega^2 + (E^2/m^2)\omega_0^2} < 1. \quad (3.17)$$

In reversing the inequality (3.16) one can find a regime for LPM suppression. For more details on this situation, the calculation itself and a subtle discussion of the competing contributions from LPM effect, TM effect and the absorption of quanta the reader might be referred to [Gal64].

In conclusion we repeat that the polarization of the medium causes the bremsstrahlung spectrum off an relativistic electron passing an amorphous medium to be reduced for lower frequencies. This is the proper Ter-Mikaelian effect.

The importance of the TM effect for the energy loss of quarks in deconfined matter was already questioned in [Mül99] and [Käm00]. It was confirmed that a direct analogue of this effect in QED also exists in QCD.

3.2 Quantum Description: Cross Section and Radiation Amplitude

Guided by the above classical considerations we turn to a quantum description of the radiation process within perturbation theory. The analogue to classical electrodynamics is QED. This section introduces quantities which are suitable to discuss the radiation pattern in inelastic collisions in the soft radiation limit in detail.

3.2.1 General Cross Section

The differential cross section for a process with two initial and n final particles with initial (final) energies E_k (E'_k) and initial (final) momenta p_k (p'_k) generally takes the following form as can be found in many textbooks, e.g. [Bjo90],

$$d\sigma = \frac{1}{|\vec{v}_1 - \vec{v}_2|} \left(\frac{N_1}{2E_1} \right) \left(\frac{N_2}{2E_2} \right) |M|^2 \frac{N'_1 d^3 p'_1}{2E'_1 (2\pi)^3} \cdots \frac{N'_n d^3 p'_n}{2E'_n (2\pi)^3} \cdot (2\pi)^4 \delta^{(4)} \left(p_1 + p_2 - \sum_{i=1}^n p'_i \right) S. \quad (3.18)$$

The factors N_i are 1 for spinless particles, photons and gluons. Otherwise, in the case of Dirac particles, $N_i = 2m_i$ if the spinors are normalized to 1. The dynamics is now contained in the matrix element M , the delta function takes care of energy-momentum conservation. The statistical factor $S = \prod_i \frac{1}{l_i!}$ accounts for l_i identical particles of sort i in the final state.

3.2.2 Radiation Amplitude

In order to motivate the quantity "radiation amplitude" we consider first the situation where the emission of one photon is induced by the scattering of two electrons. From a comparison of the elastic and inelastic differential cross sections one can define a ratio which represents the probability of a photon being emitted. The respective cross sections which belong to the diagrams depicted for the quark-gluon case in Fig. D.1 and Figs. D.4(a)-D.4(d), to be modified by replacing gluon and quark lines with photon and electron lines, are

$$d\sigma_{\text{inel}} = \frac{S \cdot (2\pi)^4 \delta^{(4)}(p_1 + p_2 - p'_1 - p'_2 - k)}{|\vec{v}_1 - \vec{v}_2|} \left(\frac{N_1}{2E_1} \right) \left(\frac{N_2}{2E_2} \right) \cdot |M_{\text{inel}}|^2 \frac{N'_1 d^3 p'_1}{2E'_1 (2\pi)^3} \frac{N'_2 d^3 p'_2}{2E'_2 (2\pi)^3} \frac{d^3 k}{2\omega (2\pi)^3}, \quad (3.19)$$

$$d\sigma_{\text{el}} = \frac{S \cdot (2\pi)^4 \delta^{(4)}(p_1 + p_2 - p'_1 - p'_2)}{|\vec{v}_1 - \vec{v}_2|} \left(\frac{N_1}{2E_1} \right) \left(\frac{N_2}{2E_2} \right) |M_{\text{el}}|^2 \frac{N'_1 d^3 p'_1}{2E'_1 (2\pi)^3} \frac{N'_2 d^3 p'_2}{2E'_2 (2\pi)^3}. \quad (3.20)$$

Before the ratio is taken, the squared matrix elements are summed over all final polarizations and an average over initial polarization configurations is carried out. The overline at the matrix element indicates this summing and averaging procedure. We define the radiation amplitude by means of

$$dP = \frac{\overline{d\sigma_{\text{inel}}}}{\overline{d\sigma_{\text{el}}}} = \frac{\overline{|M_{\text{inel}}|^2}}{\overline{|M_{\text{el}}|^2}} \cdot \frac{d^3 k}{2\omega (2\pi)^3}. \quad (3.21)$$

The idea behind this quantity is a factorisation into a part describing the emitted radiation and an underlying part for the elastic scattering. This factorisation holds only true if the momentum of the photon is negligible compared to the momenta of the other particles, an assumption, which is called soft radiation limit. Eq. (3.21) describes the probability of one photon emission under the condition that an elastic scattering has occurred, that is to say P is a conditional probability. Usually, one defines the photon number distribution R_γ

$$R_\gamma = \omega \frac{d^3 N_\gamma}{d^3 k} = \frac{1}{2(2\pi)^3} \frac{\overline{|M_{\text{inel}}|^2}}{\overline{|M_{\text{el}}|^2}} \quad (3.22)$$

(see for instance Eqs. (15), (16) and (45) in [Gyu00a]).

Besides the kinematical or constant factors the relevant physics in Eq. (3.21) is, very close to the definition of R_γ , described by the fraction

$$\overline{|R|^2} = \frac{\overline{|M_{\text{inel}}|^2}}{\overline{|M_{\text{el}}|^2}}, \quad (3.23)$$

which is the sufficient quantity to compare different radiation patterns in such processes in the next chapters. We will call this the radiation amplitude R , or strictly speaking the summed and averaged squared radiation amplitude $\overline{|R|^2}$, but for convenience the term ‘‘radiation amplitude’’ will always be used in the following if the meaning is obvious.

The above considerations apply directly to one gluon emission. The matrix elements have to be summed additionally over final colour states and averaged over initial colour states. The relevant QCD diagrams are shown in Fig. D.1 and Figs. D.4, where a new kind of diagram due to the three-gluon vertex, or sometimes also called triple-vertex, occurs, Fig. D.4(e). Corresponding colour factors have to be implemented. A detailed discussion with respect to the colour states is presented in Appendix A.

The radiation amplitudes for single scattering processes and similarly defined for double scattering processes with one photon, or gluon respectively, being emitted, are described explicitly in the following chapters.

For completeness, we mention that another different quantity, also called radiation amplitude, is introduced (cf. Eq. (16) in [Wan95]),

$$i\tilde{R} = T_{AB}^c T_{CD}^c \frac{M_{\text{rad}}}{M_{\text{el}}}, \quad (3.24)$$

with $M_{\text{rad}} \equiv M_{\text{inel}}$. Substituting this into Eq. (3.23), with $M_{\text{el}} = T_{AB}^c T_{CD}^c \cdot M_{\text{el,no colour}}$ one obtains

$$\overline{|R|^2} = \frac{\overline{|\tilde{R}M_{\text{el,no colour}}|^2}}{\overline{|M_{\text{el}}|^2}}, \quad (3.25)$$

and since $M_{\text{el,no colour}}$ is colour independent one can divide the overline in the denominator

$$\overline{|R|^2} = \frac{\overline{|\tilde{R}M_{\text{el,no colour}}|^2}}{\overline{|T_{AB}^c T_{CD}^c|^2} \cdot \overline{|M_{\text{el,no colour}}|^2}}. \quad (3.26)$$

The colour structure gives $C_{1,\text{el}}$, for more details refer to Eq. (A.13), and the overline in the numerator can also be split if \tilde{R} is independent of those states $M_{\text{el,no colour}}$ still depends on. This could only be spins, thus for scalar QCD the summing and averaging procedure can be divided and $\overline{|M_{\text{el,no colour}}|^2}$ cancels

$$\overline{|R|^2} = \frac{\overline{|\tilde{R}|^2}}{C_{1,\text{el}}}. \quad (3.27)$$

Hence, the radiation amplitudes R and \tilde{R} differ by a constant colour factor.

3.3 The Potential Model

In order to describe the radiation effects if a high energetic particle is passing an overall colour-neutral deconfined phase, a potential model was employed firstly by Gyulassy and Wang [Gyu94, Wan95]. They have justified that in a particular gauge, the A^+ -gauge, see Appendix C, the radiation contributions from target lines can be neglected. In Appendix C this is also demonstrated numerically.

Therefore, the target particles can be modelled by localized static screened potentials in the form (cf. Eq. (1) in [Wan95])

$$V_{AB}^a(\vec{q}) = gT_{AB}^a \frac{e^{-i\vec{q}\vec{x}_i}}{\vec{q}^2 + \mu^2}, \quad (3.28)$$

which arises as Fourier transformation $f(\vec{q}) = \int d^3x \tilde{f}(\vec{x})$ of the screened Coulomb potential

$$\tilde{V}_{AB}^a(\vec{x}) = \frac{gT_{AB}^a}{4\pi|\vec{x} - \vec{x}_i|} e^{-\mu|\vec{x} - \vec{x}_i|}. \quad (3.29)$$

Thereby \vec{x}_i denote the space points where these Yukawa type potentials are localized. Successive scatterings are assumed to be well separated, $\lambda \gg \mu^{-1}$, where λ is the average mean free path length of an incident projectile parton, $1/\mu$ is the Debye screening length and μ is called the Debye screening mass. The value of g is not varying here. The term T_{AB}^a stands for the original colour structure of the target and is explained in Appendix A.

3.4 Divergences

Different types of infrared divergences caused by vanishing mass parameters may arise. Firstly, due to the massless gauge boson, which is the photon in QED and the gluon in QCD, respectively, a so-called soft divergence is expected. Secondly, the collinear divergence is expected to follow from a massless matter field. The introduction of a gluon mass μ breaks gauge invariance, but in this manner the soft divergences from gluon propagators can be suppressed. Keeping the mass parameters for the quarks, collinear divergences are ruled out, too. The method for the gauge boson propagator is known as mass regularization, another possible scheme is to eliminate problematic regions in the phase space by a cut-off method.

4 Single Scattering with One-Gluon Emission

The aim of this chapter is to clarify the one-gluon emission in a single scattering event. Analogue to [Wan95] we employ the potential model to simulate the scattering of on-shell quarks. Despite of the simplicity of the formal expressions we will meet an astonishing complexity of the radiation pattern. Furthermore, we will compare the potential model with a quark-quark scattering calculation.

4.1 Kinematical Situation and Declarations

We first introduce the necessary diagrams and matrix elements within the potential model approach. Additionally, we construct the relevant kinematical conditions and emphasize the important approximations. Here, we explain the QCD situation, whose expressions can easily be reduced to the QED case.

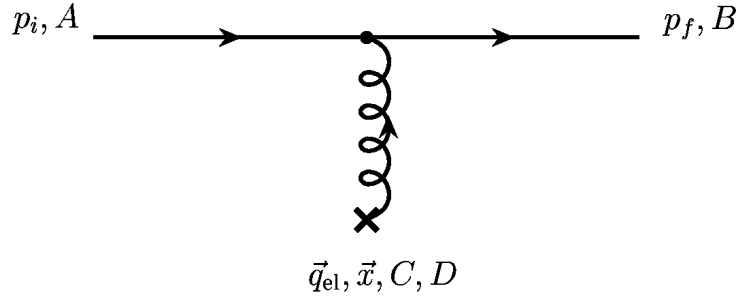


Figure 4.1: Feynman diagram for single elastic scattering in the potential model described by the amplitude $M_{1,\text{el}}^{\text{QCD}}$.

From the Feynman rules, see Appendix B, one directly obtains the matrix elements for the relevant Feynman diagrams. The matrix element for the single elastic scattering process Fig. 4.1, which we need as normalization in the radiation amplitude Eq. (3.23), reads

$$M_{1,\text{el}}^{\text{QCD}} = T_{AB}^c T_{CD}^c \cdot (-ig)(p_f + p_i)_\mu \cdot (-ig)g^{0\mu} \frac{e^{-i\vec{q}_{\text{el}}\vec{x}}}{\vec{q}_{\text{el}}^2 + \mu^2}. \quad (4.1)$$

The fact, that the potential can only impart spatial momentum transfer to the projectile, but no energy transfer, essentially simplifies the kinematics and the elastic matrix element becomes

$$M_{1,\text{el}}^{\text{QCD}} = T_{AB}^c T_{CD}^c \cdot (-g^2) \cdot 2E \cdot \frac{e^{-i\vec{q}_{\text{el}}\vec{x}}}{\vec{q}_{\text{el}}^2 + \mu^2}. \quad (4.2)$$

There are three possible diagrams of lowest order, where the emission of a gluon takes place. Note, that initial state radiation of an incoming particle with high virtuality, which is for instance studied in [Gyu00a], does not take place, because we consider here on-shell particles. We denote the diagrams Fig. 4.2 and Fig. 4.3, which appear also in QED without colour factors, of course, as abelian diagrams and distinguish between the case when the emission occurs before the potential scattering (pre-emission) and the opposite case (post-emission). The technique of indexing the individual diagrams with $M_{n,m,l}$ was introduced in [Gyu00a] and is explained in more detail in Section 5.2.

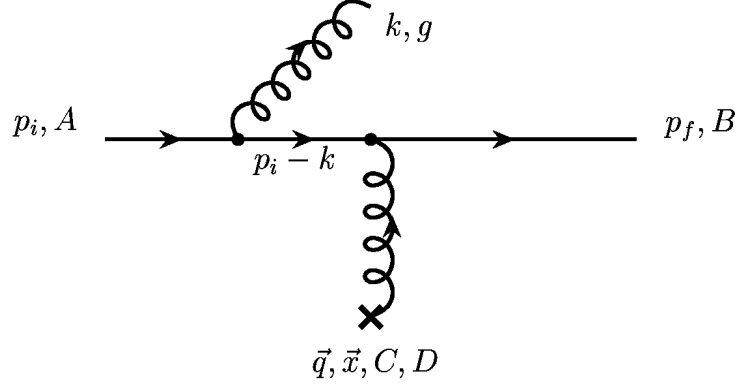


Figure 4.2: Feynman diagram for $M_{1,0,0}^{\text{QCD}}$, i.e. the single scattering with one gluon emission in the potential model. This diagram will be referred to as pre-emission diagram.

The matrix element for the pre-emission situation (see Fig. 4.2) is derived similarly as before

$$M_{1,0,0}^{\text{QCD}} = (T^f T^g)_{AB} T_{CD}^f \cdot (-ig)(p_f + p_i - k)_\mu \cdot \frac{i}{(p_i - k)^2 - m^2 + i\epsilon} \cdot (-ig)(2p_i - k)_\sigma \epsilon^\sigma \cdot (-ig)g^{0\mu} \frac{e^{-i\vec{q}\vec{x}}}{\vec{q}^2 + \mu^2}, \quad (4.3)$$

and can be reduced to

$$M_{1,0,0}^{\text{QCD}} = (T^f T^g)_{AB} T_{CD}^f \cdot g^3 \cdot 2(E - \omega) \cdot \frac{e^{-i\vec{q}\vec{x}}}{\vec{q}^2 + \mu^2} \cdot \frac{p_i \epsilon}{p_i k}. \quad (4.4)$$

In the same manner, the corresponding equation for the post-emission process (Fig. 4.3) is

$$M_{1,1,0}^{\text{QCD}} = (T^g T^f)_{AB} T_{CD}^f \cdot (-ig)(2p_f + k)_\sigma \epsilon^\sigma \cdot \frac{i}{(p_f + k)^2 - m^2 + i\epsilon} \cdot (-ig)(p_f + k + p_i)_\mu \cdot (-ig)g^{0\mu} \frac{e^{-i\vec{q}\vec{x}}}{\vec{q}^2 + \mu^2}, \quad (4.5)$$

and subsequently yields

$$M_{1,1,0}^{\text{QCD}} = (T^g T^f)_{AB} T_{CD}^f \cdot (-g^3) \cdot 2E \cdot \frac{e^{-i\vec{q}\vec{x}}}{\vec{q}^2 + \mu^2} \cdot \frac{p_f \epsilon}{p_f k}. \quad (4.6)$$

For a complete terminology, the non-abelian diagram Fig. 4.4 will be often called the three-gluon contribution. The structure is slightly more involved due to the appearance of the three-gluon vertex,

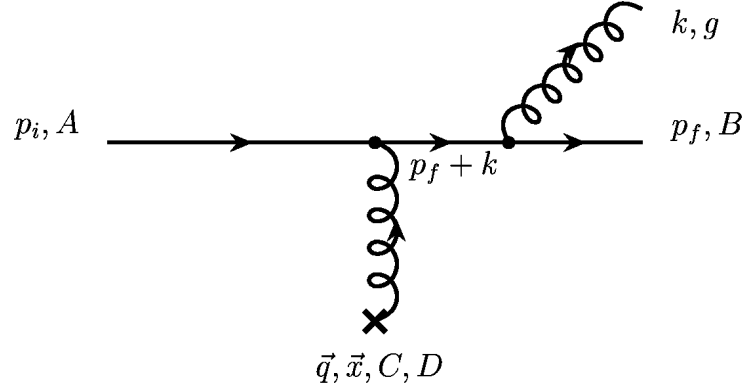


Figure 4.3: Feynman diagram for $M_{1,1,0}^{\text{QCD}}$, i.e. the single scattering with one gluon emission in the potential model. This diagram will be referred to as post-emission diagram.

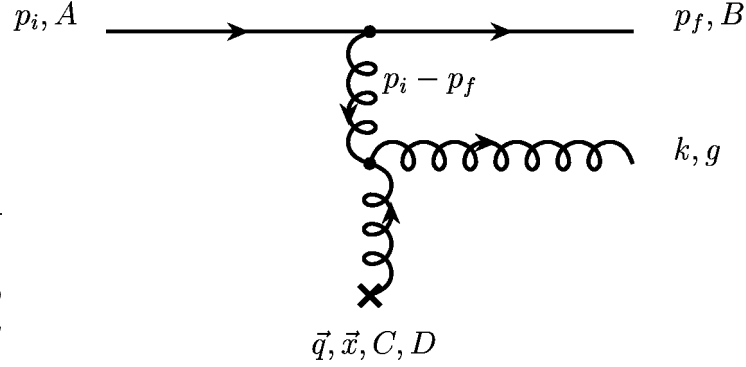


Figure 4.4: Feynman diagram for $M_{1,0,1}^{\text{QCD}}$, i.e. the single scattering with one gluon emission in the potential model. This diagram will be referred to as three-gluon diagram.

$$M_{1,0,1}^{\text{QCD}} = (-ig)(p_f + p_i)_\mu T_{AB}^e \cdot \frac{-ig^{\tau\mu}}{(p_i - p_f)^2} \cdot \epsilon^\sigma \cdot (-ig)g^{0\rho} \frac{e^{-i\vec{q}\vec{x}}}{\vec{q}^2 + \mu^2} T_{CD}^f \cdot (ig)(if_{egf})[(p_i - p_f + k)_\rho g_{\tau\sigma} + (-k - q)_\tau g_{\sigma\rho} + (q - p_i + p_f)_\sigma g_{\rho\tau}], \quad (4.7)$$

which can be written in the form

$$M_{1,0,1}^{\text{QCD}} = [T^f, T^g]_{AB} T_{CD}^f \cdot g^3 \cdot \frac{e^{-i\vec{q}\vec{x}}}{\vec{q}^2 + \mu^2} \cdot \frac{1}{(p_i - p_f)^2} \cdot [2\omega \cdot (p_i + p_f)\epsilon - \epsilon_0 \cdot (p_i + p_f)(k + q) + (2E - \omega) \cdot 2q\epsilon]. \quad (4.8)$$

So far, we have only applied the on-shell condition for the emitted gluon, $k^2 = 0$, the Lorentz condition, $\epsilon k = 0$, and the general conservation of the total four-momentum,

$$p_i + q = p_f + k, \quad (4.9)$$

especially the simplified energy conservation with $q_0 = 0$. Now, we want to evaluate the matrix element expressions further with the aim to obtain an analytical dependence, which can be used later to understand the exact numerical results. Therefore, we restrict the kinematical situation and assume an on-shell projectile quark incident in z-direction,

$$p_i = (E, 0, 0, p_{iz}). \quad (4.10)$$

For brevity, we have declared $E_i \equiv E$. The energy is determined by the positive root of the on-shell condition $p_i^2 = m^2$, where m is the quark mass and remains constant. In A^+ -gauge it is suitable to work in light-cone coordinates,

$$\begin{aligned} p_i &= [p^+, p^-, \vec{p}_\perp] \equiv [p_{i_0} + p_{i_z}, p_0 - p_z, \vec{p}_\perp] \\ &= \left[E + \sqrt{E^2 - m^2}, E - \sqrt{E^2 - m^2}, \vec{0}_\perp \right]. \end{aligned} \quad (4.11)$$

We consider situations where m is small compared to E . An expansion in the mass of the projectile yields

$$p_i \approx \left[2E - \frac{m^2}{2E}, \frac{m^2}{2E}, \vec{0}_\perp \right], \quad (4.12)$$

where we only kept the terms up to the order $1/E$. Note, that in this formulation the on-shell condition is only satisfied in the zeroth order $(1/E)^0$.

Also, the momentum of the gluon and the polarisation vectors are fixed by choosing the A^+ -gauge, refer to Appendix C,

$$k = \left[2Ex, \frac{\vec{k}_\perp^2}{2Ex}, \vec{k}_\perp \right], \quad (4.13)$$

$$\epsilon = \left[0, \frac{\vec{\epsilon}_\perp \vec{k}_\perp}{Ex}, \vec{\epsilon}_\perp \right]. \quad (4.14)$$

The plus-component of k is parameterised by x relative to the plus-component $2E$ of the incident particle. The value of

$$x = \frac{\omega}{2E}(1 + \cos \theta) = \frac{\omega}{E} \cos^2(\theta/2) \leq \frac{\omega}{E} \quad (4.15)$$

is restricted to $0 \leq x \leq 1$, because the maximum energy available for the gluon is $2E$. In our discussion x will always be sufficiently smaller than one, since we assume the soft gluon limit, where

$$E \gg \omega. \quad (4.16)$$

Furthermore, we assume $E \gg |\vec{q}_\perp|$ and $E \gg m$. This is why we will carry out expansions in $1/E$ and neglect higher orders of $1/E$ when we simplify kinematical expressions.

We begin with the pre-emission Eq. (4.4) and find¹

$$p_i \epsilon = \frac{1}{2} \cdot \left(2E - \frac{m^2}{2E} \right) \cdot \frac{\vec{\epsilon}_\perp \vec{k}_\perp}{Ex} \approx \frac{\vec{\epsilon}_\perp \vec{k}_\perp}{x}, \quad (4.17a)$$

$$p_i k = \frac{1}{2} \cdot \left(2E - \frac{m^2}{2E} \right) \cdot \frac{\vec{k}_\perp^2}{2Ex} + \frac{1}{2} \cdot \frac{m^2}{2E} \cdot 2Ex \approx \frac{1}{2x} (\vec{k}_\perp^2 + x^2 m^2), \quad (4.17b)$$

¹According to the definition of light-cone coordinates as in Eq. (4.11) also the metric $g^{\mu\nu}$ is modified, such that $a_\mu b^\mu = \frac{1}{2}(a^+ b^- + a^- b^+ + \vec{a}_\perp \vec{b}_\perp)$.

which yields

$$\frac{p_i \epsilon}{p_i k} = \frac{\vec{\epsilon}_\perp \vec{k}_\perp}{\vec{k}_\perp^2 + x^2 m^2}. \quad (4.17c)$$

The conservation of energy,

$$E_i = E_f + \omega, \quad (4.18)$$

can be expressed in terms of E by

$$E_f = E - \omega = E - \frac{1}{2}(k^+ + k^-) = E - \frac{1}{2} \left(2Ex + \frac{\vec{k}_\perp^2}{2Ex} \right) \approx E(1 - x) + O\left(\frac{1}{E}\right). \quad (4.19)$$

Since, in the limit of small gluon emission angles, $x \xrightarrow{\theta \rightarrow 0} \frac{\omega}{E}$, see Eq. (4.15), we might write the energy pre-factor $(E - \omega)$ in Eq. (4.4) as $E(1 - x)$ and obtain

$$M_{1,0,0}^{\text{QCD}} = \frac{M_{1,\text{el}}^{\text{QCD}}}{T_{A'B'}^c T_{C'D'}^c} \cdot (-2g)(1 - x) \cdot (T^f T^g)_{AB} T_{CD}^f \cdot \frac{\vec{\epsilon}_\perp \vec{k}_\perp}{\vec{k}_\perp^2 + x^2 m^2}, \quad (4.20)$$

where the elastic part Eq. (4.2) is factorised out under the important assumption

$$\vec{q}_{\text{rad}} \equiv \vec{q} \approx \vec{q}_{\text{el}}. \quad (4.21)$$

Since $x \ll 1$ in the soft gluon limit, Eq. (4.16), we will usually omit the factor $(1 - x)$ in the matrix element expressions and work with the form as in Eq. (4.33a).

In the post-emission and three-gluon vertex terms Eqs. (4.6) and (4.8) also the final quark momentum enters. Therefore, we have to solve the kinematical equations at first. The momentum transfer q in light-cone variables reads

$$q = (0, \vec{q}_\perp, q_z) = [q_z, -q_z, \vec{q}_\perp]. \quad (4.22)$$

With

$$qp_i = \frac{1}{2} \cdot q_z \cdot \frac{m^2}{2E} - \frac{1}{2} \cdot q_z \cdot \left(2E - \frac{m^2}{2E} \right) = q_z \left(\frac{m^2}{2E} - E \right), \quad (4.23)$$

$$qk = \frac{1}{2} \cdot q_z \cdot \frac{\vec{k}_\perp^2}{2Ex} - \frac{1}{2} \cdot q_z \cdot 2Ex - \vec{q}_\perp \vec{k}_\perp = q_z \left(\frac{\vec{k}_\perp^2}{4Ex} - Ex \right) - \vec{q}_\perp \vec{k}_\perp, \quad (4.24)$$

squaring of the momentum conservation Eq. (4.9) finally yields q_z in terms of the given quantities \vec{q}_\perp , k and p_i . Furthermore,

$$\begin{aligned} p_f^2 &= (p_i + q - k)^2, \\ p_f^2 &= p_i^2 + q^2 + k^2 + 2q(p_i - k) - 2p_i k, \\ m^2 &= m^2 - q_z^2 - \vec{q}_\perp^2 + 2q_z \left(\frac{m^2}{2E} - E \right) - 2q_z \left(\frac{\vec{k}_\perp^2}{4Ex} - Ex \right) + 2\vec{q}_\perp \vec{k}_\perp - \frac{1}{x}(\vec{k}_\perp^2 + x^2 m^2), \end{aligned}$$

$$\begin{aligned}
0 &= q_z^2 + 2q_z \left(E(1-x) + \frac{\vec{k}_\perp^2}{4Ex} - \frac{m^2}{2E} \right) + (\vec{k}_\perp - \vec{q}_\perp)^2 + \frac{\vec{k}_\perp^2}{x}(1-x) + xm^2, \\
q_z &= - \left(E(1-x) + \frac{\vec{k}_\perp^2}{4Ex} - \frac{m^2}{2E} \right) \pm E(1-x) \\
&\quad \cdot \sqrt{1 - \frac{\vec{k}_\perp^2}{2xE^2(1-x)} - \frac{m^2}{E^2(1-x)^2} - \frac{(\vec{k}_\perp - \vec{q}_\perp)^2}{E^2(1-x)^2} + \frac{1}{16E^4(1-x)^2} \left(\frac{\vec{k}_\perp^2}{x} - m^2 \right)^2}, \\
q_z &\approx - \left(E(1-x) + \frac{\vec{k}_\perp^2}{4Ex} - \frac{m^2}{2E} \right) \pm E(1-x) \\
&\quad \cdot \left(1 - \frac{\vec{k}_\perp^2}{4xE^2(1-x)} - \frac{m^2}{2E^2(1-x)^2} - \frac{(\vec{k}_\perp - \vec{q}_\perp)^2}{2E^2(1-x)^2} \right).
\end{aligned}$$

We focus on the positive root solution

$$q_z^{(+)} = -\frac{\vec{k}_\perp^2}{2Ex} - \frac{(\vec{k}_\perp - \vec{q}_\perp)^2}{2E(1-x)} - \frac{xm^2}{2E(1-x)}, \quad (4.25)$$

because we are interested in scatterings with small momentum transfers, that is to say forward scattering of the incident particle. The second solution, $q_z^{(-)} \approx -2E(1-x)$, corresponds to momentum transfers in the range of E , which is the excluded backward scattering scenario.²

Hence, from Eq. (4.9), we find the final quark momentum

$$\begin{aligned}
p_f &= p_i + q - k \\
&= \left[2E(1-x) + O\left(\frac{1}{E}\right), \frac{m^2}{2E(1-x)} + \frac{(\vec{k}_\perp - \vec{q}_\perp)^2}{2E(1-x)}, \vec{q}_\perp - \vec{k}_\perp \right], \quad (4.26)
\end{aligned}$$

where, as for p_i in Eq. (4.11), the on-shell condition holds true in the lowest order of $(1/E)$.

We are now in the position to analyse further the remaining matrix elements $M_{1,1,0}^{\text{QCD}}$ and $M_{1,0,1}^{\text{QCD}}$. In Eq. (4.6) we write out the four products and obtain

$$\frac{p_f \epsilon}{p_f k} = \frac{\frac{1}{2} \cdot 2E(1-x) \cdot \frac{\vec{\epsilon}_\perp \vec{k}_\perp}{Ex} - (\vec{q}_\perp - \vec{k}_\perp) \vec{\epsilon}_\perp}{\frac{1}{2} \cdot 2E(1-x) \cdot \frac{\vec{k}_\perp^2}{2Ex} + \frac{1}{2} \cdot \left(\frac{m^2}{2E(1-x)} + \frac{(\vec{k}_\perp - \vec{q}_\perp)^2}{2E(1-x)} \right) \cdot 2Ex - (\vec{q}_\perp - \vec{k}_\perp) \vec{k}_\perp}, \quad (4.27)$$

where we kept our strategy to neglect terms of higher order in $1/E$,

$$\frac{p_f \epsilon}{p_f k} = \frac{(1-x) \cdot \frac{\vec{\epsilon}_\perp \vec{k}_\perp}{x} - (\vec{q}_\perp - \vec{k}_\perp) \vec{\epsilon}_\perp}{(1-x) \cdot \frac{\vec{k}_\perp^2}{2x} + \left(\frac{m^2}{2(1-x)} + \frac{(\vec{k}_\perp - \vec{q}_\perp)^2}{2(1-x)} \right) \cdot x - (\vec{q}_\perp - \vec{k}_\perp) \vec{k}_\perp}$$

²We have numerically verified that the results for backward scattering are usually suppressed by orders of magnitude compared to the corresponding forward scattering scenario.

$$\begin{aligned}
&= \frac{\frac{1}{x}\vec{\epsilon}_\perp[(1-x)\cdot\vec{k}_\perp - x(\vec{q}_\perp - \vec{k}_\perp)]}{\frac{1}{2x(1-x)}\left[(1-x)^2\vec{k}_\perp^2 + x^2m^2 + x^2(\vec{k}_\perp - \vec{q}_\perp)^2 - 2x(1-x)(\vec{q}_\perp - \vec{k}_\perp)\vec{k}_\perp\right]} \\
&= \frac{\frac{1}{x}\vec{\epsilon}_\perp(\vec{k}_\perp - x\vec{q}_\perp)}{\frac{1}{2x(1-x)}\left[\left((1-x)\vec{k}_\perp - x(\vec{q}_\perp - \vec{k}_\perp)\right)^2 + x^2m^2\right]} \\
&= \frac{2(1-x)\vec{\epsilon}_\perp(\vec{k}_\perp - x\vec{q}_\perp)}{(\vec{k}_\perp - x\vec{q}_\perp)^2 + x^2m^2}. \tag{4.28}
\end{aligned}$$

Thus, the post-emission matrix element Eq. (4.6) becomes

$$M_{1,1,0}^{\text{QCD}} = \frac{M_{1,\text{el}}^{\text{QCD}}}{T_{A'B'}^c T_{C'D'}^c} \cdot (-2g)(1-x) \cdot (T^g T^f)_{AB} T_{CD}^f \cdot \frac{-\vec{\epsilon}_\perp(\vec{k}_\perp - x\vec{q}_\perp)}{(\vec{k}_\perp - x\vec{q}_\perp)^2 + x^2m^2}, \tag{4.29}$$

yielding finally Eq. (4.33b) below in the soft gluon approximation, respectively.

For the non-abelian three-gluon vertex matrix element Eq. (4.8) we evaluate the denominator

$$\begin{aligned}
(p_i - p_f)^2 &= 2m^2 - 2p_i p_f \\
&= 2m^2 - \left[2E \cdot \left(\frac{m^2}{2E(1-x)} + \frac{(\vec{k}_\perp - \vec{q}_\perp)^2}{2E(1-x)}\right) + \frac{m^2}{2E} \cdot 2E(1-x)\right] + O\left(\frac{1}{E^2}\right) \\
&\approx -\frac{1}{1-x} \left[(\vec{k}_\perp - \vec{q}_\perp)^2 + x^2m^2\right], \tag{4.30a}
\end{aligned}$$

and the contributions

$$\begin{aligned}
I_a &\equiv 2\omega \cdot (p_i + p_f)\epsilon \\
&= 2\omega \left[\frac{\vec{\epsilon}_\perp \vec{k}_\perp}{x} + \frac{1}{2} \cdot 2E(1-x) \cdot \frac{\vec{\epsilon}_\perp \vec{k}_\perp}{Ex} - (\vec{q}_\perp - \vec{k}_\perp)\vec{\epsilon}_\perp + O\left(\frac{1}{E^2}\right) \right] \\
&\approx \frac{2\omega}{x} \vec{\epsilon}_\perp (2\vec{k}_\perp - x\vec{q}_\perp) \\
&= 2E \cdot \vec{\epsilon}_\perp (2\vec{k}_\perp - x\vec{q}_\perp), \tag{4.30b}
\end{aligned}$$

using Eq. (4.17a) and $\omega \approx xE$ for small gluon emission angles,

$$\begin{aligned}
I_b &\equiv \epsilon_0 \cdot (p_i + p_f)(k + q) \\
&= \frac{\vec{\epsilon}_\perp \vec{k}_\perp}{2Ex} \cdot (2p_i + q - k)(q + k) \\
&= \frac{\vec{\epsilon}_\perp \vec{k}_\perp}{2Ex} \cdot [2p_i q + 2p_i k + q^2 - k^2] \\
&\approx \frac{\vec{\epsilon}_\perp \vec{k}_\perp}{2Ex} \cdot \left[-2Eq_z + \frac{1}{x}(\vec{k}_\perp^2 + x^2m^2) - \vec{q}_\perp^2\right] \sim \frac{1}{E}, \tag{4.30c}
\end{aligned}$$

where we made use of Eqs. (4.17b), (4.23), $q^2 \approx -\vec{q}_\perp^2$, and $\epsilon_0 = (\epsilon^+ + \epsilon^-)/2 = \frac{\vec{\epsilon}_\perp \vec{k}_\perp}{2Ex}$ was determined by Eq. (4.14),

$$I_c \equiv (2E - \omega) \cdot 2q\epsilon$$

$$\begin{aligned}
&= E(2-x) \cdot \left[q_z \cdot \frac{\vec{\epsilon}_\perp \vec{k}_\perp}{Ex} - 2\vec{\epsilon}_\perp \vec{q}_\perp \right] \\
&\approx -2E(2-x)\vec{\epsilon}_\perp \vec{q}_\perp.
\end{aligned} \tag{4.30d}$$

The total result is then given by the sum of Eqs. (4.30b) and (4.30d),

$$I_a + I_b + I_c = 2E \cdot \vec{\epsilon}_\perp (2\vec{k}_\perp - x\vec{q}_\perp - (2-x)\vec{q}_\perp) = 2E \cdot 2\vec{\epsilon}_\perp (\vec{k}_\perp - \vec{q}_\perp), \tag{4.31}$$

since the second term Eq. (4.30c) is suppressed by a factor $1/E$. Substituting this into Eq. (4.8) finally yields the three-gluon result

$$M_{1,0,1}^{\text{QCD}} = \frac{M_{1,\text{el}}^{\text{QCD}}}{T_{A'B'}^c T_{C'D'}^c} \cdot (-2g)(1-x) \cdot [T^f, T^g]_{AB} T_{CD}^f \cdot \frac{-\vec{\epsilon}_\perp (\vec{k}_\perp - \vec{q}_\perp)}{(\vec{k}_\perp - \vec{q}_\perp)^2 + x^2 m^2}, \tag{4.32}$$

which subsequently gives Eq. (4.33c) below for soft gluons.

In summary, we have obtained the approximate matrix elements in the soft gluon limit corresponding to Figs. 4.2, 4.3 and 4.4 as follows,

$$M_{1,0,0}^{\text{QCD}} = \frac{M_{1,\text{el}}^{\text{QCD}}}{T_{A'B'}^c T_{C'D'}^c} \cdot (-2g) \cdot (T^f T^g)_{AB} T_{CD}^f \cdot \frac{\vec{\epsilon}_\perp \vec{k}_\perp}{\vec{k}_\perp^2 + x^2 m^2}, \tag{4.33a}$$

$$M_{1,1,0}^{\text{QCD}} = \frac{M_{1,\text{el}}^{\text{QCD}}}{T_{A'B'}^c T_{C'D'}^c} \cdot (-2g) \cdot (T^g T^f)_{AB} T_{CD}^f \cdot \frac{-\vec{\epsilon}_\perp (\vec{k}_\perp - x\vec{q}_\perp)}{(\vec{k}_\perp - x\vec{q}_\perp)^2 + x^2 m^2}, \tag{4.33b}$$

$$M_{1,0,1}^{\text{QCD}} = \frac{M_{1,\text{el}}^{\text{QCD}}}{T_{A'B'}^c T_{C'D'}^c} \cdot (-2g) \cdot [T^f, T^g]_{AB} T_{CD}^f \cdot \frac{-\vec{\epsilon}_\perp (\vec{k}_\perp - \vec{q}_\perp)}{(\vec{k}_\perp - \vec{q}_\perp)^2 + x^2 m^2}. \tag{4.33c}$$

They build the basis for our further discussion. In the limit of massless quarks we recover the well-known expressions which were firstly derived by Gunion and Bertsch (see Eqs. (12a-c) in [Gun82] or Eqs. (D.9), (D.12) and (D.21) in Appendix D). Compared to Gyulassy, Levai and Vitev the equations (4.33a)-(4.33c) generalize the terms (53)-(55) in [Gyu00a] besides constant factorisation factors in the region $|\vec{k}_\perp| \gg x|\vec{q}_\perp|$. Further, in [Gyu00a] the additional influence of the production amplitude M_J Eq. (6) has to be neglected using the limit $t_0 \rightarrow -\infty$ for reasons of identification. Also, the remaining common exponentials there can be neglected, since only phase differences count.

4.2 Radiation Amplitude in QED

The expressions for the one-photon emission process in a single potential scattering event are obtained if the relevant colour group is reduced to $U(1)$, thus the colour factors are set to unity. Since a photon triple-vertex is absent in QED, the total matrix element in first order equals the sum of the pre- and post-emission diagrams, Figs. 4.2 and 4.3,

$$M_{1,\text{rad}}^{\text{QED}} = M_{1,0,0}^{\text{QED}} + M_{1,1,0}^{\text{QED}}. \tag{4.34}$$

This will be discussed under the conditions which we have already prepared. It is important to note that in the limit $x \rightarrow 0$, which will be applied in the case of QCD, the approximate total matrix element

$$M_{1,\text{rad}}^{\text{QED}} = M_{1,\text{el}}^{\text{QED}} \cdot (-2g) \left(\frac{\vec{\epsilon}_\perp \vec{k}_\perp}{\vec{k}_\perp^2 + x^2 m^2} - \frac{\vec{\epsilon}_\perp (\vec{k}_\perp - x\vec{q}_\perp)}{(\vec{k}_\perp - x\vec{q}_\perp)^2 + x^2 m^2} \right) \tag{4.35}$$

vanishes due to the destructive interference of the pre- and post-emission diagrams. Let us therefore consider the case of small x in some detail.

Note, that in the limits $m \rightarrow 0$ of light particles and $|\vec{k}_\perp| \gg x|\vec{q}_\perp|$ it is even possible to carry out the sum Eq. (4.35), whereby in doing so the often quoted standard expression

$$\overline{|M_{1,\text{rad}}^{\text{QED}}|^2} \rightarrow |M_{1,\text{el}}^{\text{QED}}|^2 \cdot 4g^2 \cdot \frac{x^2 \vec{q}_\perp^2}{\vec{k}_\perp^2 (\vec{k}_\perp - x\vec{q}_\perp)^2} \quad (4.36)$$

is obtained, in accordance with Eq. (6) in [Gun82], and thus corresponds to the Bethe-Heitler photon cross section in QED in the limit of high energies (Eq. (19) [Kov03]).

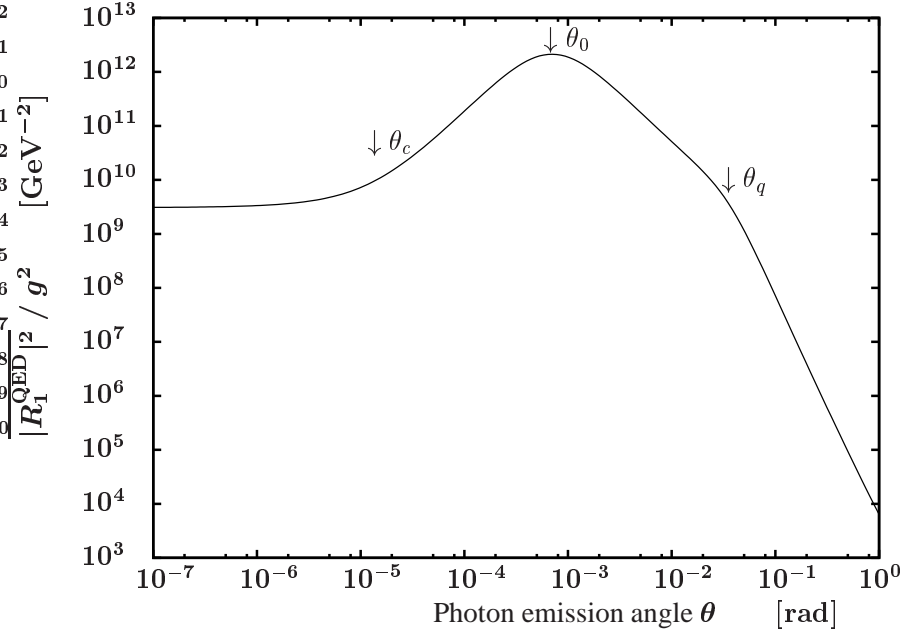


Figure 4.5: Radiation amplitude $\overline{|R_1^{\text{QED}}|^2}$ of a light particle as a function of θ for $m < |\vec{q}_\perp|$, i.e. $\theta_0 < \theta_q$. The chosen parameters are $m_d = 0.007$ GeV, $\vec{p}_i = (0, 0, 10)$ GeV, $\vec{p}_{f\perp} = (0.3, 0.2)$ GeV, $\mu = 0.5$ GeV, $\omega = 0.001$ GeV, $\phi = \pi/2$. The angle marks lie at $\theta_c = 1.4 \cdot 10^{-5}$, $\theta_0 = 7 \cdot 10^{-4}$ and $\theta_q = 3.6 \cdot 10^{-2}$. The position of the peak is determined by the non-vanishing particle mass, which further screens the infrared divergence in the $m \rightarrow 0$ limit.

We consider the behaviour of this matrix element for different regions of the photon emission angle θ . Suppose this angle lies in a region where $k_\perp \gg xq_\perp$, so one can expand the second term for small $x\vec{q}_\perp$ in Eq. (4.35),

$$M_{1,\text{rad}}^{\text{QED}} = M_{1,0,0}^{\text{QED}} + M_{1,1,0}^{\text{QED}} \Big|_{x\vec{q}_\perp=0} + \frac{\partial}{\partial(x\vec{q}_\perp)} M_{1,1,0}^{\text{QED}} \Big|_{x\vec{q}_\perp=0} \cdot x\vec{q}_\perp, \quad (4.37)$$

and obtains the first expansion contribution as remainder

$$M_{1,\text{rad}}^{\text{QED}} = M_{1,\text{el}}^{\text{QED}} \cdot (-2g) \cdot \frac{x}{\vec{k}_\perp^2 + x^2 m^2} \left(\vec{\epsilon}_\perp \vec{q}_\perp + \frac{2(\vec{\epsilon}_\perp \vec{k}_\perp)(\vec{k}_\perp \vec{q}_\perp)}{\vec{k}_\perp^2 + x^2 m^2} \right). \quad (4.38)$$

Hence, the squared and summed radiation amplitude

$$\overline{|R_1^{\text{QED}}|^2} = 4g^2 \cdot \frac{x^2}{(\vec{k}_\perp^2 + x^2 m^2)^2} \left[\vec{q}_\perp^2 + \frac{2(\vec{k}_\perp \vec{q}_\perp)^2}{(\vec{k}_\perp^2 + x^2 m^2)} + \frac{\vec{k}_\perp^2 (\vec{k}_\perp \vec{q}_\perp)^2}{(\vec{k}_\perp^2 + x^2 m^2)^2} \right], \quad (4.39)$$

implies a dependence proportional to $1/(\omega^2\theta^4)$ for angles and parameters which satisfy

$$|\vec{k}_\perp| \gg x|\vec{q}_\perp|, \quad (4.40a)$$

$$|\vec{k}_\perp| \gg xm^2. \quad (4.40b)$$

For small emission angles, $\sin \theta \approx \theta$, these conditions can be summarized by

$$\theta \gg \max(\theta_0, \theta_q), \quad (4.41)$$

where we have defined the angles

$$\theta_q \equiv \frac{|\vec{q}_\perp|}{E}, \quad (4.42a)$$

$$\theta_0 \equiv \frac{m}{E}. \quad (4.42b)$$

Note, that $\theta_0 = 1/\gamma$, where $\gamma = (1 - v^2)^{-1/2}$ for a particle with the velocity v , relates the so-called dead cone angle θ_0 , see Section 2.2, to the well-known relativistic factor γ .

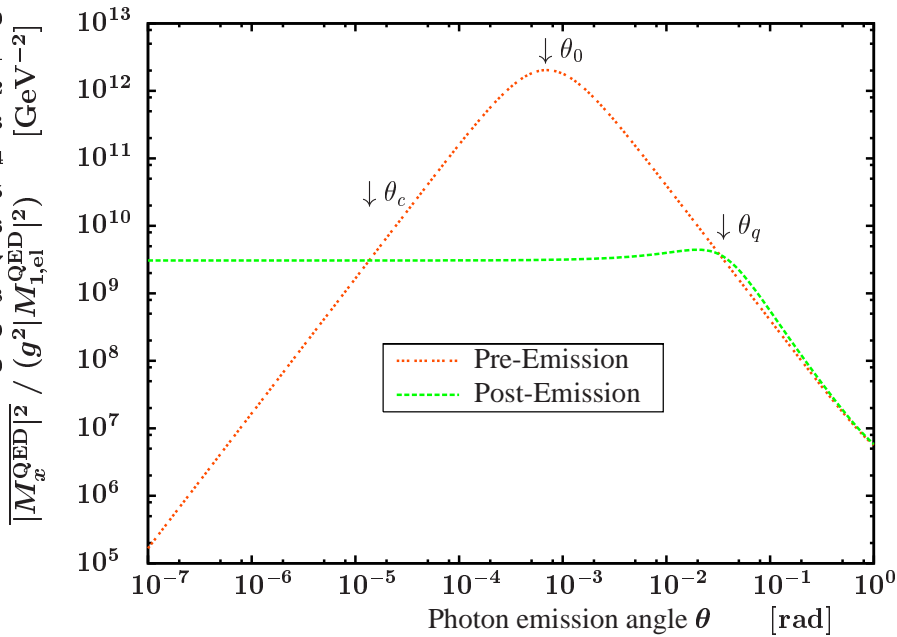


Figure 4.6: Contributions of individual diagrams to the total result depicted in Fig. 4.5. In the region $\theta > \theta_q$, the pre- and post-emission contributions interfere destructively to yield the $1/(\omega^2\theta^4)$ slope of the total radiation amplitude depicted in Fig. 4.5. For $\theta_c < \theta < \theta_q$ the pre-emission term dominates causing the $1/(\omega^2\theta^2)$ behaviour in the interval $\theta_0 < \theta < \theta_q$, while in the interval $\theta_c < \theta < \theta_0$ the amplitude (4.43) delivers the dependence $\sim \theta^2/\omega^2$. At $\theta < \theta_c$ the constant post-emission term dominates.

In Figs. 4.5 and 4.7 the numerically calculated exact radiation amplitude $\overline{|R_1^{\text{QED}}|^2}$ is exhibited for two kinematical situations. Fig. 4.5 refers to the case $\theta_0 < \theta_q$, while Fig. 4.7 shows the situation for the reversed case, $\theta_q < \theta_0$. These situations are qualitatively different and therefore we classify them as light and heavy particle cases, although by a suitable choice of the momentum transfer this classification of course does not only depend on the quark mass. Both figures reveal the $1/(\omega^2\theta^4)$ shape at $\theta \gg \max(\theta_0, \theta_q)$.

In the situation $\theta_0 < \theta_q$, for angles $\theta_0 < \theta < \theta_q$ the dominant fraction in R_1^{QED} is given by the pre-emission process, i. e. $M_{1,0,0}^{\text{QED}}$ dominates. Hence, going to smaller angles, the previous $1/(\omega^2\theta^4)$ dependence turns into a $1/(\omega^2\theta^2)$ dependence at $\theta \approx \theta_q$, as can be seen in Fig. 4.5. Indeed, in this regime, the radiation amplitude is

$$\overline{|R_1^{\text{QED}}|^2} = 4g^2 \cdot \frac{\vec{k}_\perp^2}{(\vec{k}_\perp^2 + x^2 m^2)^2}. \quad (4.43)$$

The radiation amplitude becomes peaked at the angle θ_0 . For angles below θ_0 the denominator in Eq. (4.43) becomes constant and the radiation amplitude depicted in Fig. 4.5 turns in a θ^2/ω^2 behaviour. Obviously, the term (4.43) would tend to zero, but for angles even less, $\theta \ll \theta_c$, where θ_c is introduced as

$$\theta_c \equiv \frac{m^2}{|\vec{q}_\perp|E}, \quad (4.44)$$

the constant post-emission part now becomes relevant and yields an $1/\omega^2$ dependence. This is illustrated by the crossing at θ_c in Fig. 4.6, where the individual contributions are displayed. Note, that the angles we have defined so far in Eqs. (4.42a), (4.42b) and (4.44) are not independent, since

$$\theta_c = \frac{\theta_0^2}{\theta_q} \Rightarrow \begin{cases} \theta_c < \theta_0 & \text{for } \theta_0 < \theta_q, \\ \theta_c > \theta_0 & \text{for } \theta_0 > \theta_q. \end{cases} \quad (4.45)$$

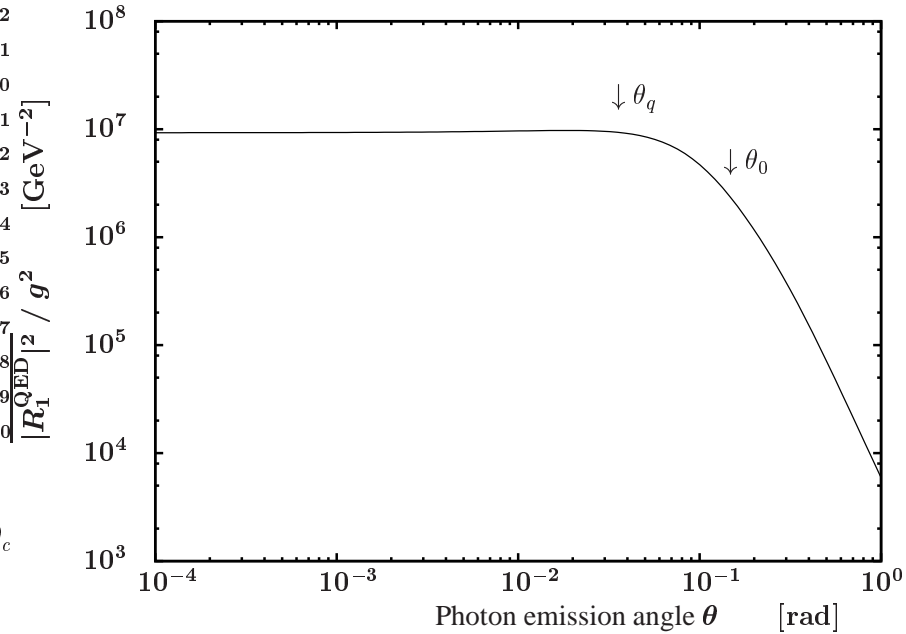


Figure 4.7: As Fig. 4.5, but for a heavier particle so that $m > |\vec{q}_\perp|$, i.e. $\theta_q < \theta_0$. The parameters are as in Fig. 4.5, except that $m_c = 1.5$ GeV. The angle marks lie at $\theta_0 = 0.15$ and $\theta_q = 3.6 \cdot 10^{-2}$.

It remains to comment on the reverse case with $\theta_q < \theta_0$, which is exhibited in Fig. 4.7. Here, the expansion in Eq. (4.38) holds true for all angles above θ_0 and the $1/(\omega^2\theta^4)$ behaviour is approached

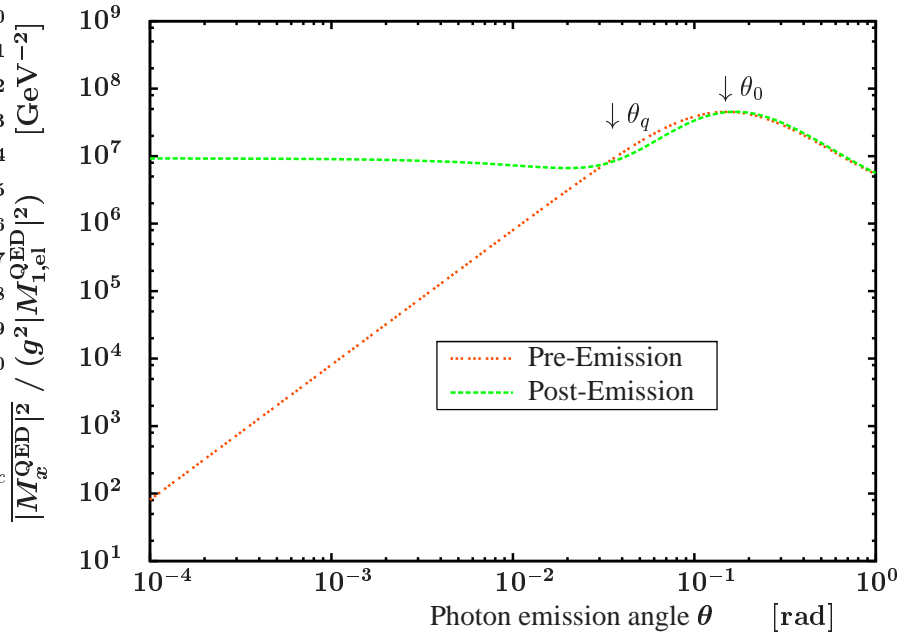


Figure 4.8: Contributions of individual diagrams to the total result in Fig. 4.7. The destructive interference of pre- and post-emission amplitudes occurs for $\theta > \theta_q$, as in Fig. 4.6, but due to $\theta_q < \theta_0$ the radiation pattern is changed, as seen in comparing Figs. 4.5 and 4.7.

in the whole range $\theta > \theta_0$.³ For angles below θ_0 , but still larger than θ_q , the radiation pattern is implied by Eq. (4.39) which has a maximum for parallel or anti-parallel orientation of the transverse photon momentum \vec{k}_\perp and the perpendicular momentum transfer \vec{q}_\perp from the potential. It can be shown that for smaller angles a constant behaviour occurs due the always dominating post-emission term for $m > |\vec{q}_\perp|$, as shown in Fig. 4.8. This again yields a result

$$|\overline{R_1^{\text{QED}}}|^2 = 4g^2 \cdot \frac{\vec{q}_\perp^2}{x^2 m^4} \sim \frac{1}{\omega^2} \quad \text{for } \theta < \theta_q. \quad (4.46)$$

In summary, the important feature of this discussion is that the QED radiation amplitude in light and heavy projectile situations is qualitatively different depending on the ratio of m and $|\vec{q}_\perp|$. For smaller m a maximum occurs, otherwise the pre- and post-emission diagrams interfere destructively and no peak is exhibited. From an analytical point, the angle θ_q describes the validity range of the expansion Eq. (4.37), so one can interpret θ_q as borderline between the destructive interference regime above θ_q and the domain $\theta < \theta_q$, where single diagrams dominate.

Comparing Figs. 4.5 and Figs. 4.7 reveals that the emission pattern of a heavy particle differs from that of a light particle: The radiation of a heavy particle is suppressed at angles $\theta < \theta_q$. This is the famous "dead cone" effect.

4.3 Radiation Amplitude in QCD

One difference between QED and QCD is the colour structure. We want to distinguish the effect of colour factors from the influence of additional non-abelian diagrams. Therefore we begin the

³Strictly we should write $\theta \gg \theta_0$ instead of $\theta > \theta_0$ which explains that the numerical result in Fig. 4.7 does not show the exact predicted behaviour. For convenience we will not always emphasise throughout the discussions in this chapter that estimates are valid for angles much smaller or greater than typical values.

discussion with the abelian diagrams in QCD.

4.3.1 Abelian Diagrams

The abelian total matrix element, like in QED, is found as sum of the pre- and post-emission matrix elements

$$M_{1,\text{rad}}^{\text{abel.QCD}} = M_{1,0,0}^{\text{QCD}} + M_{1,1,0}^{\text{QCD}}, \quad (4.47)$$

but the additional feature of colour factors essentially changes the analogue discussion from QED. Figs. 4.9 and 4.11 exhibit the numerically evaluated results for two kinematical situations which we are going to discuss. The approximate total matrix element now reads

$$M_{1,\text{rad}}^{\text{abel.QCD}} = \frac{M_{1,\text{el}}^{\text{QCD}}}{T_{A'B'}^c T_{C'D'}^c} \cdot (-2g) \left((T^f T^g)_{AB} T_{CD}^f \cdot \frac{\vec{\epsilon}_\perp \vec{k}_\perp}{\vec{k}_\perp^2 + x^2 m^2} - (T^g T^f)_{AB} T_{CD}^f \cdot \frac{\vec{\epsilon}_\perp (\vec{k}_\perp - x \vec{q}_\perp)}{(\vec{k}_\perp - x \vec{q}_\perp)^2 + x^2 m^2} \right), \quad (4.48)$$

under the kinematical and gauge constraints which we have already supplied. As in the QED case one may carry out the sum of matrix elements and the polarization sum of the squared total matrix element for $m \rightarrow 0$ and $|\vec{k}_\perp| \gg x |\vec{q}_\perp|$ to yield

$$|M_{1,\text{rad}}^{\text{abel.QCD}}|^2 \rightarrow |M_{1,\text{el}}^{\text{QCD}}|^2 \cdot 4g^2 \cdot \frac{|[T^f, T^g]_{AB} T_{CD}^f|^2}{|T_{A'B'}^c T_{C'D'}^c|^2} \cdot \frac{1}{\vec{k}_\perp^2}. \quad (4.49)$$

Similarly to the QED argument we focus on different regions of the gluon emission angle θ at fixed gluon energy ω . Angles greater than $|\vec{q}_\perp|/E$, i.e. $\theta_q < \theta$, allow to reduce Eq. (4.48) to

$$M_{1,\text{rad}}^{\text{abel.QCD}} = \frac{M_{1,\text{el}}^{\text{QCD}}}{T_{A'B'}^c T_{C'D'}^c} \cdot (-2g) \cdot \frac{\vec{\epsilon}_\perp \vec{k}_\perp}{\vec{k}_\perp^2 + x^2 m^2} \left((T^f T^g)_{AB} T_{CD}^f - (T^g T^f)_{AB} T_{CD}^f \right), \quad (4.50)$$

where the colour structure factors out and can even be summarized into a colour commutator

$$M_{1,\text{rad}}^{\text{abel.QCD}} = \frac{M_{1,\text{el}}^{\text{QCD}}}{T_{A'B'}^c T_{C'D'}^c} \cdot (-2g) \cdot \frac{\vec{\epsilon}_\perp \vec{k}_\perp}{\vec{k}_\perp^2 + x^2 m^2} \cdot [T^f, T^g]_{AB} T_{CD}^f. \quad (4.51)$$

This leads to the occurrence of the common dead cone factor Eq. (2.1), which we have introduced in Section 2.2 as stated by Dokshitzer and Kharzeev, multiplied by a colour constant

$$\overline{|R_1^{\text{abel.QCD}}|^2} = 4g^2 \cdot \frac{\vec{k}_\perp^2}{(\vec{k}_\perp^2 + x^2 m^2)^2} \cdot C_A, \quad (4.52)$$

where the colour part, see also Eq. (A.16), arises from

$$\overline{|[T^f, T^g]_{AB} T_{CD}^f|^2} = C_{1,\text{el}} \cdot C_A. \quad (4.53)$$

In the limit of massless projectile particles, $m \rightarrow 0$, the radiation amplitude becomes proportional to $1/\vec{k}_\perp^2$, that is to say an infrared divergence emerges. An advantage of the calculation in the massive case is that collinear divergences are ruled out, see section 3.4. It is important to note that

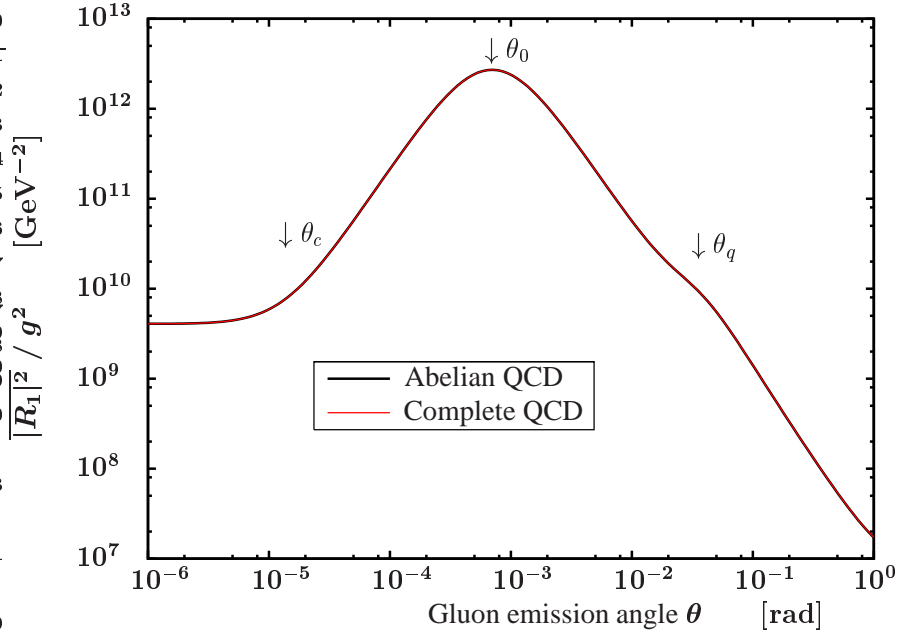


Figure 4.9: Radiation amplitude $\overline{|R_1|^2}$ of a light particle as a function of θ for $m < |\vec{q}_\perp|$. The parameters and angle marks are as in Fig. 4.5. The abelian QCD calculation agrees with the results for the full set of diagrams. The occurrence of colours interestingly modifies the pattern in Fig. 4.5. For $\theta > \theta_q$, instead of the bending at θ_q , the slope remains constant but the curve is shifted upwards by $9/4$.

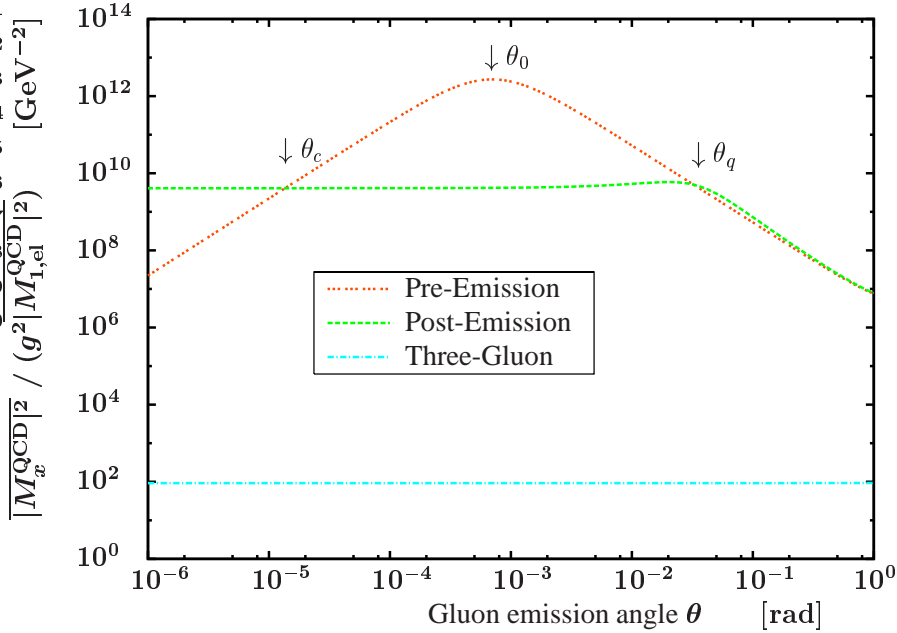


Figure 4.10: Contributions of individual diagrams to the total results in Fig. 4.9. The three-gluon contribution is suppressed by orders of magnitude and so the full QCD result does not deviate from the abelian QCD radiation amplitude.

the argument for the appearance of the dead cone peak, explained in Fig. 2.5, as in Eq. (4.52) is restricted to a kinematical situation where $|\vec{q}_\perp| < m$. Otherwise, for $\theta_0 < \theta_q$, angles $\theta > \theta_q$ are automatically out of the range around θ_0 .

Firstly, we will proceed to focus on this case, $m < |\vec{q}_\perp|$ or $\theta_0 < \theta_q$, respectively, as exhibited in Fig. 4.9. Here, the dead cone formula explains the $1/(\omega^2\theta^2)$ decrease for $\theta > \theta_q$, but its derivation does not cover the region $\theta_0 < \theta < \theta_q$. For such angles the pre-emission diagram is dominant and predicts an averaged and summed squared radiation amplitude

$$\overline{|R_1^{\text{abel.QCD}}|^2} = 4g^2 \cdot \frac{\vec{k}_\perp^2}{(\vec{k}_\perp^2 + x^2m^2)^2} \cdot C_F, \quad (4.54)$$

and a dead cone formula is recovered. However, another colour factor is relevant because only one projectile colour structure, namely the post-emission diagram, is taken into account, see Eq. (A.15),

$$\overline{|(T^f T^g)_{AB} T_{CD}^f|^2} = \overline{|(T^g T^f)_{AB} T_{CD}^f|^2} = C_{1,\text{el}} \cdot C_F. \quad (4.55)$$

Note, that the expressions Eq. (4.52) for $\theta > \theta_q$ and Eq. (4.54) for $\theta < \theta_q$, respectively, differ only in the colour part, which explains the relative shift by a factor $C_F/C_A = 4/9$ from greater to smaller θ near θ_q in Fig. 4.9. The plot Fig. 4.10 demonstrates how the post-emission diagram again dominates small angles below θ_c and thus the radiation amplitude

$$\overline{|R_1^{\text{abel.QCD}}|^2} = 4g^2 \cdot \frac{1}{x^2\vec{q}_\perp^2} \cdot C_F \quad (4.56)$$

in Fig. 4.9 becomes constant, where we made use of $\theta_c < \theta_0$ for $\theta_0 < \theta_q$ as in Eq. (4.45).

We allude again that the squared individual amplitudes, compare Figs. 4.10 and 4.6, are very similar in the QED and abelian QCD case, but due to different interference effects from the colour factors, the total radiation in the region of $\theta > \theta_q$ differs significantly; at $\theta < \theta_q$ the radiation patterns are similar.

Let us now consider the second case, when $|\vec{q}_\perp| < m$, i.e. $\theta_q < \theta_0$, which is illustrated in Fig. 4.11. From Eq. (4.52) one finds a $1/(\omega^2\theta^2)$ dependence for $\theta > \theta_0$ and a θ^2/ω^2 slope for $\theta < \theta_0$. This typical dead cone behaviour is replaced by a constant $1/\omega^2$ behaviour in Fig. 4.11,

$$\overline{|R_1^{\text{abel.QCD}}|^2} = 4g^2 \cdot \frac{\vec{q}_\perp^2}{x^2m^4} \cdot C_F, \quad (4.57)$$

which follows from Eq. (4.48) for angles $\theta < \theta_q$. This is, like in QED, due to the dominance of the post-emission process as shown in Fig. 4.12.

Fig. 4.11 highlights the striking importance of the colour factors: The radiation pattern differs significantly from that exhibited in Fig. 4.7 for the same kinematics. In contrast, the individual squared amplitudes are rather similar, except small differences due to the colour factors, see Figs. 4.12 and 4.8.

4.3.2 Non-Abelian Diagrams

We continue to discuss to which degree the three-gluon vertex diagram Fig. 4.4 contributes and how it may change the behaviour of the abelian QCD single scattering radiation amplitude. In fact, the results for the kinematical situations considered so far for abelian diagrams are not effected by the additional three-gluon vertex diagram. The statement that this contribution is negligible is already

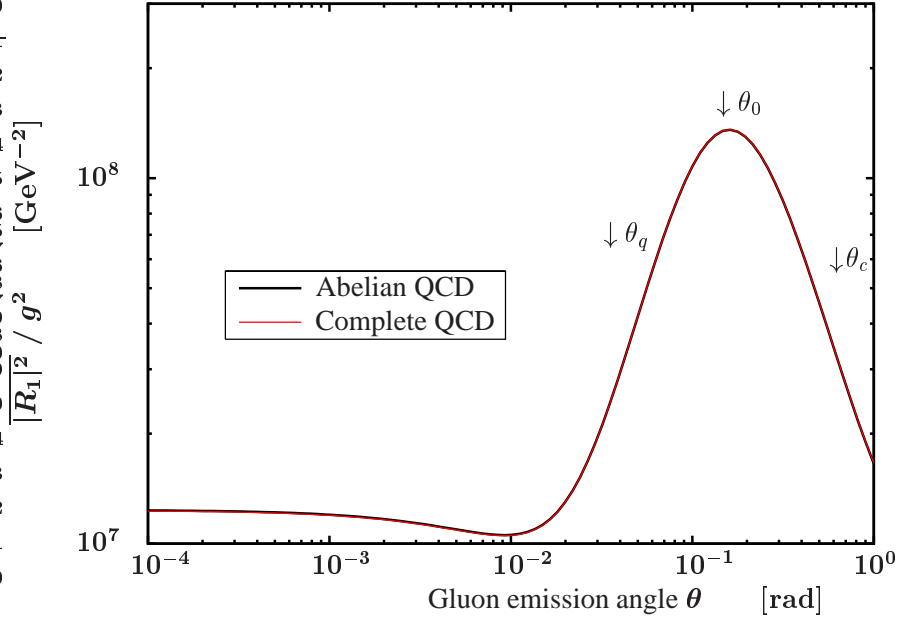


Figure 4.11: Radiation amplitude $\overline{|R_1|^2}$ of a heavy particle as a function of θ for the case $m > |\vec{q}_\perp|$. The parameters are as in Fig. 4.7, the additional typical angles are $\theta_c = 0.63$ and $\theta_{3\text{glu}} = 36$. Again, there are no differences between $\overline{|R_1^{\text{abel.QCD}}|^2}$ and $\overline{|R_1^{\text{QCD}}|^2}$. The pattern dramatically differs from the QED calculation, since a dead cone behaviour is developed.

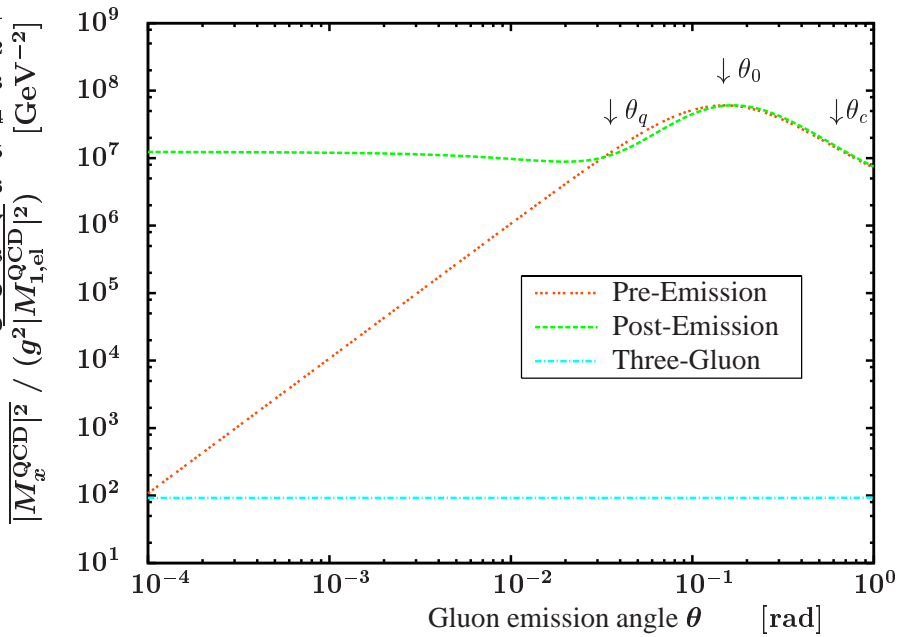


Figure 4.12: Contributions of individual diagrams to the total result in Fig. 4.11. The differences compared to Fig. 4.8 arise from colour factors.

numerically verified in Figs. 4.10 and 4.12, and indeed the complete QCD radiation amplitude is given by the abelian approach, which is fairly well confirmed by Figs. 4.9 and 4.11. We explore now the relevant regions, where the non-abelian part modifies the gluon radiation characteristic. Within the full QCD result, derived with the approximations given in Section 4.1,

$$M_{1,\text{rad}}^{\text{QCD}} = \frac{M_{1,\text{el}}^{\text{QCD}}}{T_{A'B'}^c T_{C'D'}^c} \cdot (-2g) \left((T^f T^g)_{AB} T_{CD}^f \cdot \frac{\vec{\epsilon}_\perp \vec{k}_\perp}{\vec{k}_\perp^2 + x^2 m^2} - (T^g T^f)_{AB} T_{CD}^f \cdot \frac{\vec{\epsilon}_\perp (\vec{k}_\perp - x \vec{q}_\perp)}{(\vec{k}_\perp - x \vec{q}_\perp)^2 + x^2 m^2} - [T^f, T^g]_{AB} T_{CD}^f \cdot \frac{\vec{\epsilon}_\perp (\vec{k}_\perp - \vec{q}_\perp)}{(\vec{k}_\perp - \vec{q}_\perp)^2 + x^2 m^2} \right), \quad (4.58)$$

the extra term with respect to the abelian case, the three-gluon contribution, suggests to define an additional typical angle

$$\theta_{3\text{glu}} \equiv \frac{|\vec{q}_\perp|}{\omega} = \frac{|\vec{q}_\perp|}{E} \frac{E}{\omega} = \theta_q/x. \quad (4.59)$$

This implies

$$\theta_{3\text{glu}} > \theta_q, \quad (4.60)$$

that is to say this new angle is always greater than the characteristic angle θ_q , which was introduced to discuss the importance of the post-emission diagram.

Again the sum of matrix elements in connection with the polarization sum recovers the well-known expressions (cf. Eqs. (15), (16) in [Gun82], also cf. Eqs. (17) in [Kov03] and (3.32) in [Wie00b]),

$$|M_{1,\text{rad}}^{\text{QCD}}|^2 \rightarrow |M_{1,\text{el}}^{\text{QCD}}|^2 \cdot 4g^2 \cdot \frac{|[T^f, T^g]_{AB} T_{CD}^f|^2}{|T_{A'B'}^c T_{C'D'}^c|^2} \cdot \frac{\vec{q}_\perp^2}{\vec{k}_\perp^2 (\vec{k}_\perp - \vec{q}_\perp)^2}, \quad (4.61)$$

supposed $m \rightarrow 0$ and $|\vec{k}_\perp| \gg x|\vec{q}_\perp|$.

As long as

$$|\vec{q}_\perp| > \omega, \quad (4.62)$$

that is to say $\theta_{3\text{glu}} > 1$, the gluon emission angle θ is always smaller than $\theta_{3\text{glu}}$. We will explain analytically, when, under the weaker condition

$$\theta < \theta_{3\text{glu}}, \quad (4.63)$$

the three-gluon vertex diagram might be omitted to obtain the complete QCD result. The inequality Eq. (4.63) implies that \vec{k}_\perp is small with respect to \vec{q}_\perp , which is why the three gluon term becomes constant,

$$\overline{|R_{1,\text{no colour}}^{\text{threeGluon}}|^2} = 4g^2 \cdot \frac{\vec{q}_\perp^2}{(\vec{q}_\perp^2 + x^2 m^2)^2}, \quad (4.64)$$

for fixed potential momentum transfer and gluon energy. Note, that due to the condition $|\vec{q}_\perp| > \omega$, the effect of k in the four-momentum conservation Eq. (4.9) is negligible. We will disregard the colour parts in the following discussion.

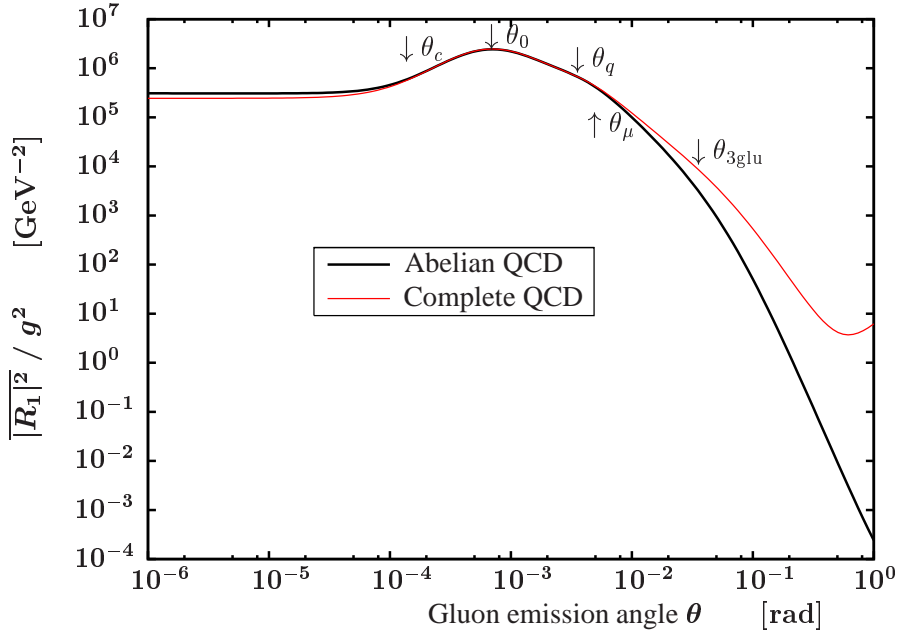


Figure 4.13: Radiation amplitude $\overline{|R_1|^2}$ as a function of θ , which reflects the changes for $\theta > \theta_{3\text{glu}}$. The parameters are chosen for $\theta_{3\text{glu}} < 1$, so that $\theta_{3\text{glu}} < \theta$ is possible, $m_d = 0.007$ GeV, $\vec{p}_i = (0, 0, 10)$ GeV, $\vec{p}_{f\perp} = (0.03, 0.02)$ GeV, $\mu = 0.05$ GeV, $\omega = 1$ GeV, $\phi = \pi/2$. The angle marks lie at $\theta_c = 1.4 \cdot 10^{-4}$, $\theta_0 = 7 \cdot 10^{-4}$, $\theta_q = 3.6 \cdot 10^{-3}$, $\theta_\mu = 5 \cdot 10^{-3}$ and $\theta_{3\text{glu}} = 3.6 \cdot 10^{-2}$. For $\theta < \theta_{3\text{glu}}$ the radiation pattern is due to the abelian diagrams and has the same form as in Fig. 4.9 but the θ^2 or θ^{-2} slopes are not visible since the window around θ_0 is too small and for $\theta < \theta_c$ the constant behaviour sets in. However a small shift in this range is caused by the three-gluon term. A drastic difference appears for $\theta > \theta_{3\text{glu}}$, refer also to Figs. 4.14 and 4.17 - 4.22.

For the case $\theta_0 < \theta_q$, a comparison of Eq. (4.64) with the relevant abelian QCD results Eqs. (4.52) in the regime $\theta > \theta_q$, as well as (4.54) for $\theta_0 < \theta < \theta_q$ yields

$$\frac{\vec{q}_\perp^2}{(\vec{q}_\perp^2 + x^2 m^2)^2} < \frac{\vec{k}_\perp^2}{(\vec{k}_\perp^2 + x^2 m^2)^2}, \quad (4.65)$$

for $\theta > \theta_0$, due to

$$\frac{1}{\vec{q}_\perp^2} < \frac{1}{\vec{k}_\perp^2},$$

$$\theta < \theta_{3\text{glu}}.$$

Here, $\theta_{3\text{glu}} > \theta_0$, required for approximations in the three-gluon term, $\vec{q}_\perp^2 > x^2 m^2$, is realized by our assumptions.

Also, in the region of lower angles, $\theta_c < \theta < \theta_0$, Eq. (4.54) shows due to

$$\frac{1}{\vec{q}_\perp^2} < \frac{\vec{k}_\perp^2}{x^4 m^4}, \quad (4.66)$$

which is equivalent to

$$x\theta_c < \theta,$$

that the three-gluon vertex is less important for the total result.

For angles $\theta < \theta_c$ the constant terms from post-emission Eq. (4.56) and three-gluon diagram Eq. (4.64) obey

$$\frac{1}{\vec{q}_\perp^2} < \frac{1}{x^2 \vec{q}_\perp'^2}, \quad (4.67)$$

since $x < 1$ and $\theta_0 < \theta_q$. In the situation of Fig. 4.9 the typical three-gluon angle $\theta_{3\text{glu}} = 3.6 \cdot 10^2$ is much greater than 1, or in other words Eq. (4.62) is true, therefore from the above derivation we understand why the abelian QCD approach is sufficient at least in this light particle situation. Also, in Figs. 4.13 and 4.14 one finds the abelian dominated radiation amplitude for a region of angles $\theta < \theta_{3\text{glu}}$. The deviations in Fig. 4.13 for angles $\theta > \theta_{3\text{glu}}$ are commented on in the next section.

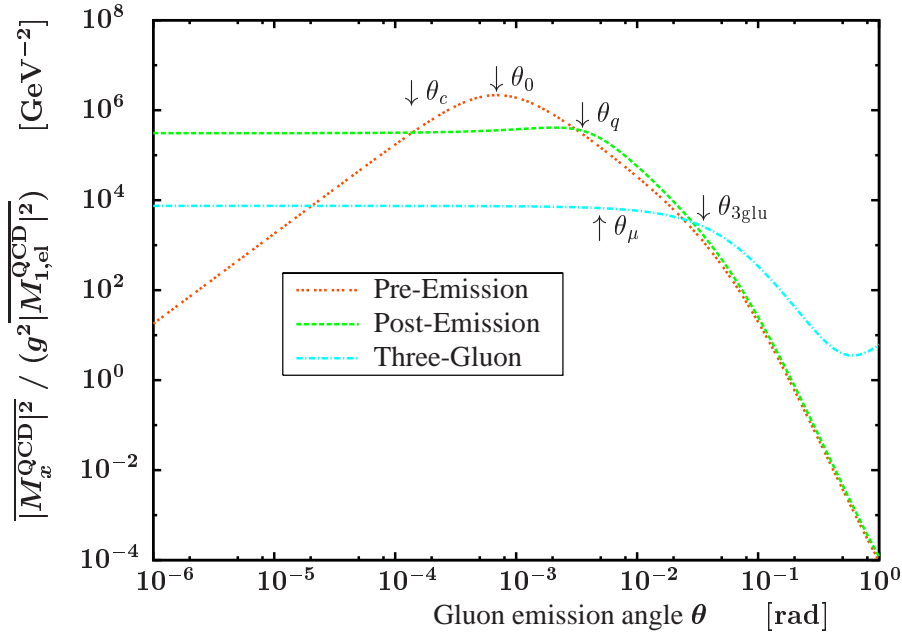


Figure 4.14: Contributions of individual diagrams to the total results in Fig. 4.13. The three-gluon term suppression for $\theta < \theta_{3\text{glu}}$ is not as strong as in Fig. 4.10 and causes some minor shift between the QCD and abelian QCD results. For $\theta > \theta_{3\text{glu}}$ clearly the specific non-abelian part dominates and yields the increase of the radiation amplitude compared to the abelian outcome in Fig. 4.13.

In the heavy particle situation, $|\vec{q}_\perp| < m$, one has to distinguish the cases $\theta_0 < \theta_{3\text{glu}}$ and vice versa. However, notice that a consideration of the radiation pattern at $\theta \approx \theta_0$ in the second case is not realizable in the very soft gluon limit Eq. (4.62), since $1 < \theta_{3\text{glu}} < \theta_0$ contradicts the precondition $m < E$. In the first situation, the previous approximation in Eq. (4.64) remains valid. Therefore, the explanations from the light particle paragraph can be repeated for $\theta > \theta_q$. If we look at $\theta < \theta_q$, here Eq. (4.57) leads to

$$\frac{1}{\vec{q}_\perp^2} < \frac{\vec{q}_\perp'^2}{x^2 m^4}, \quad (4.68)$$

for $\theta_c < \theta_{3\text{glu}}$ and the non-abelian part becomes negligible, too, under this additional restriction. This is exactly the situation in Figs. 4.11 and 4.12, where our estimates explain, why the abelian and complete QCD calculations are in agreement to very good accuracy.

Otherwise, for $\theta_c > \theta_{3\text{glu}}$, we again predict a constant behaviour of the radiation amplitude but at the total value

$$\overline{|R_1^{\text{QCD}}|^2} = 4g^2 \cdot \frac{1}{\vec{q}_\perp^2} \cdot C_A, \quad (4.69)$$

instead of Eq. (4.57).

On the other side, for $\theta_{3\text{glu}} < \theta_0$, which belongs to the heavy particle case since $\theta_q < \theta_{3\text{glu}} < \theta_0$, Eq. (4.60), the three-gluon term can be simplified,

$$\overline{|R_{1,\text{no colour}}^{\text{threeGluon}}|^2} = 4g^2 \cdot \frac{\vec{q}_\perp^2}{x^4 m^4}, \quad (4.70)$$

and compared to the corresponding radiation amplitudes from abelian QCD. Note, that $\theta_{3\text{glu}} < \theta_0$ implies the angular ordering $\theta_q < \theta_{3\text{glu}} < \theta_0 < \theta_c$, and that, furthermore, the chosen parameters should allow for $\theta_{3\text{glu}} < 1$. The case $\theta > \theta_0$ is excluded because we investigate $\theta < \theta_{3\text{glu}}$. In the angular interval $\theta_q < \theta < \theta_{3\text{glu}}$ Eqs. (4.70) and (4.52) give

$$\frac{\vec{q}_\perp^2}{x^4 m^4} > \frac{\vec{k}_\perp^2}{x^4 m^4}, \quad (4.71)$$

since $\theta_{3\text{glu}} > \theta$. This indicates that the radiation amplitude becomes constant

$$\overline{|R_1^{\text{QCD}}|^2} = 4g^2 \cdot \frac{\vec{q}_\perp^2}{x^4 m^4} \cdot C_A, \quad (4.72)$$

due to the three-gluon contribution. For $\theta < \theta_q$, by comparison with Eq. (4.57), we obtain

$$\frac{\vec{q}_\perp^2}{x^4 m^4} > \frac{\vec{q}_\perp^2}{x^2 m^4}, \quad (4.73)$$

since $x < 1$, which causes the previous constant behaviour Eq. (4.72). This pattern of the radiation amplitude is illustrated in Fig. 4.15 in the angular range $\theta < \theta_{3\text{glu}}$, where our discussion is valid. The opposite interval $\theta > \theta_{3\text{glu}}$ is explored in the next section.

Hence, we have demonstrated that the abelian QCD approach suffices to describe the radiation amplitude in the light particle situation $m < |\vec{q}_\perp|$, where $\theta_c < \theta_0 < \theta_q < \theta_{3\text{glu}}$, and for the selected heavy particle case $\theta_q < \theta_0 < \theta_c < \theta_{3\text{glu}}$, as long as the condition Eq. (4.63) is satisfied, which especially holds true in the very soft gluon situation Eq. (4.62). It was found, that in some heavy particle situations $m > |\vec{q}_\perp|$, namely for $\theta_q < \theta_{3\text{glu}} < \theta_0 < \theta_c$ and in the range of $\theta < \theta_q$ also for $\theta_q < \theta_0 < \theta_{3\text{glu}} < \theta_c$, the non-abelian diagram is the origin of a constant radiation amplitude independent of θ .

If we want to extend our discussion to the region $\theta > \theta_{3\text{glu}}$, it will be necessary to choose parameters which allow for $\theta_{3\text{glu}} < 1$. However, by the definition Eq. (4.9), the influence of k on q cannot be neglected anymore for fixed initial and final particle momenta. In other words, the momentum transfer in the kinematical situation for the radiation process begins to differ significantly from the corresponding value in the elastic scattering, which serves as reference system for the definition of the radiation amplitude. The factorisation, which was applied in the derivation of the matrix elements Eqs. (4.33a), (4.33b) and (4.33c), becomes insufficient. Therefore, we refer the consideration of this problematic θ range, which will turn out as mainly non-abelian dominated region, to the next section.

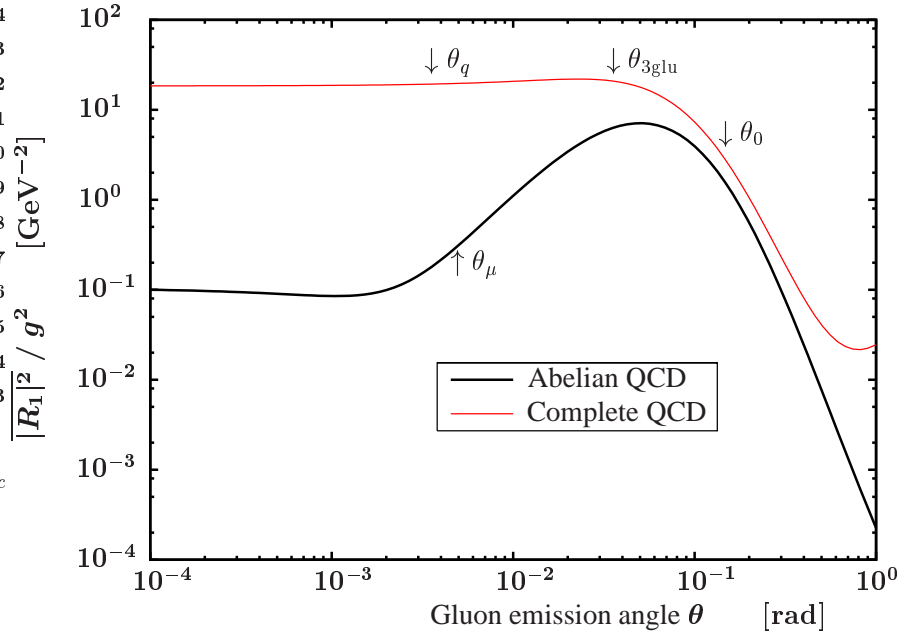


Figure 4.15: Radiation amplitude $|R_1^{\text{abel.QCD}}|^2$ of a heavy particle as a function of θ for the case $m > |\vec{q}_\perp|$. The parameters are as in Fig. 4.13 but with a mass $m_c = 1.5$ GeV instead. The characteristic angles are $\theta_q = 3.6 \cdot 10^{-3}$, $\theta_\mu = 5 \cdot 10^{-3}$, $\theta_{3\text{glu}} = 3.6 \cdot 10^{-2}$, $\theta_0 = 0.15$ and $\theta_c = 6.3$. The dead cone peak in the abelian result is shifted due to the reduction effect given by f_{kin} defined in Eq. (4.75).

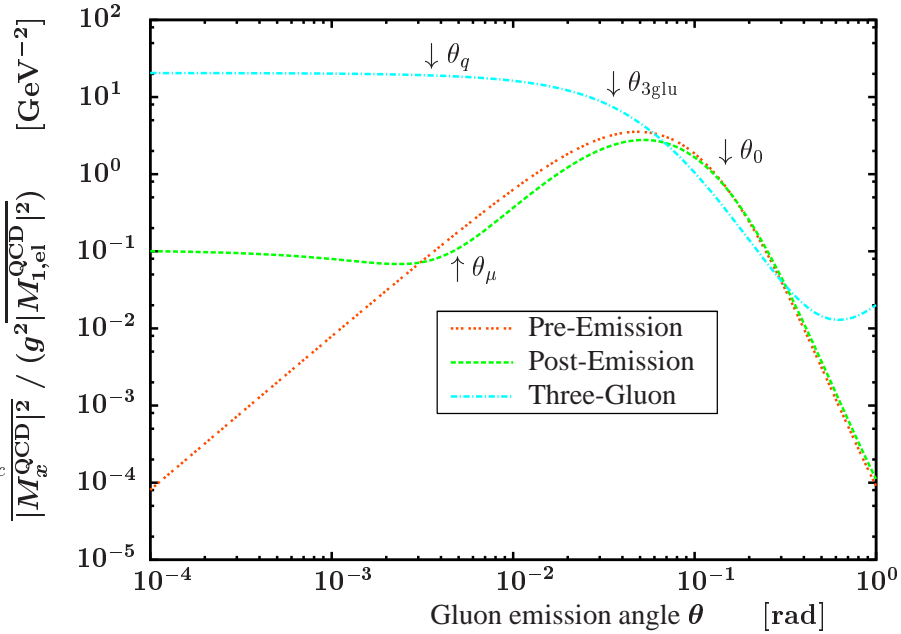


Figure 4.16: Contributions of individual diagrams to the total results in Fig. 4.15. Between θ_0 and $x\theta_c = 0.63$ the abelian diagrams are expected to be larger than the three-gluon contribution. The neglect of colour factors, which differ for abelian and non-abelian contributions by $C_A/C_F = \frac{9}{4}$ shifts this region.

4.4 Elastic Factorisation and Non-Abelian Contributions

We have already pointed out, how close the investigation of the radiation amplitude for angles $\theta > \theta_{3\text{glu}}$ is connected to the problem of the matrix element factorisation. As we commented on previously, if the very soft gluon case Eq. (4.62) is abandoned, which is essential to leave the predominantly abelian QCD situation, the gluon four-momentum k cannot be neglected with respect to the momentum transfer

$$q \equiv q_{\text{rad}} = p_f + k - p_i = q'_{\text{el}} + k, \quad (4.74a)$$

where the momentum transfer q'_{el} is given by

$$q'_{\text{el}} = p_f|_{\text{rad}} - p_i, \quad (4.74b)$$

and differs kinematically from the pure elastic momentum transfer

$$q_{\text{el}} = p_f|_{\text{el}} - p_i. \quad (4.74c)$$

Here, the momentum of the final quark state is determined by the on-shell condition with fixed transverse final momentum $\vec{p}_{f\perp}$ and additionally, in the radiative process, by the given gluon energy ω . It is therefore not allowed to factor out the denominator $(\vec{q}_{\text{rad}}^2 + \mu^2)$, which arises from the potential ansatz. Moreover one has to add a factor

$$f_{\text{kin}} \equiv \frac{\vec{q}'_{\text{el}}{}^2 + \mu^2}{\vec{q}_{\text{rad}}{}^2 + \mu^2} \quad (4.75)$$

to the expressions Eqs. (4.33a-4.33c) in order to correct this kinematical factorisation problem. Nevertheless, as long as $\mu > \omega$ no effect on the radiation amplitude appears, but otherwise this term f_{kin} , Eq. (4.75), alone is a source for an additional $1/(\omega^4\theta^4)$ dependence of the radiation amplitude, since

$$\vec{q}_{\text{rad}}{}^2 = (\vec{q}'_{\text{el}} + \vec{k})_{\perp}^2 + q_z^2 \approx \vec{k}_{\perp}{}^2 + \frac{\vec{k}_{\perp}{}^4}{4E^2x^2} = \omega^2 \sin^2 \theta \left(1 + \frac{\sin^2 \theta}{4 \cos^2(\theta/2)} \right) \approx \omega^2 \theta^2 \quad (4.76)$$

for small θ but with $\theta_{3\text{glu}} < \theta$.

Furthermore, we have to keep in mind the θ dependence of \vec{q}_{rad} for fixed p_i and p_f in the approximate matrix element expressions itself. In the definition of characteristic angles, Eqs. (4.42a), (4.44) and (4.59), $|\vec{q}_{\perp}|$ is to be understood as $|\vec{q}'_{\text{el}\perp}|$.

After these preliminary remarks we will turn the attention to the radiation amplitude for the case $\theta > \theta_{3\text{glu}}$. With this assumption, the three-gluon term

$$\overline{|R_1^{\text{threeGluon}}|^2} = 4g^2 \cdot \frac{\vec{q}'_{\text{el}\perp}{}^2}{(\vec{q}'_{\text{el}\perp}{}^2 + x^2 m^2)^2} \cdot C_A, \quad (4.77)$$

becomes constant and explains in combination with the kinematical correction factor f_{kin} the $1/(\omega^4\theta^4)$ dependence of the three-gluon contribution in Fig. 4.14. Of course, in the range $\theta > \theta_{3\text{glu}}$, also the predictions for abelian QCD situations and contributions are modified by this factor f_{kin} and have to be multiplied by $1/(\omega^4\theta^4)$.

It is of interest, where the non-abelian term Eq. (4.77) changes the abelian outcome besides the factor f_{kin} . Therefore, we consider the two distinct situations $\theta_0 < \theta_{3\text{glu}}$ and $\theta_{3\text{glu}} < \theta_0$ in order to simplify the expression Eq. (4.77).

Firstly, for $\theta_0 < \theta_{3\text{glu}} < \theta$, the term arising from the three-gluon contribution allows for a comparison with the abelian behaviour of the radiation amplitude

$$\frac{\vec{q}_{\text{el}\perp}^2}{(\vec{q}_{\text{el}\perp}^2 + x^2 m^2)^2} \approx \frac{1}{\vec{q}_{\text{el}\perp}^2} > \frac{1}{\vec{k}_{\perp}^2}, \quad (4.78)$$

due to $\theta > \theta_{3\text{glu}}$. Thus, $\theta > \theta_{3\text{glu}} > \theta_0$ is a non-abelian region, where the non-corrected matrix elements predict a constant radiation amplitude with respect to the gluon emission angle. One has to keep in mind, that the factor f_{kin} finally yields the behaviour proportional to $1/(\omega^4 \theta^4)$ as exhibited in Fig. 4.13 for $\theta > \theta_{3\text{glu}}$. The expected behaviour of the complete QCD result, as well as the predicted slope of $1/\theta^6$ for the abelian result, which is the product of the original $1/\theta^2$ behaviour and the correction dependence from f_{kin} , are only realized approximately. The deviations of our predictions from the correct outcome are depicted in Figs. 4.17 and 4.18 for the abelian and non-abelian case, respectively.

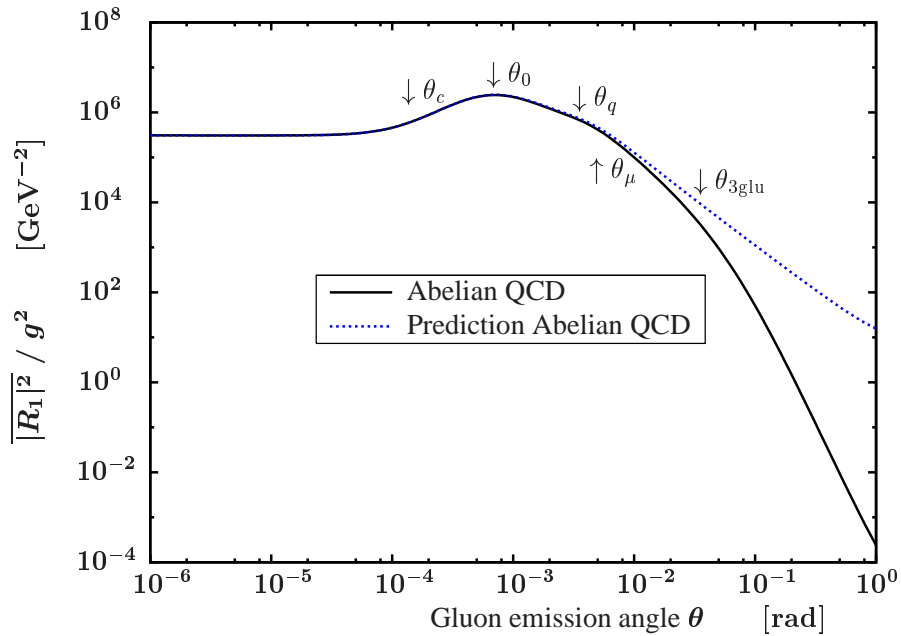


Figure 4.17: Comparison of the radiation amplitude from Fig. 4.13 in the abelian QCD approach to the corresponding prediction from Eq. (4.48) multiplied by the factor $(1 - x)$, which was neglected there. For $\theta > \theta_{3\text{glu}}$, the correction f_{kin} decreases the radiation pattern with respect to the prediction, see also Figs. 4.19 and 4.20. Thus the original $1/\theta^2$ slope becomes suppressed by $f_{\text{kin}} \sim 1/\theta^4$ and shows an approximate $1/\theta^6$ behaviour.

In order to trace back these modifications, we present in Figs. 4.19, 4.20 and 4.22 a comparison of the correct result to the predictions for the individual diagrams, that is to say we plot Eqs. (4.33a) - (4.33c). Clearly, these predicted curves confirm our expectations derived above, but deviate for angles $\theta > \max(\theta_q, \theta_\mu)$. As third line in this figures, the so-called "corrected prediction", the old prediction is multiplied by the factors $(1 - x)$, this corresponds to the forms Eqs. (4.20), (4.29) and (4.32), and multiplied by f_{kin} . The correction of this latter factor f_{kin} dramatically suppresses the radiation pattern with respect to the old prediction. Even for small angles one observes a systematic shift of the standard prediction in all figures due to the missing factor $(1 - x)^2$, which amounts to 0.9^2 in this situation. The corrected prediction agrees with the numerical result fairly well for the abelian diagrams, for the three-gluon vertex, Fig. 4.22, however a difference for large angles remains.

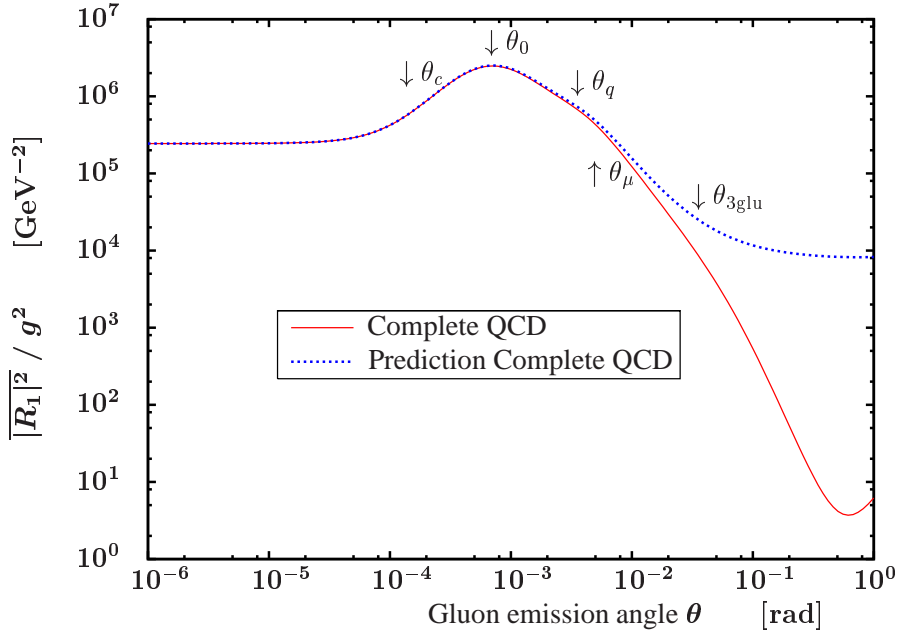


Figure 4.18: Comparison of the radiation amplitude from Fig. 4.13 including the complete set of QCD diagrams to the corresponding prediction from Eq. (4.58) multiplied by $(1 - x)$. For $\theta \sim 0.5$ the correction $f_{\text{kin}} \sim 1/\theta^4$ is not the reason for the depicted minimum. This deviation can be ascribed to the three-gluon contribution, see Figs. 4.22 and 4.23.

Whereas the radiation amplitude increases towards $\theta \approx 1$, the prediction is decreasing. This effect is even better illustrated in Figs. 4.21 and 4.23. Figs. 4.21 (a) and (b) show that our corrections so far suffice to describe the result for arbitrary emission angles. Contrary, for the three-gluon diagram we have to return to the derivation in Section 4.1. Indeed, we made the important assumption $\omega \approx xE$ when we developed Eqs. (4.30b) - (4.30d). A precise treatment using the definition of x in Eq. (4.15) together with the helpful notation

$$x' \equiv \frac{\omega}{E} = \frac{x}{\cos^2(\theta/2)} \quad (4.79)$$

at this stage yields

$$I_a = \frac{2\omega}{x} \vec{\epsilon}_\perp (2\vec{k}_\perp - x\vec{q}_\perp) = 2E \cdot \vec{\epsilon}_\perp \left(\frac{2\vec{k}_\perp}{\cos^2(\theta/2)} - x'\vec{q}_\perp \right) \quad (4.80a)$$

and

$$I_c = -2(2E - \omega) \vec{\epsilon}_\perp \vec{q}_\perp = -2E(2 - x') \vec{\epsilon}_\perp \vec{q}_\perp \quad (4.80b)$$

to give

$$\begin{aligned} I_a + I_b + I_c &= 2E \cdot \vec{\epsilon}_\perp \left(\frac{2\vec{k}_\perp}{\cos^2(\theta/2)} - x'\vec{q}_\perp - (2 - x')\vec{q}_\perp \right) \\ &= 2E \cdot 2\vec{\epsilon}_\perp \left(\frac{\vec{k}_\perp}{\cos^2(\theta/2)} - \vec{q}_\perp \right). \end{aligned} \quad (4.80c)$$

It was already pointed out, that the term I_b , Eq. (4.30c), is suppressed. Thus, the expression that we have plotted in Figs. 4.22 and 4.23 as "three-gluon corrected prediction" reads

$$M_{1,0,1}^{\text{QCD}} = f_{\text{kin}} \cdot \frac{M_{1,\text{el}}^{\text{QCD}}}{T_{A'B'}^c T_{C'D'}^c} \cdot (-2g)(1-x) \cdot [T^f, T^g]_{AB} T_{CD}^f \cdot \frac{-\vec{\epsilon}_\perp (\vec{k}_\perp / \cos^2(\theta/2) - \vec{q}_\perp)}{(\vec{k}_\perp - \vec{q}_\perp)^2 + x^2 m^2} \quad (4.81)$$

and can explain the peak structure in the contribution to the radiation amplitude.

Secondly, in the case $\theta_{3\text{glu}} < \theta_0$ we have to divide the comparison of the estimated three-gluon part

$$\frac{\vec{q}_{\text{el}\perp}^2}{(\vec{q}_{\text{el}\perp}^2 + x^2 m^2)^2} \approx \frac{\vec{q}_{\text{el}\perp}^2}{x^4 m^4}. \quad (4.82)$$

On the one side, where $\theta_q < \theta_{3\text{glu}} < \theta < \theta_0$, the abelian result is dominant, since

$$\frac{\vec{k}_\perp^2}{x^4 m^4} > \frac{\vec{q}_{\text{el}\perp}^2}{x^4 m^4} \quad (4.83)$$

is equivalent to $\theta > \theta_{3\text{glu}}$. Otherwise, the inequality changes for the angular constellation $\theta_q < \theta_{3\text{glu}} < \theta_0 < \theta$

$$\frac{1}{\vec{k}_\perp^2} \geq \frac{\vec{q}_{\text{el}\perp}^2}{x^4 m^4} \quad (4.84)$$

depending on $x\theta_c \geq \theta$. That is to say, if $x\theta_c > \theta$ no non-abelian modification takes place. Contrary, for $x\theta_c < \theta$, this argument predicts a behaviour of the radiation pattern similar to $1/\omega^4$ multiplied by f_{kin} , thus an all-over $1/(\omega^8 \theta^4)$ proportionality. In general this can be seen in Figs. 4.15 and 4.16. However the modification due to f_{kin} shadows this predictions, furthermore the dominance is only small and so interference effects give rise to the complete modification of the total result in Fig. 4.15. Figs. 4.24 - 4.28 show that the modifications which we have discussed in the light quark case, Figs. 4.17 - 4.22, also apply for the heavy quark situation.

Of course the derivation of the matrix element expressions Eqs. (4.20), (4.29) and (4.32) becomes insufficient for large values of ω . Therefore at this stage we will not continue with an analytical interpretation of these numerical results.

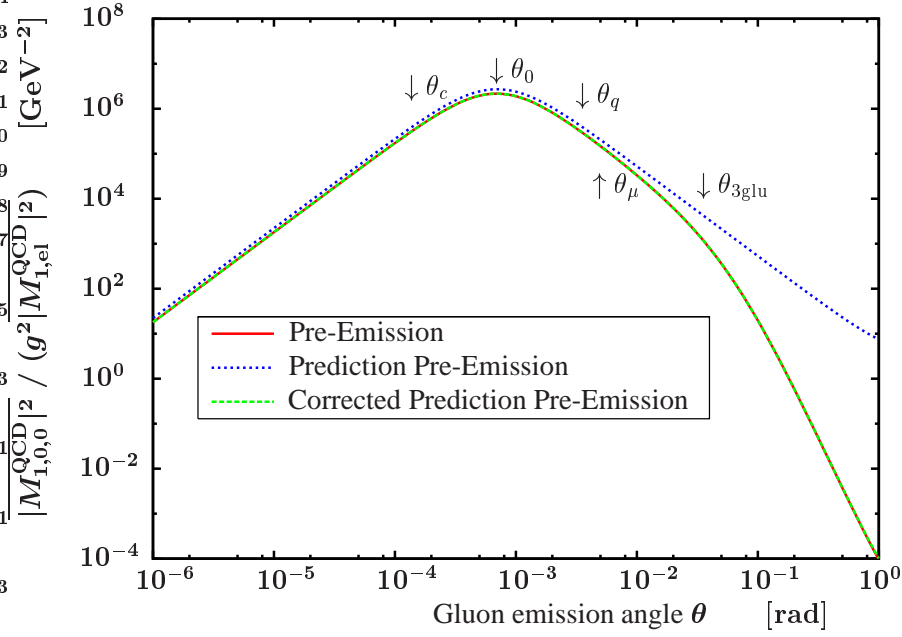


Figure 4.19: Contribution of the pre-emission diagram to the radiation amplitude in Fig. 4.13 as a function of θ compared to the prediction Eq. (4.33a) and the improved prediction which equals the expression Eq. (4.20) multiplied by f_{kin} . Taking the factors $(1-x)$ and f_{kin} obviously suffices to describe this contribution. The general pattern was discussed in the abelian section.

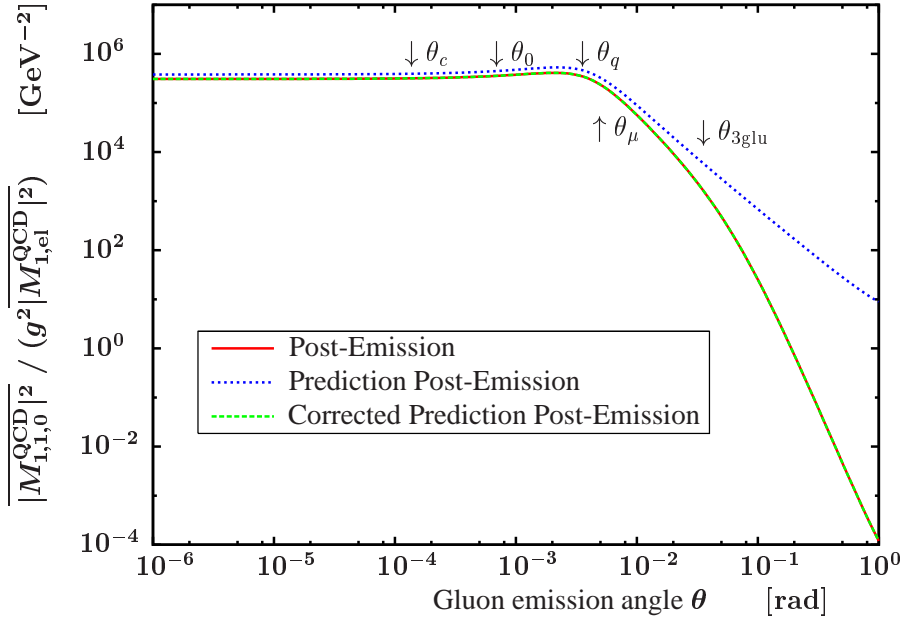
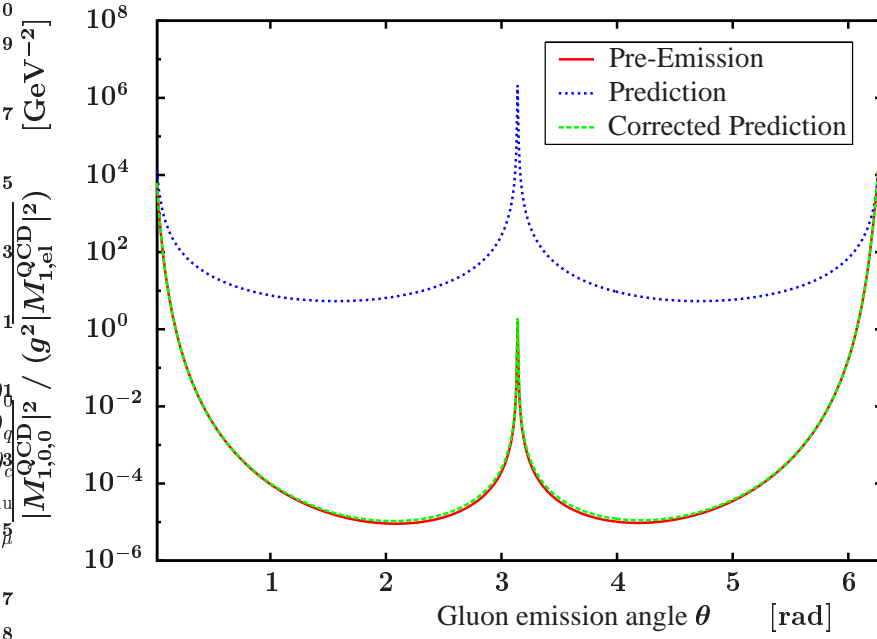
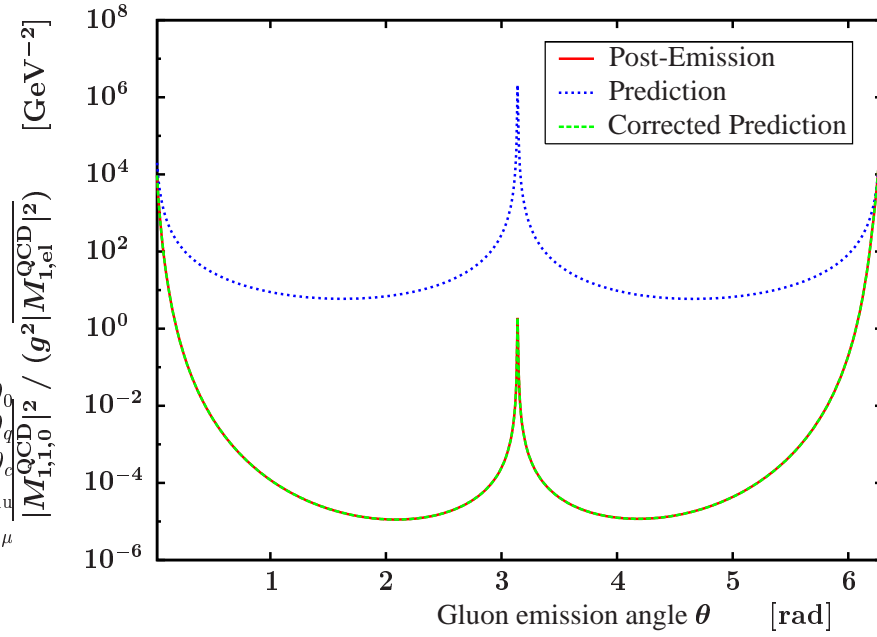


Figure 4.20: Contribution of the post-emission diagram to the radiation amplitude in Fig. 4.13 as a function of θ compared to the prediction Eq. (4.33b) and the improved prediction which equals the expression Eq. (4.29) multiplied by f_{kin} . The numerical result can be explained using $(1-x)$ and f_{kin} corrections in addition to the ordinary predictions from the paragraph on abelian QCD.



(a) Pre-projectile.



(b) Post-projectile.

Figure 4.21: Contributions of the pre-emission (a) and post-emission diagram (b) to the radiation amplitude in Fig. 4.13 as a function of θ . The figures are the same as Figs. 4.19 and 4.20 but show the behaviour for the full range $0 \leq \theta \leq 2\pi$ and demonstrate the importance of the correction factors outside the forward emission cone. A peak at $\theta = \pi$ is due to the denominators of the matrix element. Note, that for $\theta \rightarrow \pi$ also singularities in the polarization states in the A^+ -gauge arise, see Appendix C. Singularities are not drawn to infinity because the numerical calculation and the drawing program are restricted to finite values.

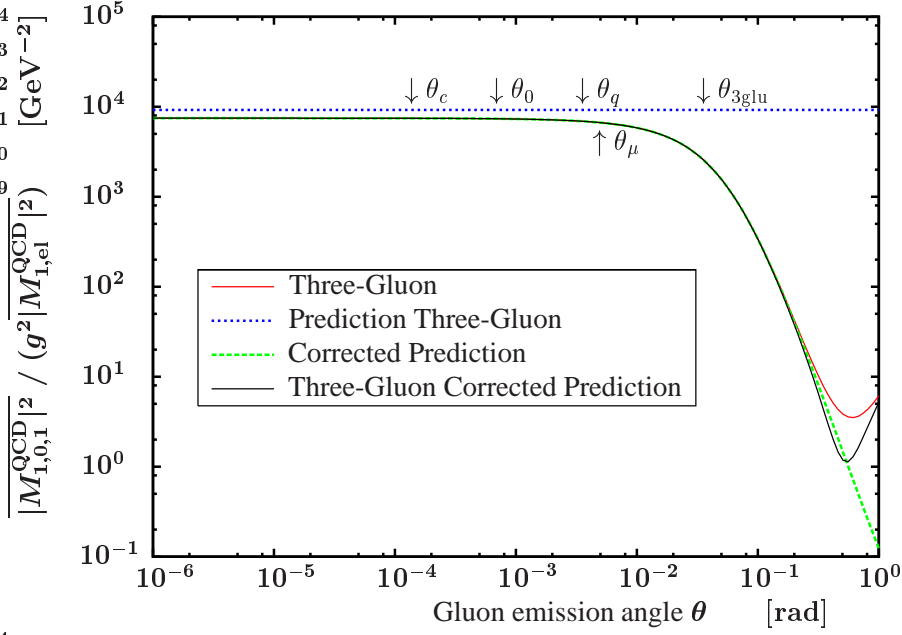


Figure 4.22: Contribution of the three-gluon diagram to the radiation amplitude in Fig. 4.13 as a function of θ compared to the prediction Eq. (4.33c) and the improved prediction which equals the expression Eq. (4.32) multiplied by f_{kin} . As in Figs. 4.19 and 4.20 the correction works well but here a minimum at $\theta \sim 0.5$ appears whereby such a pattern is not in accordance with any correction factors so far. Moreover, Eq. (4.81) instead of (4.32) is required to reproduce at least the rough pattern, see Fig. 4.23.

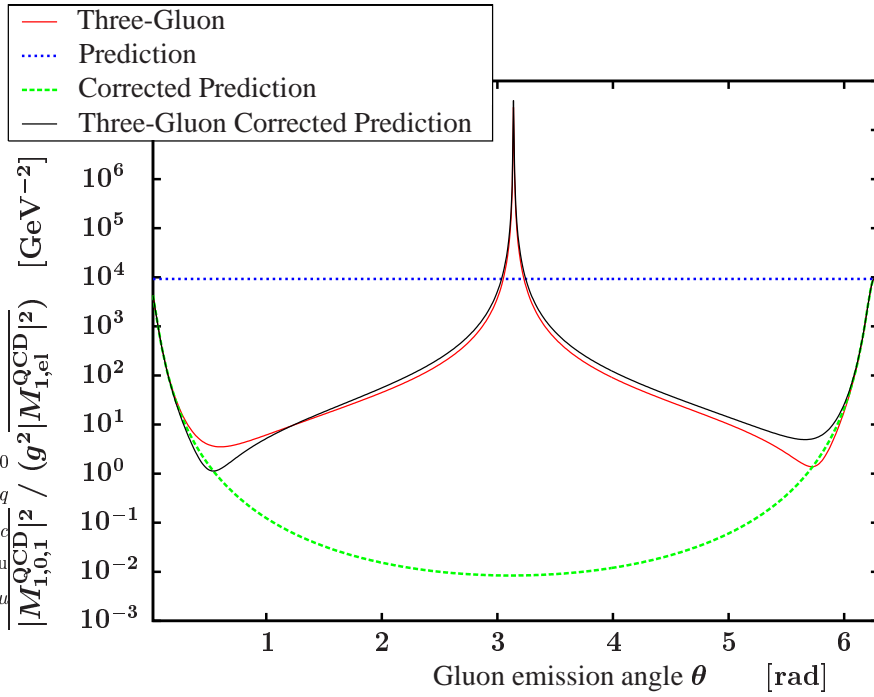


Figure 4.23: Contribution of the three-gluon diagram to the radiation amplitude in Fig. 4.13 as a function of θ . This figure is the same as in Fig. 4.22 but shown for angles $0 \leq \theta \leq 2\pi$. The peaks for $\theta \rightarrow \pi$ are due the denominators of the relevant expressions.

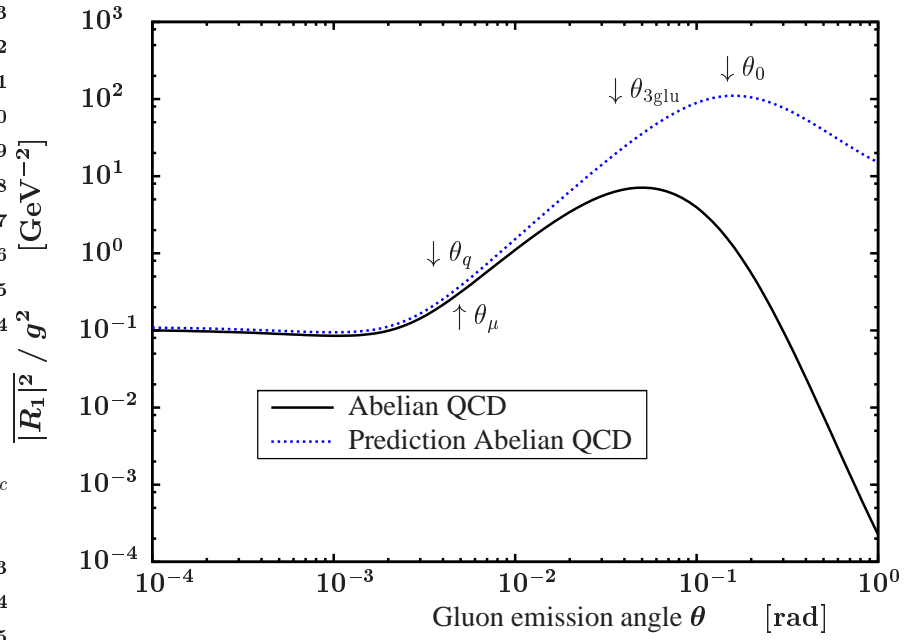


Figure 4.24: Comparison of the radiation amplitude from Fig. 4.15 in the abelian QCD approach to the corresponding prediction from Eq. (4.48).

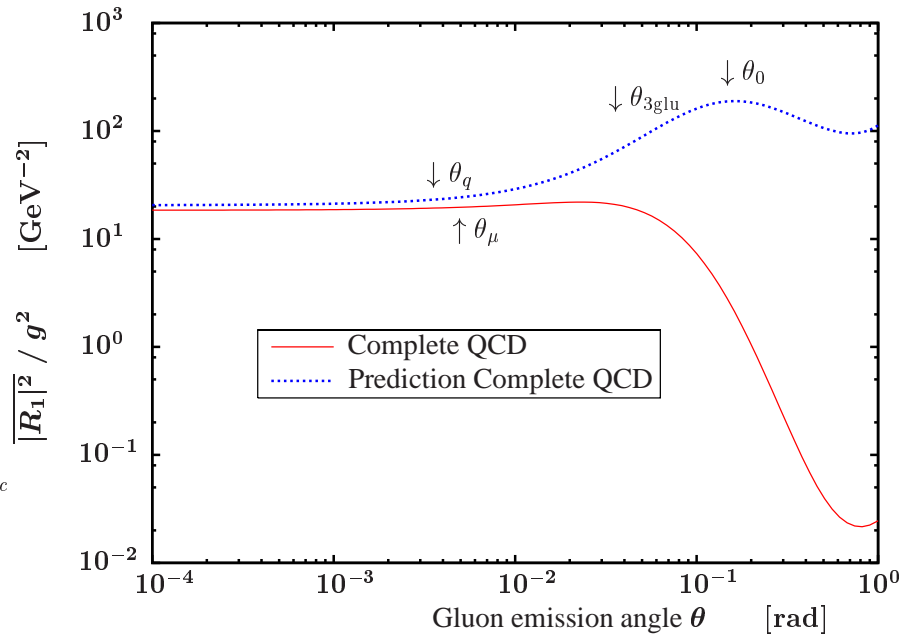


Figure 4.25: Comparison of the radiation amplitude from Fig. 4.15 including the complete set of QCD diagrams to the corresponding prediction from Eq. (4.58).

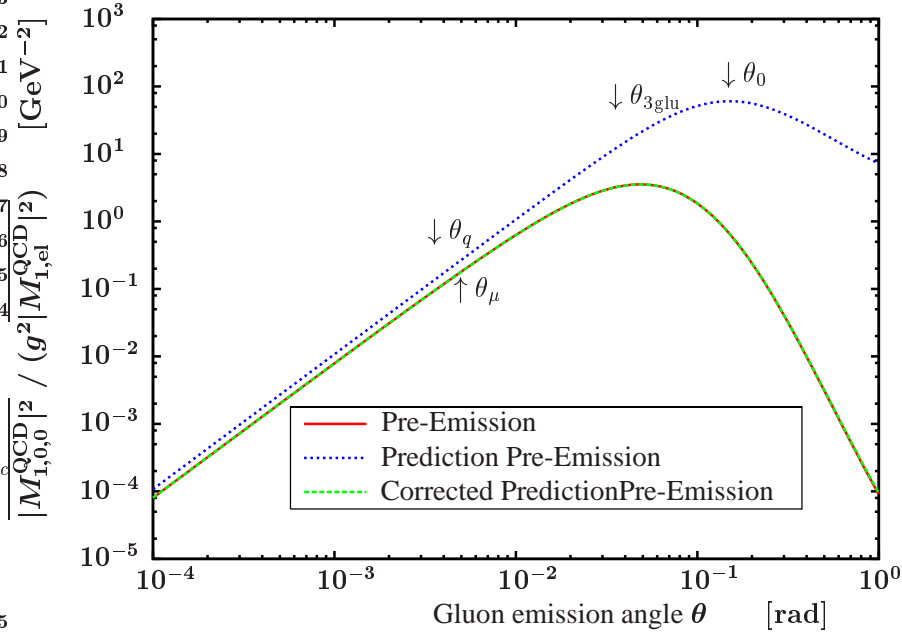


Figure 4.26: Contribution of the pre-emission diagram to the radiation amplitude in Fig. 4.15 as a function of θ compared to the prediction Eq. (4.33a) and the improved prediction which equals the expression Eq. (4.20) multiplied by f_{kin} .

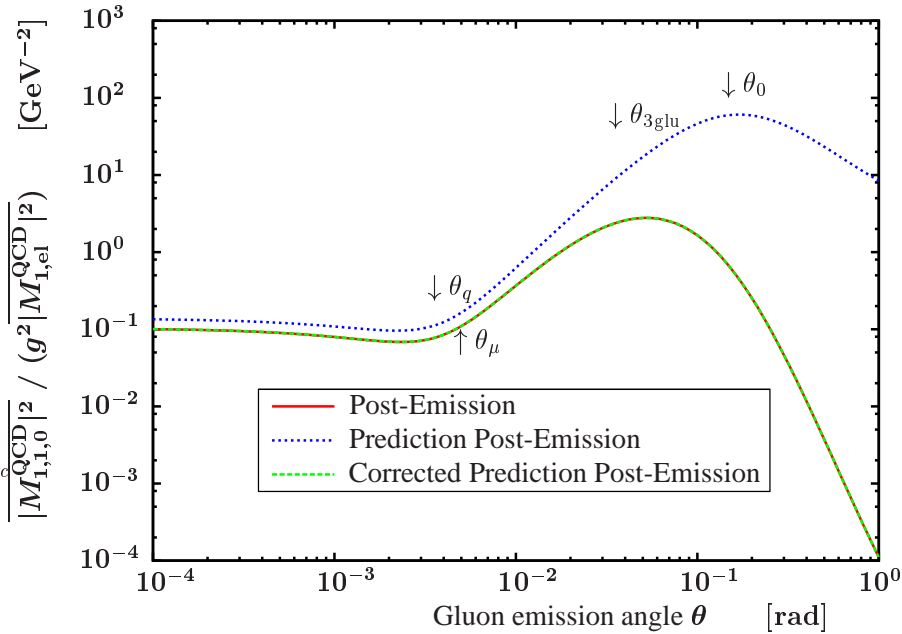


Figure 4.27: Contribution of the post-emission diagram to the radiation amplitude in Fig. 4.15 as a function of θ compared to the prediction Eq. (4.33b) and the improved prediction which equals the expression Eq. (4.29) multiplied by f_{kin} .

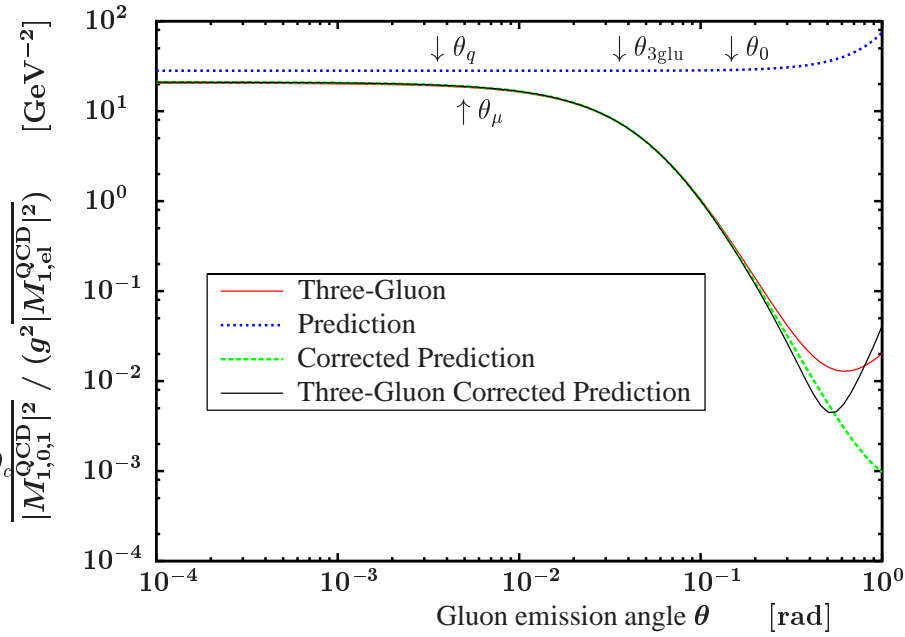


Figure 4.28: Contribution of the three-gluon diagram to the radiation amplitude in Fig. 4.15 as a function of θ compared to the prediction Eq. (4.33c) and the improved prediction which equals the expression Eq. (4.32) multiplied by f_{kin} .

4.5 Potential Model versus Quark-Quark Scattering

In the limit of soft radiation $\omega \rightarrow 0$ the physical details of the scattering processes are not relevant. We confirm this while we contrast the scattering of an incident particle in the potential model with an analogue scattering of the same projectile on a target quark at rest.

The results of a scalar QCD calculation are exhibited in Figs. 4.29 and 4.30. Four distinct situations are selected, where we consider the different combinations of heavy and light quarks in collisions. In Fig. 4.29 we choose a light projectile particle and contrast the cases of light and heavy targets. In general both pictures show no differences and have some common features which are worth noting. The behaviour of the potential calculation is similar to Fig. 4.9 where due to modified parameters of the momentum transfer the angle θ_q is shifted. The appearance of the dead cone factor in the potential model has been discussed in the last sections. We have studied that the shift of the radiation amplitude is caused by the fact that only the pre-emission contribution dominates the behaviour at the dead cone peak θ_0 and thus gives a colour factor C_F instead of C_A .

For comparison we also plot the prediction for the radiation amplitude from the dead factor

$$\overline{|R_1|^2}_{\text{GenDokKhar}} = 4g^2 C_A \frac{\vec{k}_\perp^2}{(\vec{k}_\perp^2 + x^2 m^2)^2}, \quad (4.85)$$

which comes from the combination of the pre and the post-emission diagrams, this yields a colour factor C_A , in a more generalized version than Eq. (2.1). This generalization is not restricted to small angles, a detailed explanation can be found in Appendix G. The deviation between the dead cone factor and the potential and quark-quark calculations in Fig. 4.29 equals the ratio $C_A/C_F = \frac{9}{4}$.

As technical detail we mention that contrary to our other calculations for radiation amplitudes in this case we have used a slightly different way of normalisation. Since we work with fixed

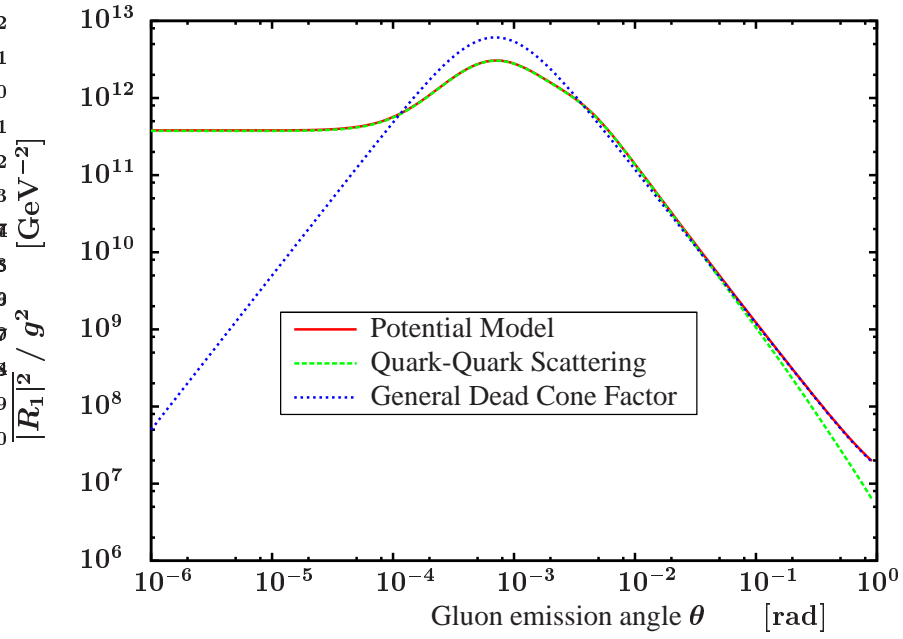
gluon momentum and input initial conditions, the remaining momenta are determined by the given transverse momentum transfer. Usually we calculate the elastic part under the assumption $\omega = 0$, this time, for Figs. 4.29-4.30, we apply the inelastic set of momenta to evaluate the elastic part. Note that this modification, the correction of the elastic part by inelastic kinematical results, becomes important when we abandon the soft radiation limit but does not effect the result for situations with $\omega = 0.001$ GeV and $p_{i,z} = 10$ GeV as being displayed in this part.

For smaller angles, as $\theta < \theta_c$ in Fig. 4.9, the dominance of the constant post-emission contribution was the reason for the constant radiation amplitude. The dead cone factor does of course not apply in this regime.

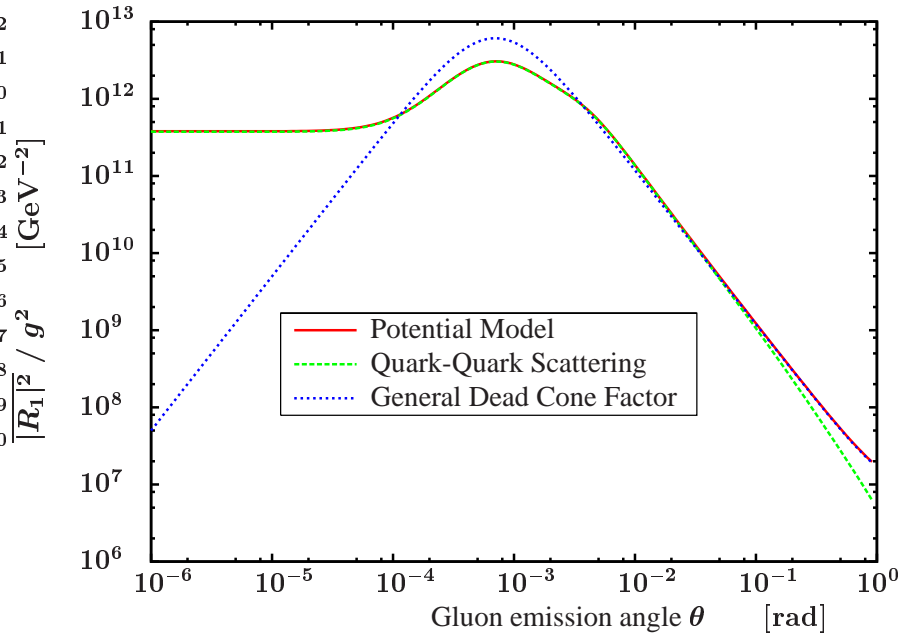
The new aspect of Fig. 4.29 is that the radiation amplitude calculated in a quark-quark collision coincides well with the potential model result as long as the angles θ are small. Thus for light projectiles, especially those which are not considerably heavier than the targets, the potential model indeed recovers the radiation amplitude obtained in a quark-quark scattering calculation. However for greater θ the radiation amplitudes from quark-quark scattering and potential model deviate.

Analogue findings for the test of the validity of the potential model can be seen in Fig. 4.30(b), where the scattering of a heavy quark on a heavy target is exhibited. As a first estimate in Fig. 4.30(a) we show that for light targets the potential model might be challenged. The assumption, that no energy would be transferred to the target, of course will be violated in such an arrangement of colliding masses.

This is intended to possibly point to the need of an improved model to describe the scattering processes in a deconfined medium in the presence of heavy projectile quarks. Strongly connected to this problem the composition of the colour-neutral matter had to be taken into account.

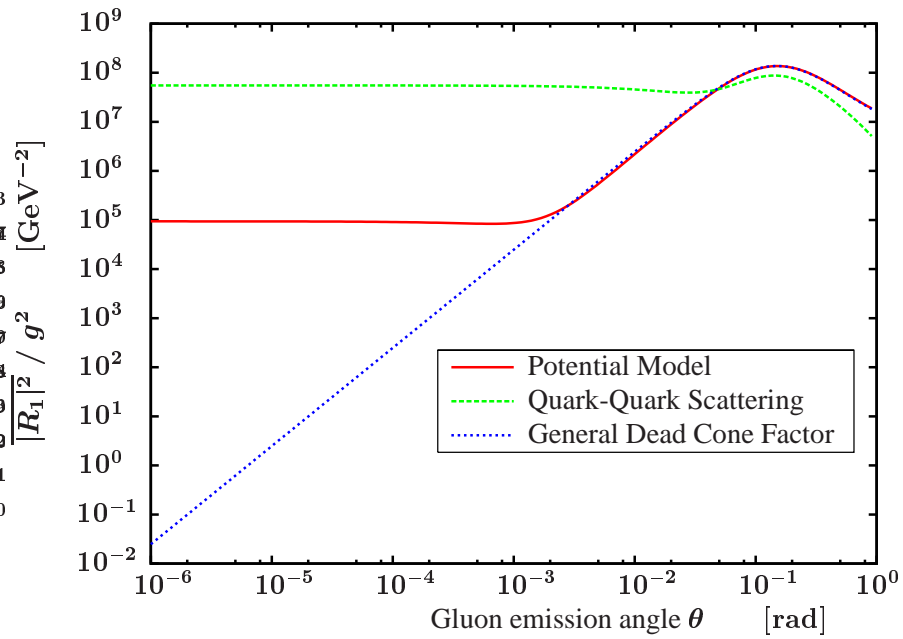


(a) Light projectile on light target.

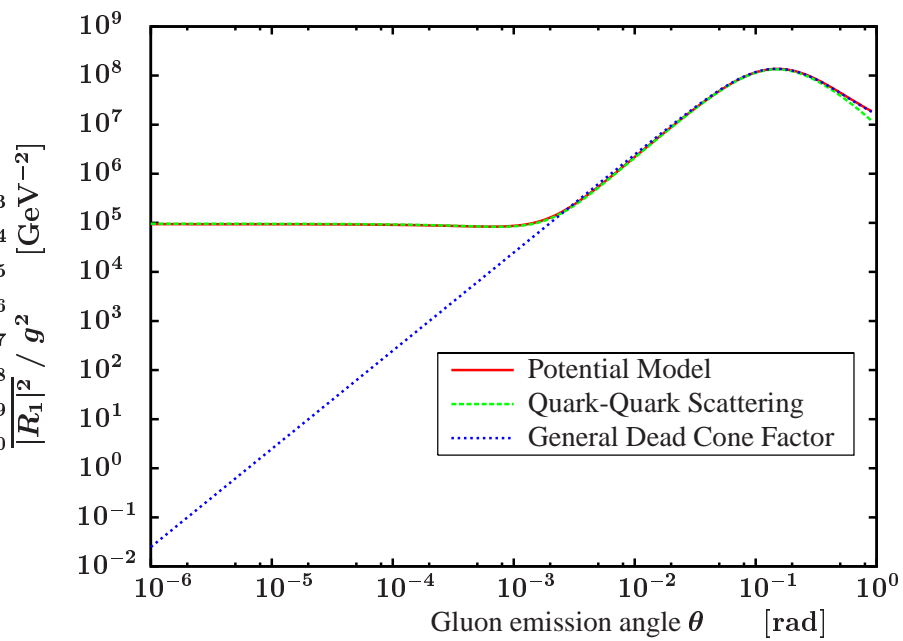


(b) Light projectile on heavy target.

Figure 4.29: The radiation amplitude $\overline{|R_1|^2}$ as a function of the emission angle θ is compared for the potential model, the quark-quark scattering on a light target and the general dead cone factor Eq. (4.85). The chosen parameters are $m_d = 0.007$ GeV (light quark), $m_c = 1.5$ GeV (heavy quark), $\vec{p}_i = (0, 0, 10)$ GeV, $\vec{p}_{i,\text{Target}} = (0, 0, 0)$, $\vec{q}_\perp = (0, 0.01)$ GeV, $\mu = 0$, $\omega = 0.001$ GeV, $\phi = 3\pi/2$.



(a) Heavy projectile on light target.



(b) Heavy projectile on heavy target.

Figure 4.30: The radiation amplitude $\overline{|R_1|^2}$ as a function of the emission angle θ is compared for the potential model, the quark-quark scattering on a heavy target and the general dead cone factor Eq. (4.85). The parameters are as in Fig. 4.29.

4.6 Summary

To summarize our findings we note that the dead cone effect consists of a suppression of radiation in forward direction by orders of magnitude. One can therefore expect that the radiative energy loss of heavy particles is substantially decreased in comparison with light particles. We have demonstrated the importance of cancellations and interference effects between contributions from different diagrams, as well as the qualitative differences between QCD and QED, that is to say charged and non-charged gauge bosons.

In Section 4.4 the question of larger ω was dealt with. For completeness it is worth noting that the numerical result for the “normalization“, the summed and averaged squared elastic matrix element $|\overline{M}|_{\text{el}}^2$ is always evaluated in the kinematical situation fixed by the same set of parameters as are used to obtain the inelastic kinematics. The reader should be aware that this is a problem for larger values of ω since it means basically to compare kinematically very distinct situations. In this case one may even question the concept of the radiation amplitude. This was already indicated in the introduction where we interpreted the radiation amplitude as conditional probability for gluon emission.

In general the inclusion of the screening mass μ suppresses the spectrum for gluon energies $\omega > \mu$. The validity of the potential model was confirmed for forward emission of radiation in the limit of small projectile masses, but estimates for heavy projectiles seem to suggest that the potential model might be reconceived.

5 Double Scattering with One-Gluon Emission

In this part we discuss the problem of double scattering in a numerical approach. A complete calculation of all relevant diagrams unfortunately failed so far. Therefore we explain the numerical problems which arise and present some key ideas. It was already shown that for multiple scattering a QCD analogue of the LPM effect exists [Gyu94, Wan95]. There only abelian diagrams were considered analytically. It turns out that especially the non-abelian diagrams might become numerically complicated for the parameter range that we have already considered in the previous chapter on single scattering.

5.1 Elastic Scattering

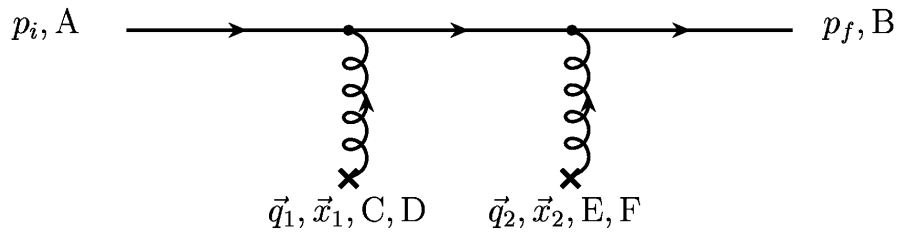


Figure 5.1: Elastic double scattering in the potential model.

The scalar matrix element for double elastic scattering in the potential model (the expression corresponds to equation (A4) in [Wan95]) reads as follows

$$M_{\text{el}}^{(2)} = (T^a T^b)_{AB} T_{CD}^a T_{EF}^b \cdot \int \frac{d^3 l}{(2\pi)^3} (-ig)(l + p_f)_\mu \cdot (-ig)g^{0\mu} \frac{e^{-i\vec{q}_2 \vec{x}_2}}{\vec{q}_2^2 + \mu^2} \cdot \frac{i}{l^2 - m^2 + i\epsilon} \cdot (-ig)(l + p_i)_\nu \cdot (-ig)g^{0\nu} \frac{e^{-i\vec{q}_1 \vec{x}_1}}{\vec{q}_1^2 + \mu^2}. \quad (5.1)$$

Here, l is the intermediate momentum of the incident particle in between the two scattering centres. Especially, $l_0 = E = p_{i0} = p_{f0}$, since energy transfer is not possible in this model. Since we consider the non-tagged case where the recoil momenta of the targets are not measured, the unknown momentum l has to be integrated over.¹

Momentum conservation at the vertices relates the internal momentum l and the momentum transfers of the scattering centres to yield

$$q_1 = l - p_i, \quad (5.2a)$$

¹Contrary in the tagged case the calculations are straightforward since all momenta are known.

$$q_2 = p_f - l. \quad (5.2b)$$

The \vec{l} -independent terms can be factored out and we obtain the expression

$$M_{\text{el}}^{(2)} = (T^a T^b)_{AB} T_{CD}^a T_{EF}^b \cdot ig^4 (2E)^2 \cdot e^{\vec{p}_i \vec{x}_1 - \vec{p}_f \vec{x}_2} \underbrace{\int \frac{d^3 l}{(2\pi)^3} \frac{e^{i\vec{l}(\vec{x}_2 - \vec{x}_1)}}{(l^2 - m^2 + i\epsilon)(\vec{q}_1^2 + \mu^2)(\vec{q}_2^2 + \mu^2)}}_{I_{\text{el}}} \quad (5.3)$$

where we will discuss only the integral I_{el} .

5.1.1 Integration in Cylindrical Coordinates

In [Wan95] one of these three integrations is performed analytically, that is to say the l_z integration is carried out with the technique of residues. We present the results in a more general way and discuss the approximations which are used in [Wan95]. In order to carry out this integration we rewrite the denominator into a product of linear factors of l_z ,

$$I_{\text{el}} = \int \frac{d^2 l_{\perp}}{(2\pi)^2} \int \frac{dl_z}{2\pi} \frac{-e^{i\vec{l}(\vec{x}_2 - \vec{x}_1)}}{(l_z - l_{z1+})(l_z - l_{z1-})(l_z - l_{z2+})(l_z - l_{z2-})(l_z - l_{z3+})(l_z - l_{z3-})}, \quad (5.4)$$

$$= - \int \frac{d^2 l_{\perp}}{(2\pi)^2} \int \frac{dl_z}{2\pi} \frac{e^{i\vec{l}(\vec{x}_2 - \vec{x}_1)}}{\prod_{k=1}^3 (l_z - l_{zk+})(l_z - l_{zk-})}. \quad (5.5)$$

Thus, the relevant residues can be found directly. The quantities $l_{zj\pm}$ indicate the zeros of the denominator with respect to l_z , where the index \pm characterizes the sign of the imaginary part

$$l_{z1\pm} = \pm \sqrt{\vec{p}_i^2 - l_{\perp}^2} \pm i\epsilon', \quad (5.6a)$$

$$l_{z2\pm} = p_{iz} \pm i\sqrt{(\vec{l}_{\perp} - \vec{p}_{i\perp})^2 + \mu^2}, \quad (5.6b)$$

$$l_{z3\pm} = p_{fz} \pm i\sqrt{(\vec{l}_{\perp} - \vec{p}_{f\perp})^2 + \mu^2}. \quad (5.6c)$$

We define the spatial distance vector of the potentials $\vec{d} = \vec{x}_2 - \vec{x}_1$ and consider the case when the component d_z is positive. Then, the integration can be carried out in the complex plane where the path is closed in the upper half. Hence, the l_z -integral follows from the sum of the residues of the integrand with positive imaginary part as

$$I_{\text{el}} = - \int \frac{d^2 l_{\perp}}{(2\pi)^2} e^{i\vec{l}_{\perp} \vec{d}_{\perp}} \cdot i \sum_{j=1}^3 \left[\frac{e^{id_z l_z} \cdot (l_z - l_{zj+})}{\prod_{k=1}^3 (l_z - l_{zk+})(l_z - l_{zk-})} \right]_{l_z=l_{zj+}}. \quad (5.7)$$

Additional in this approach, we require at least a small overall scattering taking place since the case $\vec{p}_i = \vec{p}_f$ leads to degenerated residues and the calculation had to be modified. Now, it was argued by Wang, Gyulassy and Plümer [Wan95] that the contributions from Eqs. (5.6b) and (5.6c) are suppressed by the factor $e^{-\mu d_z}$ given the assumption $d_z \gg 1/\mu$, that means if the distance of the scattering centres is much greater than the screening length of the potential. This integral can be carried out and the investigation of different residues seems to confirm the latter assumption of [Wan95]. The integration was dealt with using various summation methods, e.g. [Yak89]. However the calculation of this integral requires to cut out the singularity at $l_{\perp}^2 = \vec{p}_i^2$, thus in order to estimate the error of this integration we suggest an approach in spherical-like coordinates as explained below.

5.1.2 Integration in Spherical-like Coordinates

The aim of this co-ordinate choice is to avoid the previous co-ordinate singularity, therefore one wants to integrate over the modulus of \vec{l} where only angular integrations would remain. The integration over $|\vec{l}|$ would run from zero to infinity but should be extended to the interval $[-\infty, +\infty]$ to make the residual calculus applicable. This is done by a slight modification of standard spherical coordinates as follows. The region of space which usually is described by $\frac{\pi}{2} < \theta < \pi$ is now included by negative values of the radius, this quantity shall be denoted l .² This yields the co-ordinate definition

$$l_x = l \cos \phi \sin \theta, \quad (5.8)$$

$$l_y = l \sin \phi \sin \theta, \quad (5.9)$$

$$l_z = l \cos \theta, \quad (5.10)$$

with $-\infty < l < +\infty$, $0 \leq \phi \leq 2\pi$ and $0 \leq \theta \leq \frac{\pi}{2}$.

This coordinates will be used to evaluate the integral I_{el} defined in Eq. (5.3) in the same manner as in Section 5.1.1. The integration over l leads to the solution

$$I_{\text{el}} = -\frac{1}{(2\pi)^2} \int_0^{2\pi} d\phi \int_0^{\frac{\pi}{2}} d\theta \sin \theta \sum_{j=1}^3 \left[\frac{e^{i\vec{d}\vec{e}_l \cdot l} \cdot (l - l_{j+}) \cdot l^2}{\prod_{k=1}^3 (l - l_{k+})(l - l_{k-})} \right]_{l=l_{j+}}, \quad (5.11)$$

where

$$l_{1\pm} = \pm p \pm i\epsilon', \quad (5.12a)$$

$$l_{2\pm} = p(\vec{e}_i \vec{e}_l) \pm i\sqrt{\mu^2 + p^2[1 - (\vec{e}_i \vec{e}_l)^2]}, \quad (5.12b)$$

$$l_{3\pm} = p(\vec{e}_f \vec{e}_l) \pm i\sqrt{\mu^2 + p^2[1 - (\vec{e}_f \vec{e}_l)^2]}. \quad (5.12c)$$

Here the explicit relations in the elastic kinematics were already applied. Furthermore we have introduced the abbreviations $p = |\vec{p}_i| = |\vec{p}_f|$ and the unit vectors $\vec{e}_l = \vec{l}/l$, $\vec{e}_i = \vec{p}_i/|\vec{p}_i|$ and $\vec{e}_f = \vec{p}_f/|\vec{p}_f|$.

In this expressions no singularity occurs, assuming again $\vec{p}_i \neq \vec{p}_f$. The infinite integration we had to deal with in Section 5.1.1 is transformed into an angular integration with finite boundaries. We could show that these two approaches yield identical results whereby the precision of this comparison was restricted by the choice of cutting out the singularity for the cylindrical integration. Having developed this approach we apply the same procedure to the inelastic diagrams.

5.2 Inelastic Scattering

The diagrams for inelastic double scattering with one gluon being emitted are displayed in Figs. 5.2 and 5.3.

The notation $M_{n,m,l}$ follows the classification of the time-ordered diagrams introduced by Gyulassy, Levai and Vitev [Gyu00a]. The label n counts the number of scatterings, $0 \leq m \leq n$ denotes that the gluon is emitted after the m -th scattering, especially $m = 0$ means the emission takes place before the first scattering, and l labels the different possible final state interaction patterns after the

²This should not be confused with l as four-momentum, since we deal only with three-dimensional integrations.

gluon is emitted. This number l can even be organized to represent the interaction pattern in a binary array

$$\vec{\sigma} = (\sigma_1 = 0, \dots, \sigma_m = 0, \sigma_{m+1}, \dots, \sigma_n), \quad (5.13)$$

where all scattering variables σ_i up to the emission process are zero, $\sigma_i = 0$ for $1 \leq i \leq m$. For $m < i$ the binary numbers σ_i are 1 if the gluon rescatters at centre i otherwise 0 for a scattering of the quark. Therefore the label $l = \left(\sum_{j=1}^n \sigma_j 2^j \right) / 2^{m+1}$ numbers the diagrams for fixed n and l in a unique manner.

It might be instructive to consider for example $M_{2,1,1}$, Fig. 5.3(d). The number of scatterings is $n = 2$, the emission takes place after the first scattering centre is passed, $m = 1$, the allocated binary array $\vec{\sigma} = (0, 1)$ gives $l = 1$. In contrast $M_{2,1,0}$, Fig. 5.2(b), without gluon rescattering gives $\vec{\sigma} = (0, 0)$ and $l = 0$.

We can now also count the total number of possible diagrams with one gluon emission for a given number of scattering centres n . For fixed m there exist $l_{\max} + 1$ arrangements, with l_{\max} realized for $\sigma_{0,\dots,m} = 0$ and $\sigma_{m+1,\dots,n} = 1$ one finds

$$l_{\max} = \frac{1}{2^{m+1}} \sum_{j=m+1}^n 2^j = 2^{n-m} - 1 \quad (5.14)$$

and

$$\sum_{m=0}^n (l_{\max} + 1) = \sum_{m=0}^n 2^{n-m} = 2^{n+1} - 1 \quad (5.15)$$

as the combinatorial number of all diagrams where one gluon is being emitted and n scatterings occur. Note, this information can be derived directly from the binary array, since the number of possible arrangements of the two "states" 0 and 1 in a field of fixed length n corresponds to the number of possible diagrams. The number 2^n of these combinations has to be doubled to account for emissions prior to the first scattering, one may assume an imaginary zeroth centre with σ_0 , and the total number must be reduced by 1 since the purely elastic diagram, all $\sigma_{0,\dots,n} = 0$, has to be excluded. Again we find that the number of relevant radiation diagrams grows with the number of scatterings n as $2^{n+1} - 1$. In the case $n = 1$ these are the 3 diagrams Figs. 4.2, 4.3 and 4.4, for $n = 2$ there are 7 diagrams, Figs. 5.2 and 5.3, for $n = 3$ one already has to compute 15 diagrams.

In order to evaluate the diagrams in Figs. 5.2 and 5.3 again integrals over the unknown internal momentum have to be performed, where we have applied the same approach which was introduced in the section on the elastic case above. The calculation of all the relevant residues is a straightforward even though extensive task. Comparisons of both integration methods, which are the cylindrical and the spherical-like coordinates, and different summation schemes reveal considerable problems for the diagrams $M_{2,0,2}$ (Fig. 5.3(c)), $M_{2,0,3}$ (Fig. 5.3(b)) and $M_{2,1,0}$ (Fig. 5.2(b)). This makes complete numerical calculations for the moment being impossible, even a pure abelian discussion is not possible due to the complications with integrations in $M_{2,1,0}$. Two main reasons can account for the deviations between the different integration approaches. At first the cutting of the integration interval to avoid singularities becomes impossible in some cases. This is to say there are singularities which fall in the range where the integrand has its dominant contributions. Secondly, the numerical subtraction of large numbers might be a further restriction to the increase of precision. Therefore the numerical analysis of these diagrams and the integration in general should be under deeper investigation. The application of additional program packages for the integration of singular functions, e.g. [Wed00], could be useful.

A full understanding of these integrations is especially necessary to check assumptions that were made in [Wan95] to derive the LPM analogue in QCD. We emphasize that in their work the actual full integration is avoided in the way that one factorises out the radiation part of the integrand after the l_z integration assuming it would not depend on \vec{l}_\perp . A continuation of the double scattering calculations could provide a valuable check of this approximation.

6 Summary and Outlook

In the present thesis we have investigated how the mass parameter of an on-shell quark passing a deconfined medium influences its radiative energy loss probability.

The importance of the basic single scattering diagrams with one gluon emission is emphasized by various aspects. Among of them data from RHIC, which suggest thin plasmas, imply that only a few scatterings are taking place. The existence of an analogue to the LPM effect in QCD, which would reduce the effective number of scatterings further, is another indication of the significance of these diagrams. Moreover the fast convergence of the opacity expansion, where the first order in the GLV formalism describes the radiative energy loss considerably well in this approach, suggests the relevance of the single scattering processes. Therefore a very detailed discussion of these diagrams was done in the potential model by numerical means.

We have shown and discussed the exciting features of the radiation amplitude in QED and QCD and disentangled interference effects and especially the influence of the non-abelian diagram in QCD.

The dead cone suppression factor was shown to emerge in specific angular regions, however the radiation amplitude deviates from this prediction for either small angles, due to the post-emission process, or in case of higher gluon energies ω . For the latter possibility the three-gluon diagram, including the three-gluon vertex, becomes responsible. In summary we have confirmed the suppression effect due to the heavy quark mass, but the dead cone factor is not the correct modification to light quark scenarios in all kinematical situations.

We have explicitly shown that not the mass parameter of the projectile itself but the ratio to the transverse momentum transfer is relevant to categorise light and heavy mass situations. As stated above for large gluon energies, that is to say greater than the transverse momentum transfer, the non-abelian effects become important.

In literature various approaches assume soft radiation $\omega \rightarrow 0$, small momentum transfers $\vec{q} \rightarrow 0$ and light particles $m \rightarrow 0$. With this investigation we give a detailed insight into the interplay of these assumptions in the potential model approach. Besides this we have confirmed that the A^+ -gauge is appropriate to neglect radiation contributions from target lines. Also comparisons of scalar and spinor calculations did not reveal significant differences.

We have indicated that the potential model might be challenged if heavy projectile quarks are present. In addition, it was emphasized that for considerably large values of the gluon energy one is confronted with factorisation problems with respect to the elastic scattering part in matrix elements. In such situations the missing unique interpretation of the radiation amplitude questions whether it is sufficient to consider ratios of inelastic and elastic cross sections.

One should be aware that the integration of the radiation pattern in order to obtain the total energy loss might smooth out the distinct scenarios we have elucidated. The problem of integration using numerical results for the radiation amplitude can be a challenging subject of further research.

The evaluation of all double scattering diagrams to satisfactory precision, which failed so far, should be analysed further in order to discuss the QCD analogue of the LPM effect numerically. It is

worth noting that these situations already require considerably more calculation power and for further generality, e.g. higher scattering processes or integrations to obtain the net energy loss, maybe even with spinors instead of scalar particles, analytical simplifications seem to be unavoidable.

Various other aspects could be implemented, at first the TM effect via a finite gluon mass or the interference with the production amplitude of the quark to make contact to the GLV formalism. Having done an integration to yield an energy loss one could consider further contributions of higher orders, as e.g. diagrams with two gluons being emitted. The enlarged variety of parameters might dramatically enlarge the number of kinematical regions which had to be considered analytically. The level of tree diagrams considered here does of course not take into account the dynamical effect of QCD. Therefore the inclusion of radiative corrections, that means the calculation of loop diagrams could be a further topic of investigation. A further step might be the test of predictions for hadronic observables with respect to our findings, that is to say a convolution of the numerically found radiation amplitude with appropriate fragmentation functions. Finally these results could be implemented into a model of detailed balance to account for absorption and stimulated emission effects of gluons.

In closing the main result is that various equations from literature are checked numerically, and also analytically, where especially the dead cone factor was found to be correct but not sufficient in all kinematical configurations. How this shortcoming would effect the net energy loss still remains an open question to be clarified by further detailed investigations.

Appendix A Remarks on Colour Algebra

In general the algebra of the group $SU(N)$ is defined by the commutation relation

$$[T^a, T^b] = if_{abc}T^c \qquad a, b, c = 1 \dots N^2 - 1, \qquad (\text{A.1})$$

where T^a are the generators of the group, f_{abc} denote the structure constants and a, b, c, \dots stand for the colour indices. For $SU(3)$, the colour group which is used in the program code, the conventional colour matrices are, e.g. [Hua92],

$$\begin{aligned} \lambda_1 &= \begin{pmatrix} 0 & 1 & 0 \\ 1 & 0 & 0 \\ 0 & 0 & 0 \end{pmatrix}, & \lambda_2 &= \begin{pmatrix} 0 & -i & 0 \\ i & 0 & 0 \\ 0 & 0 & 0 \end{pmatrix}, & \lambda_3 &= \begin{pmatrix} 1 & 0 & 0 \\ 0 & -1 & 0 \\ 0 & 0 & 0 \end{pmatrix}, \\ \lambda_4 &= \begin{pmatrix} 0 & 0 & 1 \\ 0 & 0 & 0 \\ 1 & 0 & 0 \end{pmatrix}, & \lambda_5 &= \begin{pmatrix} 0 & 0 & -i \\ 0 & 0 & 0 \\ i & 0 & 0 \end{pmatrix}, & \lambda_6 &= \begin{pmatrix} 0 & 0 & 0 \\ 0 & 0 & 1 \\ 0 & 1 & 0 \end{pmatrix}, \\ \lambda_7 &= \begin{pmatrix} 0 & 0 & 0 \\ 0 & 0 & -i \\ 0 & i & 0 \end{pmatrix}, & \lambda_8 &= \frac{1}{\sqrt{3}} \begin{pmatrix} 1 & 0 & 0 \\ 0 & 1 & 0 \\ 0 & 0 & -2 \end{pmatrix}, \end{aligned} \qquad (\text{A.2})$$

whereby these matrices are related to the matrix representation of the generators via

$$T^a = \frac{\lambda_a}{2}. \qquad (\text{A.3})$$

Very important features are, that the colour matrices are hermitian

$$T^{a\dagger} = T^a, \qquad (\text{A.4a})$$

and traceless

$$Tr T^a = 0. \qquad (\text{A.4b})$$

The colour parts of the matrix elements can however be evaluated analytically. Therefore some useful relations should be given. The generators are normalized by

$$Tr [T^a T^b] = \frac{1}{2} \delta^{ab}. \qquad (\text{A.5})$$

From the very useful equation

$$T_{ij}^a T_{kl}^a = \frac{1}{2} \left(\delta_{il} \delta_{jk} - \frac{1}{N} \delta_{ij} \delta_{kl} \right), \quad (\text{A.6})$$

one especially obtains

$$(T^a T^a)_{il} = \frac{1}{2} \left(\delta_{il} N - \frac{1}{N} \delta_{il} \right) = C_F \delta_{il}, \quad (\text{A.7})$$

where the Casimir of the representation of the group is

$$C_F = \frac{N^2 - 1}{2N}. \quad (\text{A.8})$$

We further need the relation

$$\sum_{c,d=1}^{N^2-1} f_{acd} f_{bcd} = \delta_{ab} C_A, \quad (\text{A.9})$$

which defines the Casimir of the adjoint representation $C_A = N$. In particular, for $SU(3)$ we obtain $C_F = \frac{4}{3}$ and $C_A = 3$.

In every matrix element a colour structure, that is to say an arrangement consisting of colour matrices and structure constants is enclosed between colour states χ_X . Thus, the abbreviation

$$(C_{b_1 \dots b_n}^{a_1 \dots a_m})_{AB} \equiv \chi_B^\dagger C_{b_1 \dots b_n}^{a_1 \dots a_m} \chi_A \quad (\text{A.10})$$

is used, as also in [Wan95], with arbitrary numbers m and n of colour indices. There are N independent colour states which we denote by capital letters as subscript $A, B, C = 1 \dots N$. In the terminology of matrices, these colour states are represented by N -dimensional unit vectors, thus for $SU(3)$ they read

$$\chi_1 = \begin{pmatrix} 1 \\ 0 \\ 0 \end{pmatrix}, \quad \chi_2 = \begin{pmatrix} 0 \\ 1 \\ 0 \end{pmatrix} \quad \text{and} \quad \chi_3 = \begin{pmatrix} 0 \\ 0 \\ 1 \end{pmatrix}. \quad (\text{A.11})$$

The overline at a colour expression means an average over all initial colours and a sum over all final colour states, under the modulus squared the product with the adjoint matrix structure is understood,

$$\overline{|C_{A_1 \dots A_s, A'_1 \dots A'_t}^{g_1 \dots g_m, g'_1 \dots g'_n}|^2} = \frac{1}{(N^2 - 1)^m \cdot N^s} \sum_{\substack{A_1, \dots, A_s = 1 \dots N, \\ A'_1, \dots, A'_t = 1 \dots N, \\ g_1, \dots, g_m = 1 \dots (N^2 - 1), \\ g'_1, \dots, g'_n = 1 \dots (N^2 - 1)}} \left(C_{A_1 \dots A_s, A'_1 \dots A'_t}^{g_1 \dots g_m, g'_1 \dots g'_n} \cdot (C_{A_1 \dots A_s, A'_1 \dots A'_t}^{g_1 \dots g_m, g'_1 \dots g'_n})^\dagger \right), \quad (\text{A.12})$$

where m initial gluons, s initial quarks, n final gluons and t final quarks are assumed.

As clarification it should be demonstrated, how the important colour parts Eqs. (4.53) and (4.55) are obtained. The colour structure of the elastic single scattering Figs. 4.1 or D.1, which serves as precondition, is evaluated first. Note, due to the sum rule, all equal indices have to be summed over.

Thus, we do not write the sum sign for f and we will later also neglect the sum signs for the colour states. The quantity $C_{1,\text{el}}$ in Eq. (3.27) reads

$$\begin{aligned}
C_{1,\text{el}} &= \overline{|T_{AB}^f T_{CD}^f|^2} \\
&= \frac{1}{N^2} \sum_{A,B,C,D=1}^N (\chi_B^\dagger T^f \chi_A \chi_D^\dagger T^f \chi_C) \cdot (\chi_B^\dagger T^g \chi_A \chi_D^\dagger T^g \chi_C)^\dagger \\
&= \frac{1}{N^2} (\chi_B^\dagger T^f \chi_A \chi_D^\dagger T^f \chi_C) \cdot (\chi_B^\dagger T^g \chi_A \chi_D^\dagger T^g \chi_C)^\dagger \\
&= \frac{1}{N^2} (\chi_B^\dagger T^f \chi_A \chi_D^\dagger T^f \chi_C \chi_C^\dagger T^g \chi_D \chi_A^\dagger T^g \chi_B) \\
&= \frac{1}{N^2} \text{Tr}(T^f T^g) \text{Tr}(T^f T^g) \\
&= \frac{1}{2N^2} \delta^{fg} \text{Tr}(T^f T^g) \\
&= \frac{C_F}{2N}.
\end{aligned} \tag{A.13}$$

Within this derivation, we have used Eq. (A.7) but with the sum convention, Eq. (A.4a), cyclical exchange in the trace of a matrix product and the matrix relations

$$\sum_{A=1}^N \chi_A \chi_A^\dagger = \mathbb{E} \quad \text{and} \quad \sum_{A=1}^N \chi_A^\dagger \mathbb{M} \chi_A = \text{Tr}(\mathbb{M}), \tag{A.14}$$

with \mathbb{E} as identity matrix and \mathbb{M} as arbitrary matrix, each of them has the format $(N \times N)$. Now, the colour element Eq. (4.55) can be evaluated where it is convenient to find the elastic colour part $C_{1,\text{el}}$,

$$\begin{aligned}
\overline{|(T^f T^g)_{AB} T_{CD}^f|^2} &= \frac{1}{N^2} \chi_B^\dagger T^f T^g \chi_A \chi_D^\dagger T^f \chi_C \chi_C^\dagger T^e \chi_D \chi_A^\dagger T^g T^e \chi_B \\
&= \frac{1}{N^2} \text{Tr}(T^f T^g T^g T^e) \text{Tr}(T^f T^e) \\
&= C_F \cdot \frac{1}{N^2} \text{Tr}(T^f T^e) \text{Tr}(T^f T^e) \\
&= C_F \cdot C_{1,\text{el}}.
\end{aligned} \tag{A.15}$$

This is similarly carried out for Eq. (4.53), the colour commutator structure, that is also denoted by $[T^f, T^g]_{AB} T_{CD}^f = -C_{CD,AB}^g$, (cf. Eq. (7) in [Wan95]),

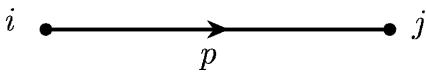
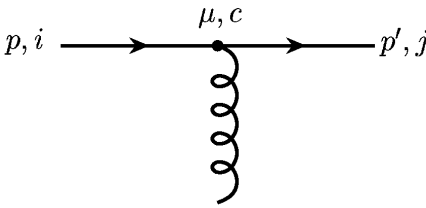
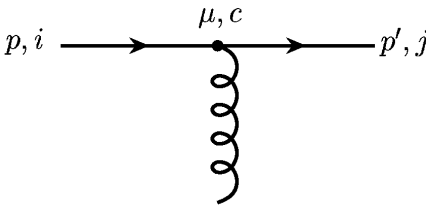
$$\begin{aligned}
\overline{|[T^f, T^g]_{AB} T_{CD}^f|^2} &= \overline{|f_{fge} T_{AB}^e T_{CD}^f|^2} \\
&= \frac{1}{N^2} f_{fge} f_{bga} \chi_B^\dagger T^e \chi_A \chi_D^\dagger T^f \chi_C \chi_C^\dagger T^b \chi_D \chi_A^\dagger T^a \chi_B \\
&= \frac{1}{N^2} f_{fge} f_{bga} \text{Tr}(T^e T^a) \text{Tr}(T^f T^b) \\
&= \frac{1}{N^2} f_{fge} f_{bga} \frac{1}{2} \delta_{ea} \text{Tr}(T^f T^b) \\
&= \frac{1}{2N^2} f_{fge} f_{bge} \text{Tr}(T^f T^b) \\
&= C_A \cdot \frac{1}{2N^2} \delta_{fb} \text{Tr}(T^f T^b) \\
&= C_A \cdot C_{1,\text{el}}.
\end{aligned} \tag{A.16}$$

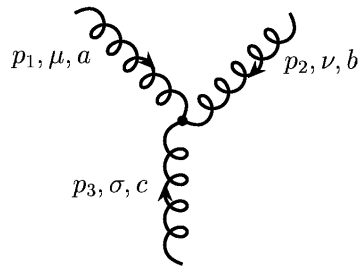
Appendix B Feynman Rules

The following conventions for the Feynman rules are applied throughout this work. We also display the naming scheme used in our C++ code for the colourless parts, colour factors are shown in curly brackets, refer also to Appendix E. The different rules for scalar and spinor QCD are distinguished. The corresponding expressions for QED are recovered if all colour generators are set to unity and the colour structure constants become zero, which means that photon self coupling does not occur due to the $U(1)$ symmetry.

In the case of fermionic particles incoming spinor lines obtain a factor $u(p, s) \cdot \chi_A$, outgoing spinor lines a factor $\bar{u}(p, s) \cdot \chi_A^\dagger$, for antiparticles there should be v instead of u . The bispinor $u(p, s)$ is given in Appendix E. A factor ϵ^μ is assigned to outer gluon or photon lines. For scalar particles the relevant factors reduce to the colour parts χ_A or χ_A^\dagger , respectively. The colour factors χ_A, T^c, T_{AB}^c and f_{abc} are explained in Appendix A.

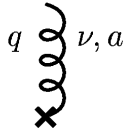
The delta functions which ensure momentum conservation at the vertices are neglected.

	<p>ScalarPropagator(ContraVector * p, double * m₀)</p> $\frac{i}{p^2 - m_0^2 + i\epsilon} \cdot \{\delta_{ij}\}$
	<p>SpinorPropagator(ContraVector * p, double * m₀)</p> $\frac{i}{p^\mu \gamma_\mu - m_0 + i\epsilon} \cdot \{\delta_{ij}\}$
	<p>ScalarVertex(ContraVector * p', ContraVector * p, int & mu)</p> $-ig(p + p')_\mu \cdot \{T_{ji}^c\}$
	<p>SpinorVertex(int & mu)</p> $-ig\gamma_\mu \cdot \{T_{ji}^c\}$
	<p>GluonPropagator(ContraVector * k, int & mu, int & nu)</p> $\frac{-i}{k^2 + i\epsilon} \left(g^{\mu\nu} - (1 - \lambda) \cdot \frac{k^\mu k^\nu}{k^2 + i\epsilon} \right) \cdot \{\delta_{ab}\}$
<p>$\lambda \rightarrow 1$: Feynman gauge, $\lambda \rightarrow 0$: Landau gauge</p>	



ThreeGluonVertex(ContraVector * p_1 , int & μ ,
ContraVector * p_2 , int & ν , ContraVector * p_3 , int & σ)

$$ig[(p_1 - p_2)_\sigma \cdot g_{\mu\nu} + (p_2 - p_3)_\mu \cdot g_{\nu\sigma} + (p_3 - p_1)_\nu \cdot g_{\sigma\mu}] \cdot \{if_{abc}\}$$



StaticDebyeScreenedPotential(ContraVector * q , int & ν)

$$-ig \cdot g^{0\nu} \frac{e^{-i\vec{q}\cdot\vec{x}}}{\vec{q}^2 + \mu^2} \cdot \{T_{CD}^a\}$$

μ . . . Debye screening mass

Appendix C Gauge Invariance

C.1 General Restrictions

The canonical quantisation of the field strength A^μ ,

$$A^\mu = N\epsilon^\mu e^{-ikx}, \quad (\text{C.1})$$

starts from an expansion in Minkowski space. Hence, there are 4 polarization vectors required, which serve as a basis. We consider massless photons with momentum k , $k^2 = 0$, N is a normalization constant. The same holds true for gluons when we neglect colours. For brevity, we speak about photons.

The free photon field A^μ obeys the wave equation

$$\square A^\mu = 0 \quad (\text{C.2})$$

in Lorentz gauge $\partial_\mu A^\mu = 0$. This implies the four-dimensional transverse condition $\epsilon k = 0$. However there are only 2 transverse polarizations realised for real photons. In the quantisation formalism, the method of Gupta and Bleuler, which is based on the Lorentz condition $\partial_\mu A^\mu = 0$, shows that the contributions of scalar and longitudinal photons to expectation values cancel each other. Note, that in the case of QCD the formal introduction of ghost fields is required to cancel internal contributions from non-transverse gluons.

In the following section we discuss the question, how polarization vectors are to be chosen especially for the numerical calculation. The connection to the A^+ -gauge, which is often applied, e.g. in articles on energy loss by gluon radiation [Gun82, Wan95], is demonstrated.

The solution A^μ of Eq. (C.2) is not fixed by the Lorentz condition. Any solution

$$A'^\mu = A^\mu - \partial^\mu \Lambda \quad (\text{C.3})$$

with $\square \Lambda = 0$ satisfies the relevant equations. If we choose $\Lambda \sim e^{-ikx}$, this allows for a modification of the polarization vectors according to

$$\epsilon'^\mu = \epsilon^\mu + \beta k^\mu, \quad (\text{C.4})$$

where β is an arbitrary constant.

The four-dimensional polarization vectors for free photons are usually constructed from an intuitive generalisation of the three-dimensional orthonormal polarization vectors which are perpendicular to \vec{k} . This three dimensional transverse gauge with $A^0 = 0$ corresponds to the Coulomb gauge. However, this relation is constrained to the form of polarization vectors, and the Coulomb gauge, defined by $\vec{\nabla} \cdot \vec{A} = 0$, allows $A^0 = 0$ only if no charges are present. Thus, we restrict the terminology to the notation A^0 -gauge as a particular choice from the class of Lorentz gauges. It reads

$$\epsilon^{(1)} = (0, \vec{\epsilon}^{(1)}), \quad (\text{C.5})$$

$$\epsilon^{(2)} = (0, \vec{\epsilon}^{(2)}), \quad (\text{C.6})$$

$$\vec{\epsilon}^{(1)} \cdot \vec{\epsilon}^{(2)} = \vec{\epsilon}^{(1)} \cdot \vec{k} = \vec{\epsilon}^{(2)} \cdot \vec{k} = 0, \quad (\text{C.7})$$

$$\vec{\epsilon}^{(1)} \cdot \vec{\epsilon}^{(1)} = \vec{\epsilon}^{(2)} \cdot \vec{\epsilon}^{(2)} = 1. \quad (\text{C.8})$$

In general the polarization vectors have to obey the following conditions

$$\epsilon^{(1)} k = \epsilon^{(2)} k = \epsilon^{(1)} \epsilon^{(2)} = 0, \quad (\text{C.9})$$

$$\epsilon^{(1)} \epsilon^{(1)} = \epsilon^{(2)} \epsilon^{(2)} = -1. \quad (\text{C.10})$$

It is straightforward to show that these conditions are invariant with respect to the transformation Eq. (C.4).

C.2 Tests of Gauge Invariance

C.2.1 Gauge Invariance for Polarization Vectors

$A^0 = 0$ gauge

The z-direction is generally fixed by the direction of the incoming projectile quark. The momentum of the emitted gluon is expressed in spherical coordinates, the form of the three-dimensional transverse polarizations can be obtained if one starts from a gluon momentum in z-direction, where polarizations are in x- and y-direction, respectively. The general situation for an arbitrary momentum direction is then obtained by application of rotation matrices. For completeness we note the expressions which are especially employed in the program code in the function "getPolarization_Azero(...)",

$$k = \omega \cdot (1, \cos \phi \sin \theta, \sin \phi \sin \theta, \cos \theta), \quad (\text{C.11})$$

$$\epsilon^{(1)} = (0, \cos \phi \cos \theta, \sin \phi \cos \theta, -\sin \theta), \quad (\text{C.12})$$

$$\epsilon^{(2)} = (0, -\sin \phi, \cos \phi, 0). \quad (\text{C.13})$$

The emission angle θ is related to the gluon rapidity y , sometimes denoted η , via the ratio of the plus and minus momentum components $k^+ = k_0 + k_3$ and $k^- = k_0 - k_3$,

$$y = \frac{1}{2} \ln \frac{k^+}{k^-} = \ln \frac{1 + \cos \theta}{\sin \theta}, \quad (\text{C.14})$$

The central rapidity region $y \sim 0$ corresponds to transverse gluon emission.

$A^+ = 0$ gauge

In light-cone coordinates the remaining freedom of the potential A^μ is fixed with the condition $A^+ = 0$. In terms of the usual coordinates this refers to the form

$$\epsilon^{(1/2)} = (\epsilon_0, \vec{\epsilon}_\perp^{(1/2)}, -\epsilon_0), \quad (\text{C.15})$$

$$\vec{\epsilon}_\perp^{(1)} \cdot \vec{\epsilon}_\perp^{(2)} = 0. \quad (\text{C.16})$$

Depending on the parameterisation of k^μ the explicit form of

$$\epsilon_0 = \frac{\vec{\epsilon}_\perp \vec{k}_\perp}{k_0 + k_z} \quad (\text{C.17})$$

is obtained from the Lorentz condition $\epsilon k = 0$. For the transverse polarization vectors we use $\vec{\epsilon}_\perp^{(1)} = (1, 0)$ and $\vec{\epsilon}_\perp^{(2)} = (0, 1)$ in the numerical calculations. It is necessary to take care of singularities of coordinates. Such a problem arises in ϵ_0 for $\theta \rightarrow \pi$. So this gauge is restricted to forward emission angles.

It was generally stated above that the set of polarizations obtained here may be transformed under (C.4) whereby physical observables remain invariant. Clearly, this transformation can be used with $\beta = -\epsilon_0/\omega$ to eliminate the component ϵ_0 . Then, the situation is as in the A^0 -gauge case, but the three-dimensional polarizations may differ from the set used in the A^0 -gauge by an rotation about the momentum direction. If we investigate circular polarizations or carry out a summation over polarizations this point has no importance, only for particular linear polarization states it has to be taken into account to test gauge invariance with respect to the transformation (C.4). Note that $\beta \rightarrow 0$ for $\theta \rightarrow 0$, hence the A^+ - and A^0 -gauge should agree for angles close enough to zero.

$A^- = 0$ gauge

In a similar manner the condition $A^- = 0$ can be achieved

$$\epsilon^{(1/2)} = (\epsilon'_0, \vec{\epsilon}_\perp^{(1/2)}, \epsilon'_0), \quad (\text{C.18})$$

$$\vec{\epsilon}_\perp^{(1)} \cdot \vec{\epsilon}_\perp^{(2)} = 0, \quad (\text{C.19})$$

where

$$\epsilon'_0 = \frac{\vec{\epsilon}_\perp \vec{k}_\perp}{k_0 - k_z}. \quad (\text{C.20})$$

This choice of coordinates is numerically well defined for backward emission but diverges for $\theta \rightarrow 0$. As argued in the case of the A^+ -gauge the transformation equation (C.4) with $\beta = -\epsilon'_0/\omega$ suggests agreement of the A^- - and A^0 -gauge in the limit $\theta \rightarrow \pi$.

The A^- -gauge is of interest, since in the CMS the diagrams with projectile emission in the A^+ -gauge should refer to the target emission contributions in the A^- -gauge as follows. Say we consider a collision of equally heavy projectile and target particles in the CMS with the emission of the gluon from the projectile line where we obtain a specific angular pattern of the radiation amplitude. Let us assume now that the z -direction is reversed, which in the CMS means equivalently the interchange of projectile and target. What follows is that the previous projectile emission pattern now becomes the new target angular emission behaviour. But if also all other z -components are exchanged, that is to say in the momentum of the gluon we set $k_z \rightarrow -k_z$ (this is realized by the substitution $\theta \rightarrow \pi - \theta$) and in the polarization we write $\epsilon_z \rightarrow -\epsilon_z$, one would expect that the new target distribution is identical to the previous radiation behaviour from emission off the projectile line.

In particular, $\epsilon_z \rightarrow -\epsilon_z$ leads to $A^+ \rightarrow A^-$ and vice versa. Therefore we find a symmetry of the radiation amplitudes in the CMS with respect to the "exchange transformation"

$$\left. \begin{array}{l} \text{projectile} \leftrightarrow \text{target} \\ A^+ \leftrightarrow A^- \\ \theta \leftrightarrow \pi - \theta \end{array} \right\} \quad (\text{C.21})$$

This is of course restricted to a symmetric kinematical situation, that is to say, equal quark masses and small transverse momentum transfer.

Numerical Tests of Gauge Invariance in Polarization States

The three gauges are compared numerically for the process of one gluon emission induced by the single scattering of two quarks in Figs. C.1, C.2 and C.3. The symmetry properties between the A^+ - and A^- -gauge are very well confirmed by comparison of Figs. C.1 and C.2. Moreover one finds that the graphs for the A^0 -gauge obey an axial symmetry about the axis $\theta = \frac{\pi}{2}$, which can clearly be understood since Eqs. (C.12), (C.13) are invariant under $\theta \leftrightarrow \pi - \theta$. Note that the three-gluon contribution diagram, Fig. C.3(a), fits well in this symmetry argument for A^0 . The behaviour of the A^0 -gauge result for $\theta \rightarrow \frac{\pi}{2}$ is due to the specific coordinates where for $\theta \rightarrow \frac{\pi}{2}$ only z -components remain from products with polarization vectors in the matrix element expressions in contrast to the other gauges. Thus the sharp decrease for $\theta \rightarrow \frac{\pi}{2}$ is explained, it is not a divergence.

In spite of this comparing A^+ and A^- for the three-gluon contribution, Fig. C.3(a) reveals deviations in the angular range $\theta \sim \frac{\pi}{2}$. These result from the fact that we have not reversed the situation properly, since the fixed momentum transfer is defined at the target line in the A^+ -gauge but not redefined to the projectile in the calculation of the case of the A^- -gauge.

It should be pointed out that the single contributions in this three gauges are quite different but the total matrix element is in this kinematical region gauge invariant, Fig. C.3(b).

The transformation equations between these three gauges show for which gluon emission angles there is agreement between the three cases. Thus, the A^0 -gauge is equivalent to the A^+ -gauge for forward emission of the gluon ($\theta \rightarrow 0$) and equivalent to the A^- -gauge for backward emission ($\theta \rightarrow \pi$). In Fig. C.1 we find this agreement between A^+ - and A^- -gauge as well as in Fig. C.2 for the combination A^- and A^0 -gauge. However the angle θ is not close enough to π for the A^- - and A^0 -gauge to meet in Fig. C.1, as $\theta \rightarrow 0$ is not reached in Fig. C.2 for an identification of the A^+ and A^0 -gauge. These relations based on Eq. (C.4) are all satisfied in Fig. C.3(a) for the three-gluon case.

In summary, besides the discussion of symmetry properties between different gauges and contributions, we emphasize the numerically confirmed gauge invariance of the total result. It could be shown that target contributions are negligible in the A^+ -gauge. This is an important feature to justify the potential model, which applies the A^+ -gauge and thus needs only to evaluate emission contributions coming from the projectile.

C.2.2 Gauge Invariance for the Gluon Propagator

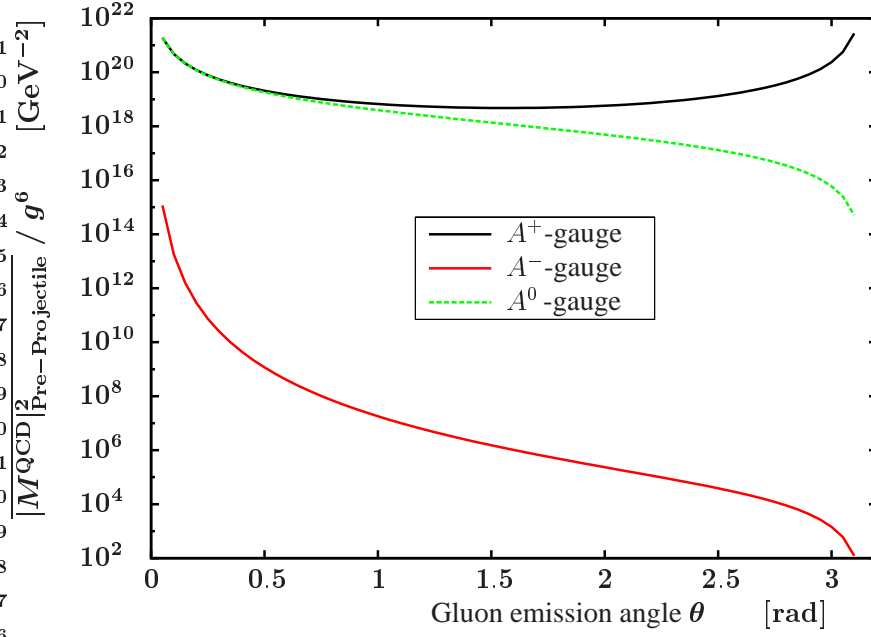
Numerical Tests

Besides the freedom of fixing the polarization states the propagator of the gluon, which so far has been used in Feynman gauge, can be modified according to

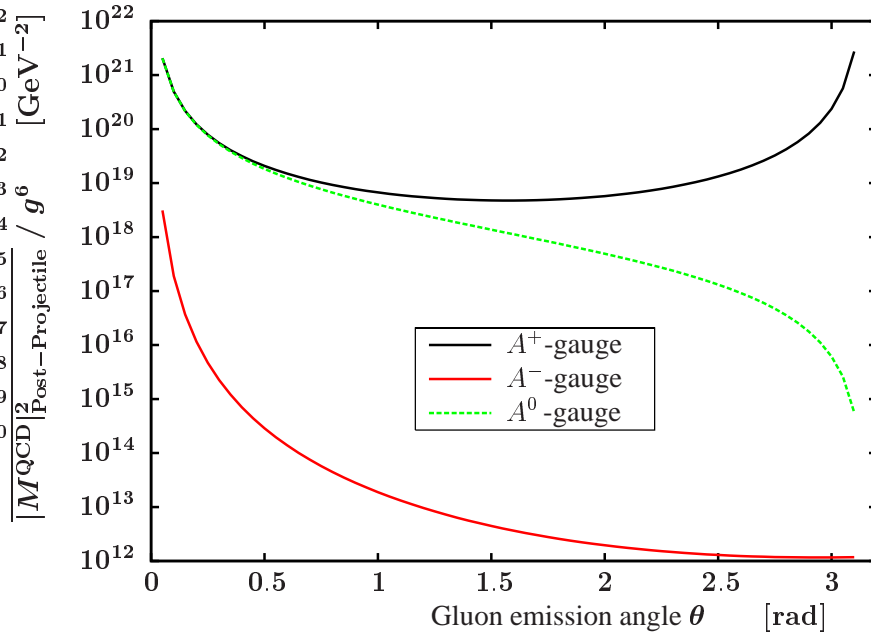
$$D(k)^{\mu\nu} = \frac{-1}{k^2 + i\epsilon} \left(g^{\mu\nu} - (1 - \lambda) \cdot \frac{k^\mu k^\nu}{k^2 + i\epsilon} \right). \quad (\text{C.22})$$

The introduced gauge parameter λ recovers in particular the Feynman gauge ($\lambda \rightarrow 1$) or the Landau gauge ($\lambda \rightarrow 0$). In Fig. C.4 we exhibit results for different choices of fixing the gauge freedom by λ . The numerical results show gauge invariance with respect to λ in all single contributions, not shown here, and in the total matrix element, Fig. C.4. However, this may be also due to the smallness of the transverse momentum transfer which restricts the amount of the gauge varying term in the gluon propagator. The same calculation using spinor rules does not show any significant differences.

Analytically and numerically we restrict all calculations to the Feynman gauge. Although it is possible to show that a gauge term proportional to $k^\mu k^\nu$ vanishes at least for the simple elastic

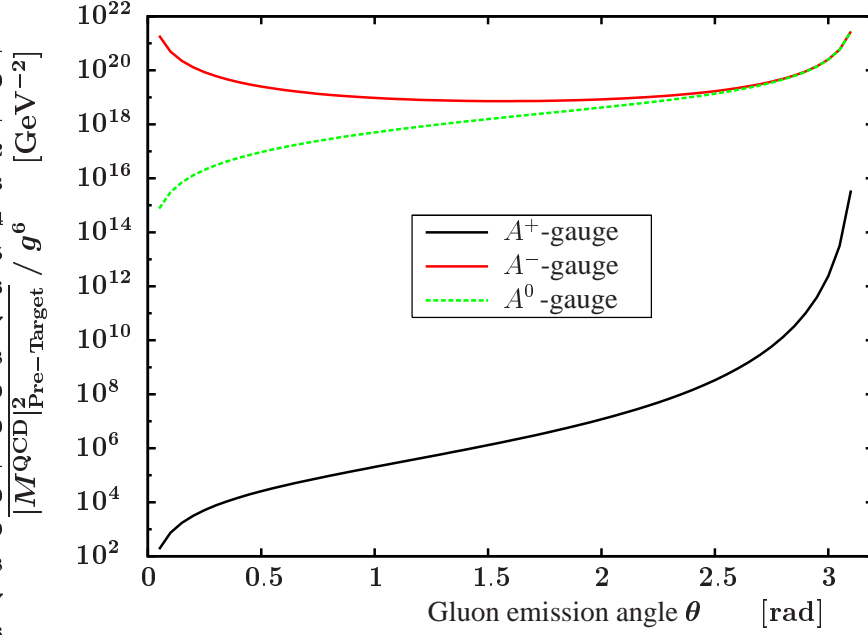


(a) Pre projectile contributions.

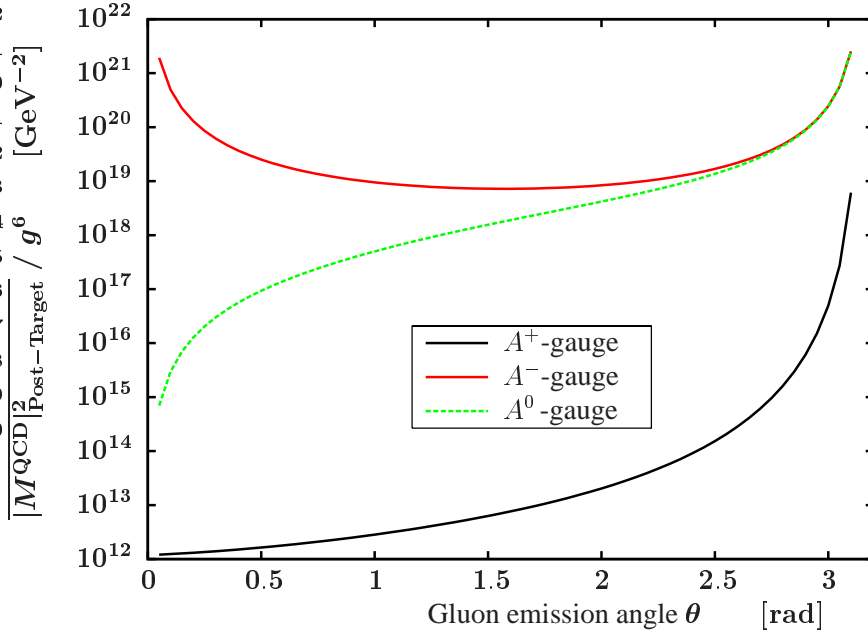


(b) Post projectile contributions.

Figure C.1: Projectile contributions to the summed and averaged squared matrix element for gluon emission in the scattering of two down quarks from scalar QCD as a function of the emission angle θ compared for different gauges. The parameters are specified in Fig. C.3, where one finds gauge invariance for the total outcome.

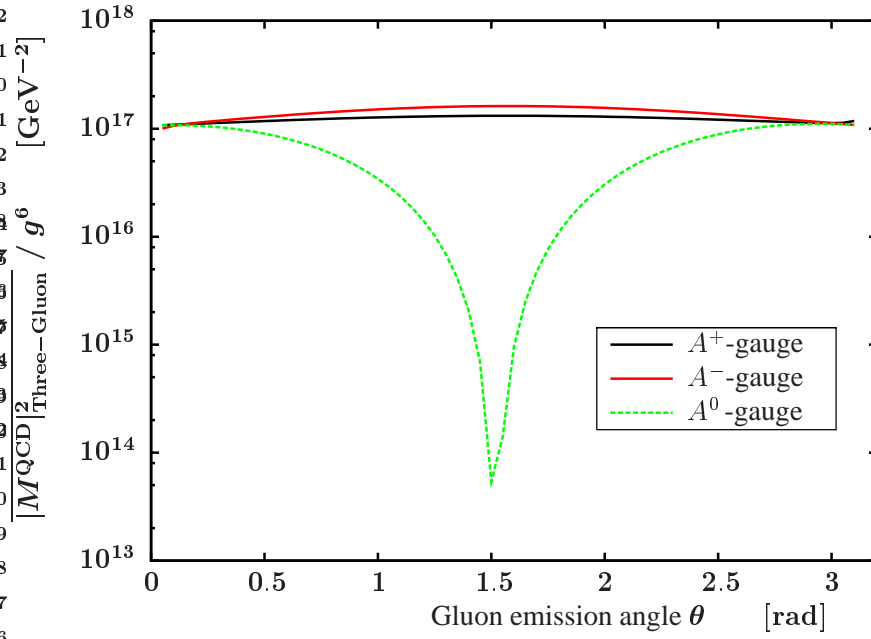


(a) Pre target contributions.

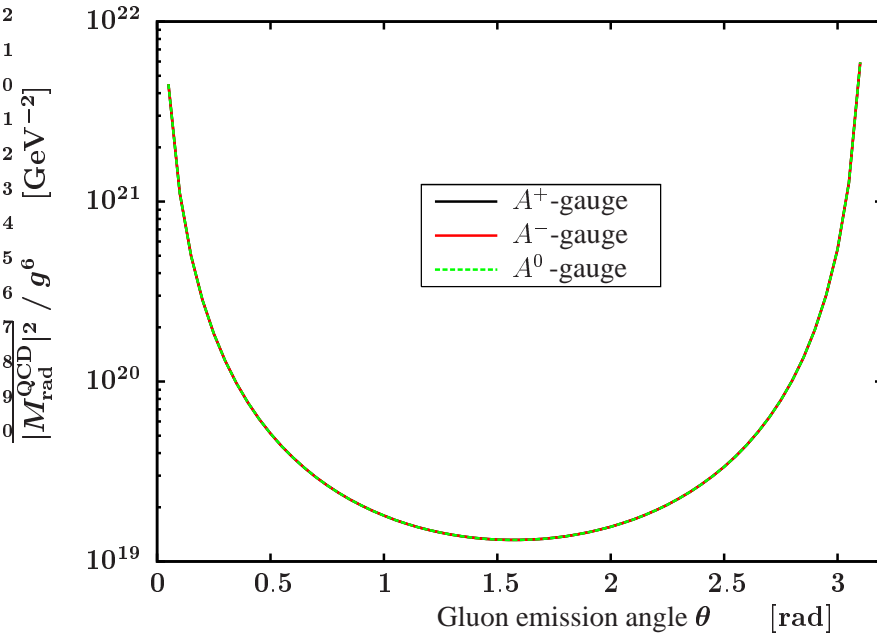


(b) Post target contributions.

Figure C.2: Target contributions to the summed and averaged squared matrix element for gluon emission in the scattering of two down quarks from scalar QCD as a function of the emission angle θ compared for different gauges. The parameters are stated in Fig. C.3. It shows that in the A^+ -gauge the target contributions are negligible with respect to the contributions from emission off the projectile, Fig. C.1.



(a) Three gluon contributions.



(b) Total matrix element taking all diagrams.

Figure C.3: The summed and averaged squared matrix element for gluon emission in the scattering of two down quarks from scalar QCD is exhibited as a function of the emission angle θ compared for different gauges. In (a) the contributions from the three-gluon vertex are found to be relevant in all gauges. The total matrix element (b), obtained as coherent sum of all diagrams, however is gauge invariant, that is to say the results in different gauges fall together. The results are for forward scattering in the CMS in the Feynman gauge with parameters $m_1 = m_2 = m_{\text{down}} = 0.007 \text{ GeV}/c^2$, $\vec{p}_1 = (0, 0, 5) \text{ GeV}/c$, $\vec{p}_2 = (0, 0, -5) \text{ GeV}/c$, $\omega = 0.001 \text{ GeV}$, $\theta = 0 \dots \pi$, $\phi = \pi/2$, $q_x = 0$, $q_y = 0.01 \text{ GeV}/c$, $\sqrt{s} = 10 \text{ GeV}/c$.

scattering diagram Fig. D.1, we will not pursue this problem further. The latter independence of the gauge fixing term written in terms of the relevant spinor product¹

$$\bar{u}(p_f)\gamma_\mu u(p_i)k^\mu k^\nu \bar{u}(p'_f)\gamma_\nu u(p'_i) = \bar{u}(p_f)\not{k}u(p_i)\bar{u}(p'_f)\not{k}u(p'_i) = 0 \quad (\text{C.23})$$

results because the spinors obey the Dirac equation

$$\bar{u}(\not{p} - m) = (\not{p} - m)u = 0. \quad (\text{C.24})$$

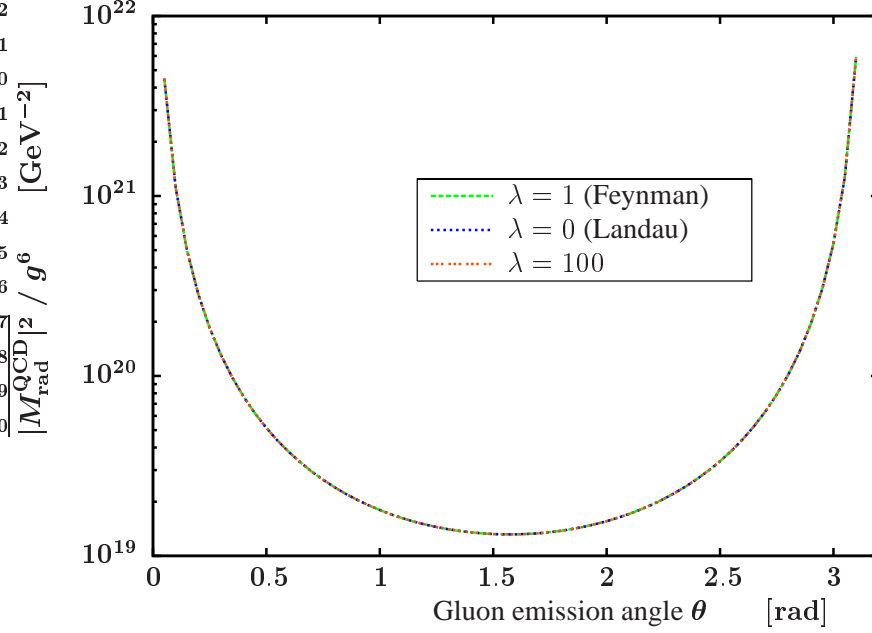


Figure C.4: The summed and averaged squared matrix element for gluon emission in the scattering of two down quarks from scalar QCD is exhibited as a function of the emission angle θ compared for different gauges of the gluon propagator (denoted by the gauge parameter λ). The total matrix element is gauge invariant, that is to say the results in different gauges fall together. The results are for forward scattering in the CMS in the A^+ -gauge with parameters $m_1 = m_2 = m_{\text{down}} = 0.007 \text{ GeV}/c^2$, $\vec{p}_1 = (0, 0, 5) \text{ GeV}/c$, $\vec{p}_1 = (0, 0, -5) \text{ GeV}/c$, $\omega = 0.001 \text{ GeV}$, $\theta = 0 \dots \pi$, $\phi = \pi/2$, $q_x = 0$, $q_y = 0.01 \text{ GeV}/c$, $\sqrt{s} = 10 \text{ GeV}/c$.

C.3 Polarization Matrix

The degree of polarization can be expressed in terms of a polarization matrix

$$\rho_{\alpha\beta} = \frac{1}{2} \begin{pmatrix} 1 + \xi_3 & \xi_1 - i\xi_2 \\ \xi_1 + i\xi_2 & 1 - \xi_3 \end{pmatrix}, \quad (\text{C.25})$$

which includes 3 real parameters, namely the Stokes parameters ξ_1 , ξ_2 and ξ_3 with allowed values $-1 \leq \xi_i \leq 1$. The probability for a particular polarization e is then obtained from the projection

$$p_{(e)} = \epsilon^\dagger \rho \epsilon. \quad (\text{C.26})$$

¹The slash symbol / stands for the contraction of a Lorentz quantity A^μ with the Gamma matrices γ_ν , $\not{A} \equiv A^\mu \gamma_\mu$.

The parameters ξ_i carry information on the contribution from the following gluon polarization states

$$\xi_1 = \begin{cases} 1 & \text{linear polarization vector } \epsilon^{(+)} = \frac{1}{\sqrt{2}} (\epsilon^{(1)} + \epsilon^{(2)}), \\ -1 & \text{linear polarization vector } \epsilon^{(-)} = \frac{1}{\sqrt{2}} (\epsilon^{(1)} - \epsilon^{(2)}), \end{cases} \quad (\text{C.27})$$

$$\xi_2 = \begin{cases} 1 & \text{circular polarization vector } \epsilon^{(+)} = -\frac{i}{\sqrt{2}} (\epsilon^{(1)} + i\epsilon^{(2)}), \\ -1 & \text{circular polarization vector } \epsilon^{(-)} = \frac{i}{\sqrt{2}} (\epsilon^{(1)} - i\epsilon^{(2)}), \end{cases} \quad (\text{C.28})$$

$$\xi_3 = \begin{cases} 1 & \text{linear polarization vector } \epsilon^{(1)}, \\ -1 & \text{linear polarization vector } \epsilon^{(2)}. \end{cases} \quad (\text{C.29})$$

The numerical calculations yield the values for

$$p_{(1)} = \epsilon^{(1)\dagger} \rho \epsilon^{(1)}, \quad p_{(2)} = \epsilon^{(2)\dagger} \rho \epsilon^{(2)}, \quad (\text{C.30})$$

$$p_{(+)} = \epsilon^{(+)\dagger} \rho \epsilon^{(+)}, \quad p_{(-)} = \epsilon^{(-)\dagger} \rho \epsilon^{(-)}. \quad (\text{C.31})$$

Since ρ is an adjoint matrix and the relation

$$\xi_1^2 + \xi_2^2 + \xi_3^2 = 1 \quad (\text{C.32})$$

holds for a completely polarized gluon, we may express the Stokes values by

$$|\xi_1| = 2\sqrt{p_{(1)}p_{(2)}}, \quad (\text{C.33})$$

$$\xi_2 = 2p_{(+)} - 1 = 1 - 2p_{(-)}, \quad (\text{C.34})$$

$$\xi_3 = 2p_{(1)} - 1 = 1 - 2p_{(2)}. \quad (\text{C.35})$$

Furthermore, in the case when $\xi_2 = 0$, that is to say, the gluon is fully linear polarized, the direction of the transverse polarization vector becomes accessible by the following argument. If there is no circular contribution, the general linear polarization vector is spanned by

$$\epsilon = a\epsilon^{(1)} + b\epsilon^{(2)}. \quad (\text{C.36})$$

This corresponds obviously to a rotation about the k -axis. Note, that this rotation does not influence on the results for circular polarization vectors. A comparison with the four-dimensional generalization of the polarization matrix

$$\begin{aligned} \rho_{\mu\nu} = & \frac{1}{2} (\epsilon_\mu^{(1)}\epsilon_\nu^{(1)} + \epsilon_\mu^{(2)}\epsilon_\nu^{(2)}) + \frac{\xi_1}{2} (\epsilon_\mu^{(1)}\epsilon_\nu^{(2)} + \epsilon_\mu^{(2)}\epsilon_\nu^{(1)}) \\ & - i\frac{\xi_2}{2} (\epsilon_\mu^{(1)}\epsilon_\nu^{(2)} - \epsilon_\mu^{(2)}\epsilon_\nu^{(1)}) + \frac{\xi_3}{2} (\epsilon_\mu^{(1)}\epsilon_\nu^{(1)} - \epsilon_\mu^{(2)}\epsilon_\nu^{(2)}) \end{aligned} \quad (\text{C.37})$$

yields

$$a = \pm\sqrt{p_{(1)}}, \quad b = \pm\sqrt{p_{(2)}}. \quad (\text{C.38})$$

In this manner, we can detect the realized polarization direction from the results for $e^{(1)}$, $e^{(2)}$, $e^{(+)}$ and $e^{(-)}$. The results for the polarization directions obtained in the calculations refer to the three-dimensional transverse basis defined in Section (C.2.1).

In Fig. C.6(a) we demonstrate this for the case of completely linear polarization $\epsilon^{(1)}$. The ratios of different polarizations contributions to the total matrix element as a function of the emission angle θ are shown for linear polarizations in Fig. C.6(a) and for circular polarization vectors in Fig. C.6(b). The sum of each ratio pair of course equals 1. In Fig. C.5 we check that the choice of polarizations does not effect for the summed and averaged squared matrix element. Furthermore the same calculations were carried out with spinor rules but no difference was found.

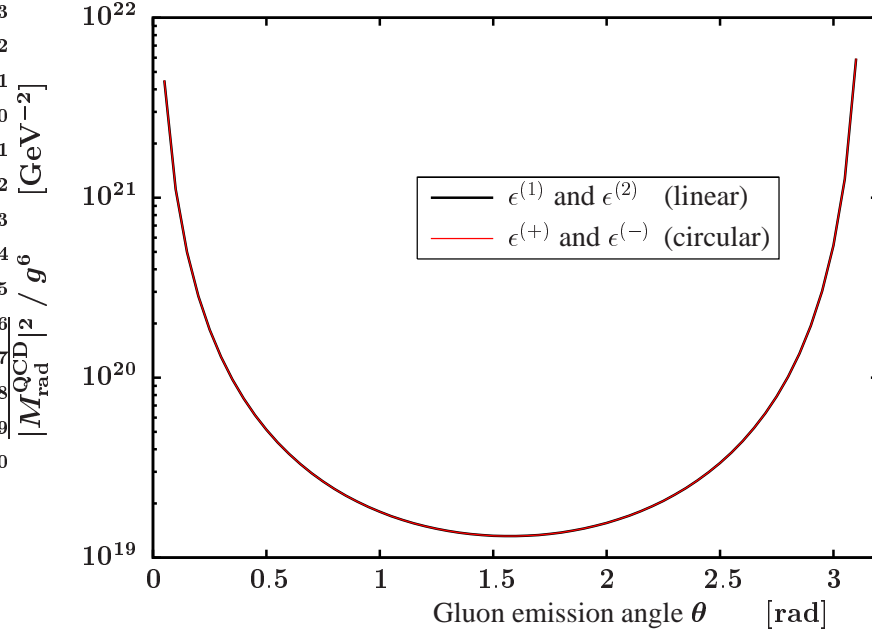
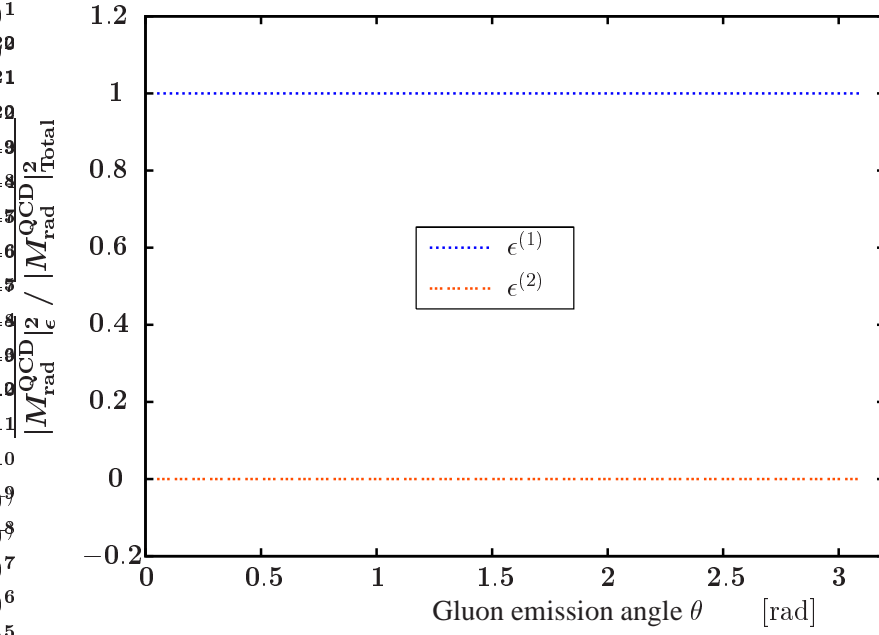
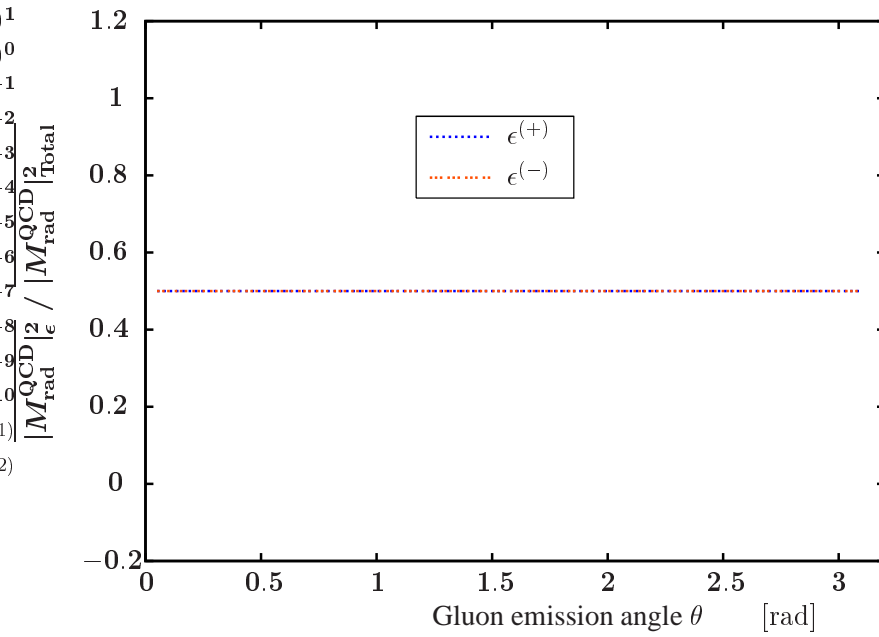


Figure C.5: The summed and averaged squared matrix element for gluon emission in the scattering of two down quarks from scalar QCD is exhibited as a function of the emission angle θ compared for linear and circular polarization vectors, see also Figs. C.6. The result is invariant with respect to this choices, that is to say the lines fall together. The results are for forward scattering in the CMS in the A^0 -gauge and the Feynman gauge with parameters $m_1 = m_2 = m_{\text{down}} = 0.007 \text{ GeV}/c^2$, $\vec{p}_1 = (0, 0, 5) \text{ GeV}/c$, $\vec{p}_2 = (0, 0, -5) \text{ GeV}/c$, $\omega = 0.001 \text{ GeV}$, $\theta = 0 \dots \pi$, $\phi = \pi/2$, $q_x = 0$, $q_y = 0.01 \text{ GeV}/c$, $\sqrt{s} = 10 \text{ GeV}/c$.



(a) Linear polarizations.



(b) Circular polarizations, both lines fall together.

Figure C.6: Relative polarization contributions to the summed and averaged squared matrix element for gluon emission in the scattering of two down quarks from scalar QCD as a function of the emission angle θ compared for (a) linear and (b) circular polarizations. The parameters are specified in Fig. C.5.

Appendix D Gunion-Bertsch Limit

The first discussion of induced gluon radiation was done by Gunion and Bertsch (GB) [Gun82] in the limit of high quark energies and soft gluon energies. Furthermore, they have used the A^+ -gauge, massless quarks and neglected the spins, thus they worked in scalar QCD with particle masses $m = 0$. The calculation was carried out in CMS. For completeness we give the relevant expressions.

This first approach could be used as check for the program code as follows. The matrix elements for induced gluon radiation are calculated numerically in CMS for the case of transverse gluons. The results are compared to the approximation of Gunion and Bertsch.

Note that a different naming for the momentum transfer $l = p'_f - p'_i$ instead of q used elsewhere in this thesis is written. This corresponds to the definition given in [Gun82].

D.1 Elastic Scattering

The investigation of the elastic scattering matrix element, Fig. D.1, is a necessary prerequisite for the induced gluon radiation processes because the elastic part is factored out to obtain the radiation amplitude. Therefore the GB approximations for elastic scattering are checked in Fig. D.2. In the down quark scattering no considerable differences to numerical results appear in the regime of small momentum transfers, Fig. D.2. The curves lie on the GB line, of course they deviate if the transferred perpendicular momentum becomes larger with respect to the initial momenta of the quarks in CMS, $l_\perp \sim p$.

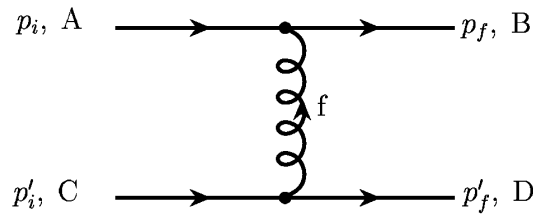


Figure D.1: Elastic scattering of two quarks with one gluon exchanged.

The relevant expressions for elastic scattering are

$$C_{\text{elastic}} = (T^f)_{AB}(T^f)_{CD}, \tag{D.1}$$

$$M_{\text{elastic}}^{\text{scalar}} = C_{\text{elastic}} \cdot ig^2 \cdot \frac{(p_f + p_i)_\mu (p'_f + p'_i)^\mu}{(p_f - p_i)^2}, \tag{D.2}$$

$$M_{\text{elastic}}^{\text{GB}} = C_{\text{elastic}} \cdot (-ig^2) \frac{2s}{l_\perp^2}. \tag{D.3}$$

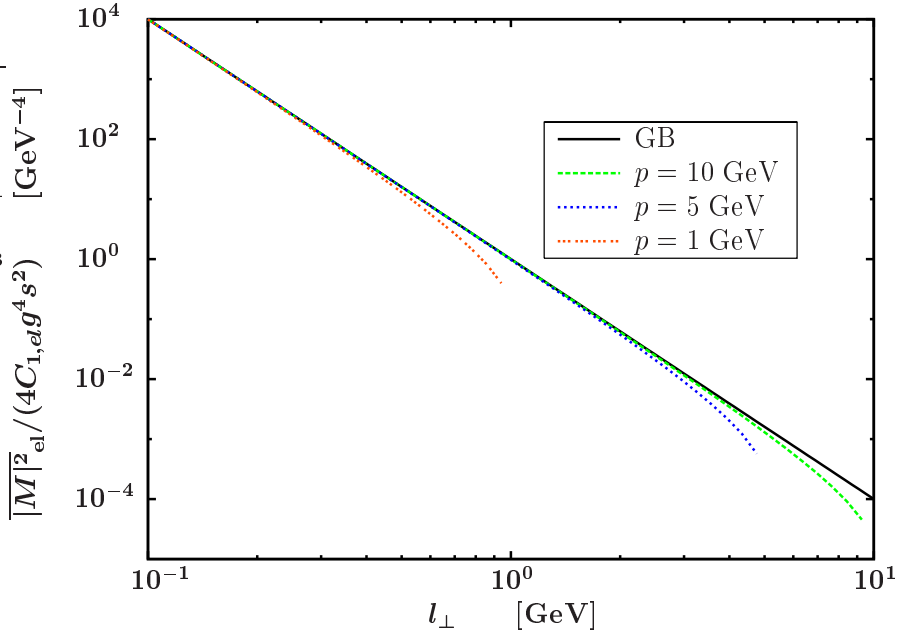


Figure D.2: Elastic scattering of two down quarks. The normalized summed and averaged squared matrix element is shown as a function of the transverse momentum transfer l_{\perp} .

Note, that in the high-energy limit and for small momentum transfers it is straightforward to obtain the invariant differential cross section

$$\frac{d\sigma}{dt} = C_{1,\text{el}} \frac{2\pi\alpha^2 s^2 + u^2}{s^2 t^2} \quad (\text{D.4})$$

for the elastic scattering from a spinor calculation, where $\alpha = \frac{g^2}{4\pi}$ is the coupling constant, the colour factor $C_{1,\text{el}}$ is defined in Eq. (A.13) and s , t and u are the usual Mandelstam variables, cf. Eq. (3) in [Wan95].

However, suppression of the GB matrix element can be seen in other mass configurations. If we extend the GB approach including finite masses it is not sufficient to calculate the changed invariant CMS energy s in Eq. (D.3). This problem is due to the identity $s = 2p$ in CMS which does not hold for $m \neq 0$. A new derivation for $m \neq 0$ yields

$$\overline{|M|}_{\text{el}}^2 = K^2 \cdot \overline{|M|}_{\text{el,GB}}^2 \quad (\text{D.5})$$

where

$$K = 1 - \frac{x^2 + y^2}{\sqrt{1+x^2} + \sqrt{1+y^2}} \quad (\text{D.6})$$

and the masses are given in units of the initial momentum p of the colliding particles in CMS, $x = \frac{m_1}{p}$ and $y = \frac{m_2}{p}$. Since $K < 1$ this results in a reduction of the matrix element compared to the GB result. In Fig. D.3 this factor is visualized. In the limit $x, y \rightarrow 0$ one recovers the GB expressions, $K \rightarrow 1$. Therefore in order to make reasonable comparisons with GB we will restrict the following calculations to light particles.

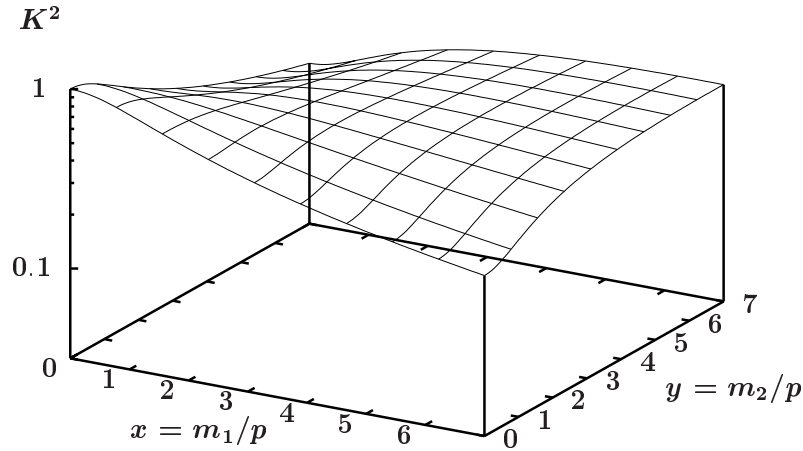


Figure D.3: The mass dependence of the ratio $K^2 = \overline{|M|}_{\text{el}}^2 / \overline{|M|}_{\text{el,GB}}^2$ is shown. In the limit of massless particles GB is recovered, otherwise suppression occurs.

D.2 Inelastic Scattering

D.2.1 Single Contributions to Gluon Radiation

We consider the emission of gluons perpendicular to the initial momenta of the colliding quarks. Since the GB approximations use massless quarks we consider two equally light quarks with mass $m = 0.007$ GeV (down quarks) and each carrying the momentum $p = 10$ GeV in CMS. These momenta define the z -direction. The transverse momentum transfer is taken to be $l_{\perp} = l_y = 0.01$ GeV for example. The transverse component k_{\perp} of the gluon is also measured in y -direction.

The plots compare the squared summed and averaged matrix elements (colours and polarizations) for the single radiation contributions in Fig. D.4. The formula for GB are used as shown, in the target line radiation case, we have shown the terms which come from the GB calculation although these terms are not taken into account for the GB approximation of the total matrix element.

In the three-dimensional plot, Fig. D.11, the situation for different angles is considered, as well. All numerical calculations are in good agreement with the GB approximation for small ω . Of course, this is not true if the soft radiation limit is abandoned.

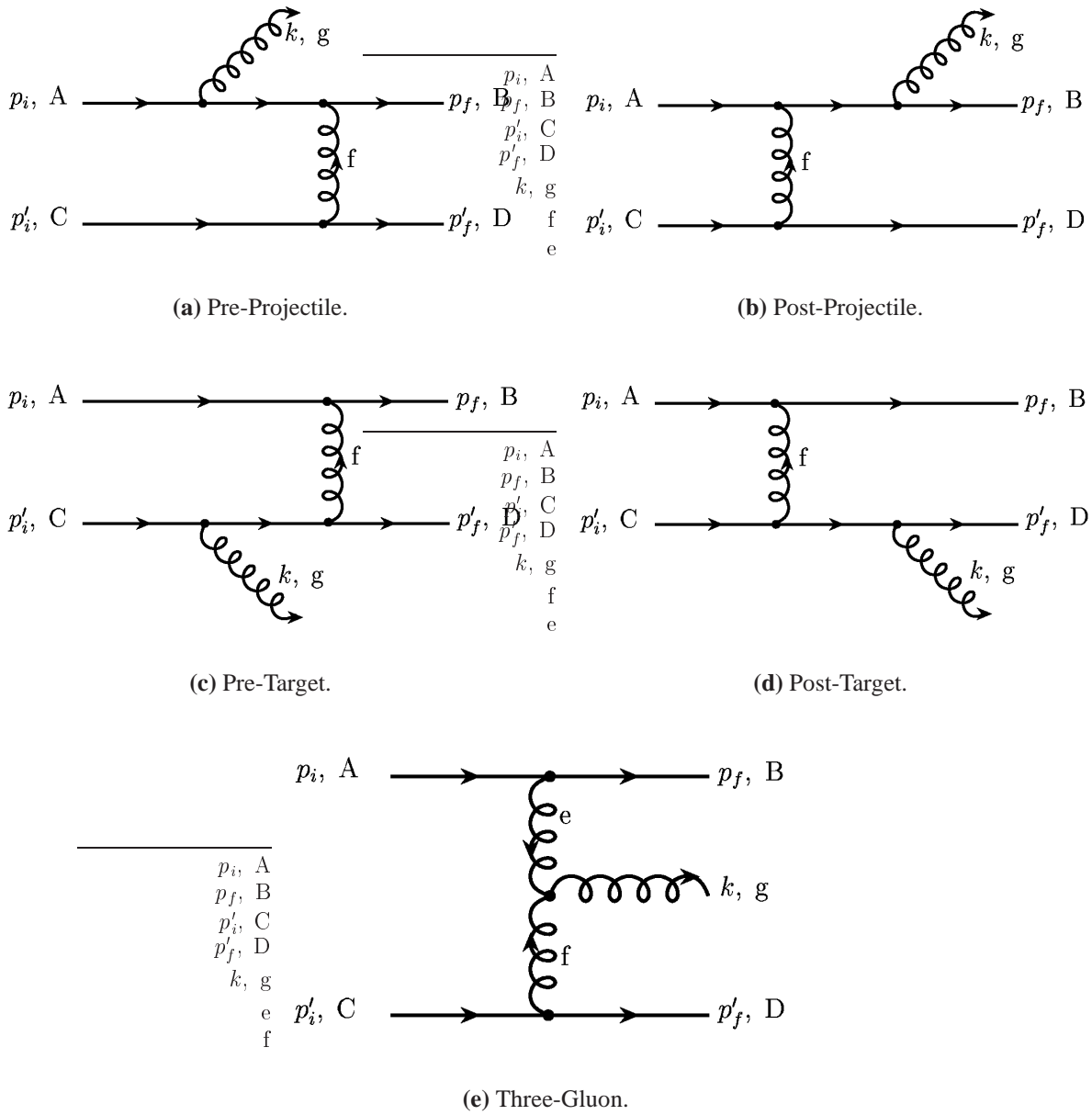


Figure D.4: Contributions to the inelastic scattering of two quarks with one gluon being emitted.

Pre-Projectile Contribution

The relevant expressions for the pre-projectile diagram, Fig. D.4(a), which are numerically compared in Fig. D.5 are

$$C_{\text{prePro}} = (T^f T^g)_{AB} (T^f)_{CD}, \quad (\text{D.7})$$

$$M_{\text{prePro}}^{\text{scalar}} = C_{\text{prePro}} \cdot i g^3 \frac{(p_f + p_i - k)_\mu (p'_f + p'_i)^\mu \cdot (2p_i - k)_\nu \epsilon^\nu}{[(p_i - k)^2 - m^2] \cdot (p'_f - p'_i)^2}, \quad (\text{D.8})$$

$$\frac{M_{\text{prePro}}^{\text{GB}}}{M_{\text{elastic}}^{\text{GB}}} = \frac{C_{\text{prePro}}}{C_{\text{elastic}}} \cdot (-2g) \frac{\vec{\epsilon}_\perp \vec{k}_\perp (1-x)}{k_\perp^2}. \quad (\text{D.9})$$

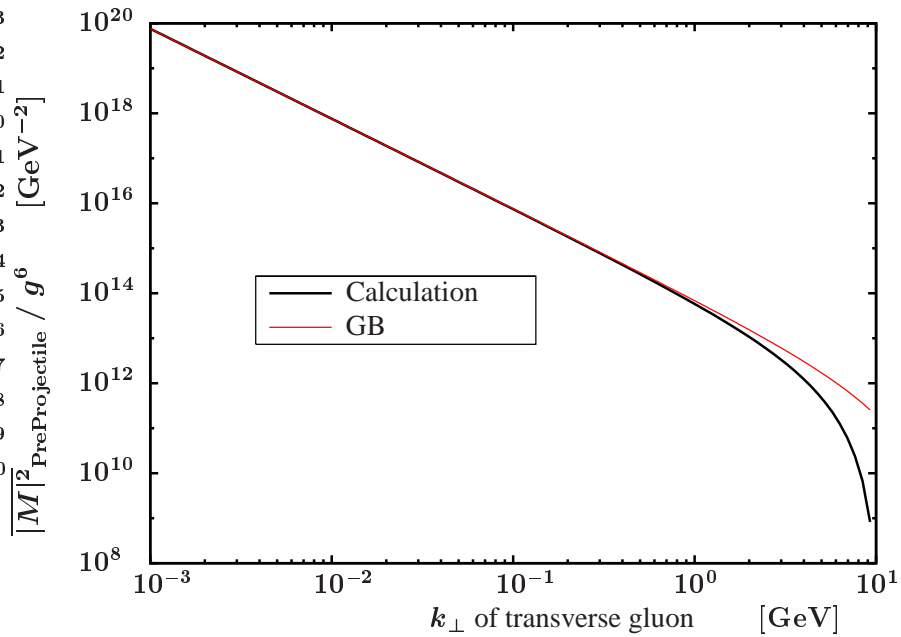


Figure D.5: For the *pre-projectile contribution* the summed and averaged squared matrix element as a function of the perpendicular momentum component of a transverse emitted gluon calculated numerically is compared to the GB approximation.

Post-Projectile Contribution

The relevant expressions for the post-projectile diagram, Fig. D.4(b), which are numerically compared in Fig. D.6 are

$$C_{\text{postPro}} = (T^g T^f)_{AB} (T^f)_{CD}, \quad (\text{D.10})$$

$$M_{\text{postPro}}^{\text{scalar}} = C_{\text{postPro}} \cdot i g^3 \frac{(p_f + p_i + k)_\mu (p'_f + p'_i)^\mu \cdot (2p_f + k)_\nu \epsilon^\nu}{[(p_f + k)^2 - m^2] \cdot (p'_f - p'_i)^2}, \quad (\text{D.11})$$

$$\frac{M_{\text{postPro}}^{\text{GB}}}{M_{\text{elastic}}^{\text{GB}}} = \frac{C_{\text{postPro}}}{C_{\text{elastic}}} \cdot (-2g) \frac{-\vec{\epsilon}_\perp (\vec{k}_\perp - x \vec{l}_\perp) (1-x)}{(\vec{k}_\perp - x \vec{l}_\perp)^2}. \quad (\text{D.12})$$

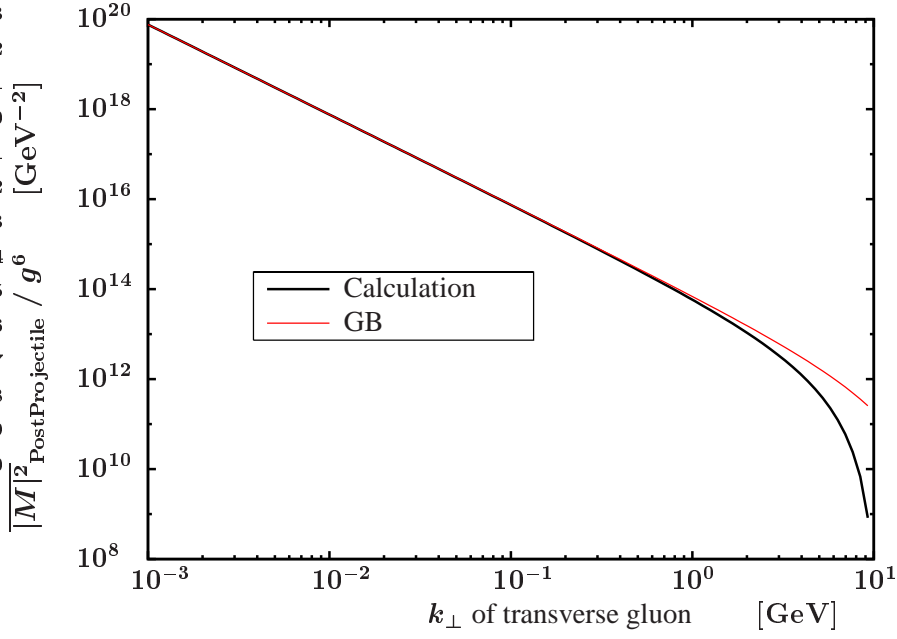


Figure D.6: For the *post-projectile contribution* the summed and averaged squared matrix element as a function of the perpendicular momentum component of a transverse emitted gluon calculated numerically is compared to the GB approximation.

Pre-Target Contribution

The relevant expressions for the pre-target diagram, Fig. D.4(c), which are numerically compared in Fig. D.7 are

$$C_{\text{preTar}} = (T^f)_{AB} (T^f T^g)_{CD}, \quad (\text{D.13})$$

$$M_{\text{preTar}}^{\text{scalar}} = C_{\text{preTar}} \cdot ig^3 \frac{(p'_f + p'_i - k)_\mu (p_f + p_i)^\mu \cdot (2p'_i - k)_\nu \epsilon^\nu}{[(p'_i - k)^2 - m'^2] \cdot (p_f - p_i)^2}, \quad (\text{D.14})$$

$$M_{\text{preTar}}^{\text{GB}} = 0. \quad (\text{D.15})$$

The divergent part arises from the singularity due to $(p_f - p_i)^2$. This can also be found in the post-target and three-gluon contribution. A further discussion is given below.

Post-Target Contribution

The relevant expressions for the post-target diagram, Fig. D.4(d), which are numerically compared in Fig. D.8 are

$$C_{\text{postTar}} = (T^f)_{AB} (T^g T^f)_{CD}, \quad (\text{D.16})$$

$$M_{\text{postTar}}^{\text{scalar}} = C_{\text{postTar}} \cdot ig^3 \frac{(p'_f + p'_i + k)_\mu (p_f + p_i)^\mu \cdot (2p'_f + k)_\nu \epsilon^\nu}{[(p'_f + k)^2 - m'^2] \cdot (p_f - p_i)^2}, \quad (\text{D.17})$$

$$M_{\text{postTar}}^{\text{GB}} = C_{\text{postTar}} \cdot 2ig^3 \frac{\vec{\epsilon}_\perp \vec{l}_\perp (2-x)(x-1)}{x(\vec{k}_\perp - \vec{l}_\perp)^2}. \quad (\text{D.18})$$

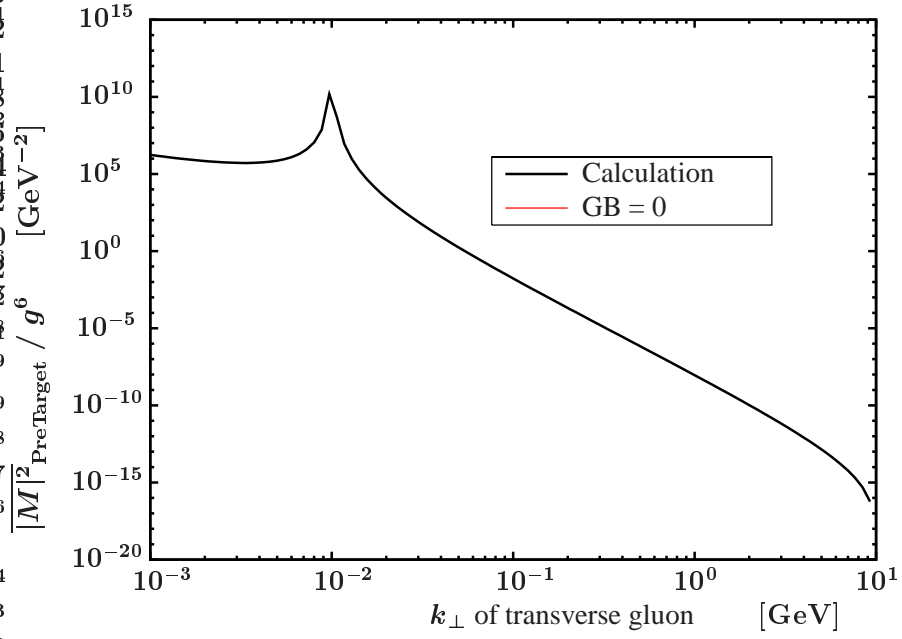


Figure D.7: For the *pre-target contribution* the summed and averaged squared matrix element as a function of the perpendicular momentum component of a transverse emitted gluon calculated numerically is compared to the GB approximation. Note in this case the predicted GB result equals zero.

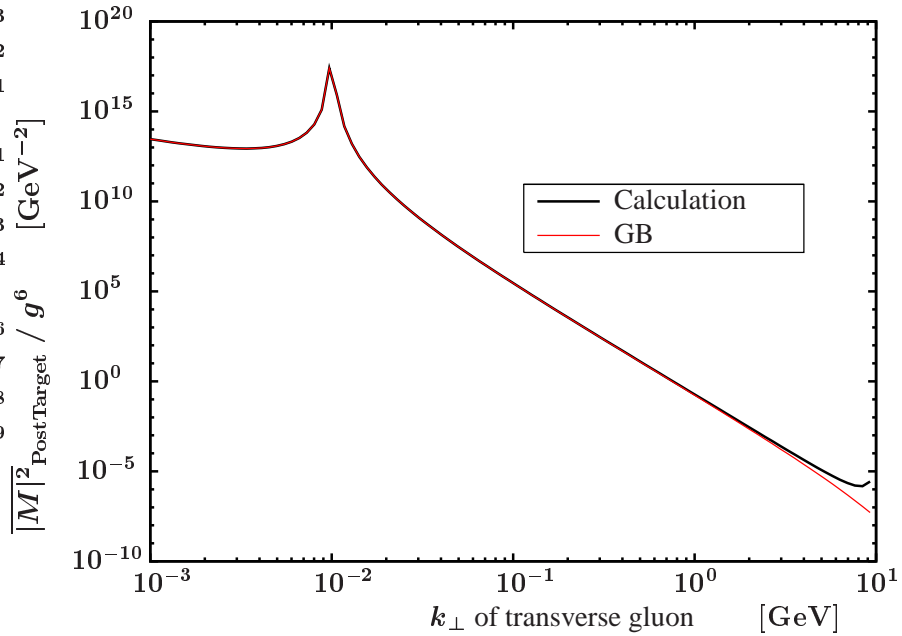


Figure D.8: For the *post-target contribution* the summed and averaged squared matrix element as a function of the perpendicular momentum component of a transverse emitted gluon calculated numerically is compared to the GB approximation.

Three-Gluon Contribution

The relevant expressions for the three-gluon diagram, Fig. D.4(e), which are numerically compared in Fig. D.9 are

$$C_{\text{threeGlu}} = i f_{egf}(T^e)_{AB}(T^f)_{CD}, \quad (\text{D.19})$$

$$M_{\text{threeGlu}}^{\text{scalar}} = C_{\text{threeGlu}} \cdot \frac{i g^3}{(p_i - p_f)^2 \cdot (p'_i - p'_f)^2} \cdot \left[(p_f + p_i)^\mu \epsilon_\mu \cdot (p_i - p_f + k)^\nu (p'_f + p'_i)_\nu \right. \\ \left. + (p_f + p_i)^\mu (p'_f - k - p'_i)_\mu \cdot (p'_f + p'_i)^\nu \epsilon_\nu \right. \\ \left. + (p'_i - p'_f - p_i + p_f)^\mu \epsilon_\mu \cdot (p_f + p_i)^\nu (p'_f + p'_i)_\nu \right], \quad (\text{D.20})$$

$$\frac{M_{\text{threeGlu}}^{\text{GB}}}{M_{\text{elastic}}^{\text{GB}}} = \frac{C_{\text{threeGlu}}}{C_{\text{elastic}}} \cdot (-2g) \frac{\vec{\epsilon}_\perp (\vec{k}_\perp - \vec{l}_\perp)(1-x)}{(\vec{k}_\perp - \vec{l}_\perp)^2}. \quad (\text{D.21})$$

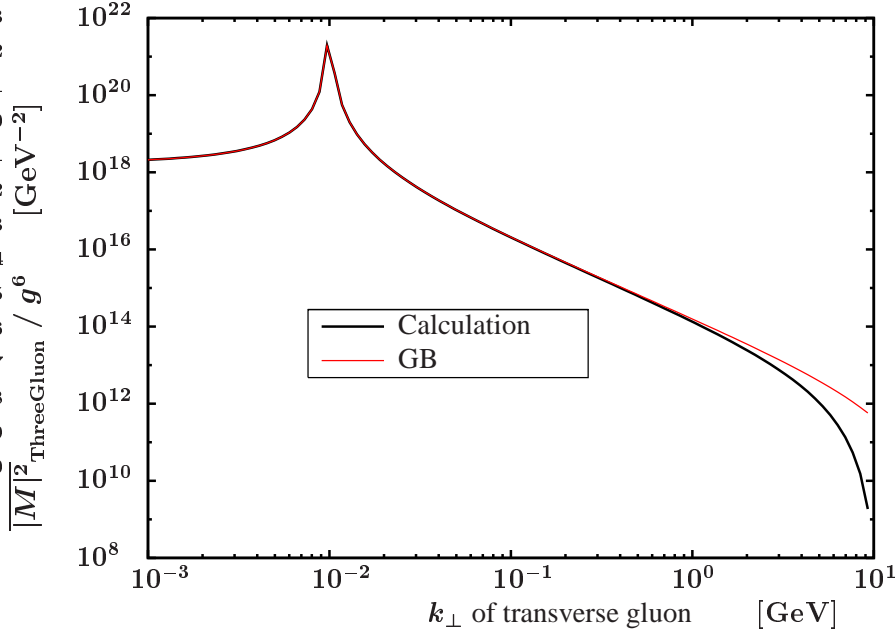


Figure D.9: For the *three-gluon contribution* the summed and averaged squared matrix element as a function of the perpendicular momentum component of a transverse emitted gluon calculated numerically is compared to the GB approximation.

D.2.2 Total Matrix Element

Within the GB approach, the contributions where the emission occurs at the target line are neglected. In addition, the $x \rightarrow 0$ limit is assumed. In this kinematical situation with transverse gluons ($k_z = 0$, $\omega = k_\perp$) and quark masses much smaller than the initial momentum per particle ($P^+ = 2E = s$)¹ the value of x is determined by $x = \frac{\omega}{\sqrt{s}} = \frac{k_\perp}{20 \text{ GeV}}$. This accounts for the deviation of GB

¹The positive momentum fraction, termed P^+ , of the projectile is worked with in [Gun82].

for large transverse momenta of the gluon. For arbitrary angles the value of x is defined by $x = \frac{\omega}{\sqrt{s}} \cdot (1 + \cos \theta)$.

The expression which is displayed in Fig. D.10 reads

$$\frac{M_{\text{total}}^{\text{GB}}}{M_{\text{elastic}}^{\text{GB}}} = \frac{if_{efg}(F^e)_{AB}(F^f)_{CD}}{C_{\text{elastic}}} \cdot 2g \left(\frac{\vec{\epsilon}_{\perp} \vec{k}_{\perp}}{k_{\perp}^2} - \frac{\vec{\epsilon}_{\perp} (\vec{k}_{\perp} - \vec{l}_{\perp})}{(\vec{k}_{\perp} - \vec{l}_{\perp})^2} \right). \quad (\text{D.22})$$

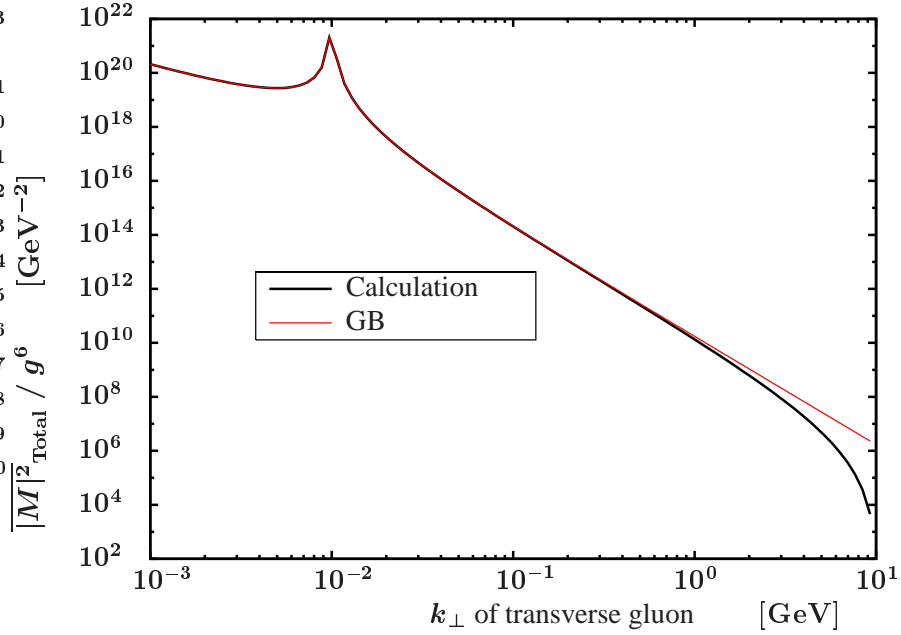


Figure D.10: For the *total result* the summed and averaged squared matrix element as a function of the perpendicular momentum component of a transverse emitted gluon calculated numerically is compared to the GB approximation.

Comment on the singularities The singularities in the diagrams for pre-target, post-target and three-gluon contribution are found at the same value of k_{\perp} . This is due to the expression $(p_f - p_i)^2$ in the denominator of the relevant matrix elements. The case $p_i = p_f$ corresponds to the equation $p'_i - p'_f \equiv l = k$, which reduces in the transverse gluon emission to the condition $l_{\perp} = \omega = k_{\perp}$. In general the singularity is expected for $l_{\perp} = \omega \cdot \sin \theta$.

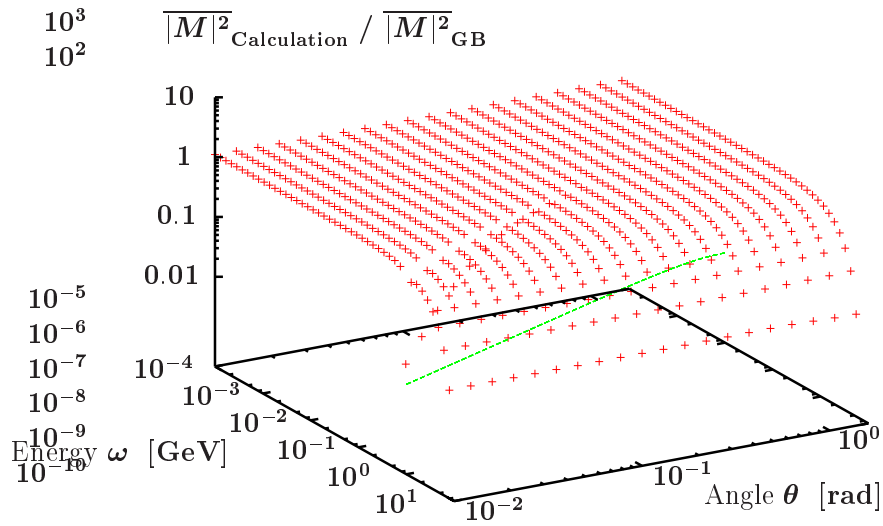


Figure D.11: The ratio between the numerically obtained total results for inelastic scattering to the GB outcome is shown as a function of gluon energy ω and emission angle θ . The projected straight line shows where singularities are placed.

Appendix E The C++ Program

The numerical investigation of the radiation diagrams is dealt with using several C++ programs, which are built up from a set of objects and functions.

Technically, the basic objects are three- and four-dimensional complex quadratic matrices together with complex row and column vectors of the same dimensions. These objects use the built-in class of complex numbers and are provided with the usual operations of matrix calculus.

The three-dimensional objects represent the colour parts of the Feynman rules, the four-dimensional objects realize the spinor algebra.

For the sake of reproducibility of the numerical results we give a compilation of important definitions and conventions. Lorentz indices are denoted in Greek letters and run over $0 \dots 3$, if spatial indices are meant these are written in Latin letters and run over $1 \dots 3$.

We define the metric tensor as

$$g^{\mu\nu} = \begin{pmatrix} 1 & 0 & 0 & 0 \\ 0 & -1 & 0 & 0 \\ 0 & 0 & -1 & 0 \\ 0 & 0 & 0 & -1 \end{pmatrix}. \quad (\text{E.1})$$

For the sake of numerical calculation of spinor results we have implemented the Gamma matrices

$$\gamma^0 = \begin{pmatrix} \underline{1} & \underline{0} \\ \underline{0} & -\underline{1} \end{pmatrix}, \quad \gamma^k = \begin{pmatrix} \underline{0} & -\underline{\sigma}^k \\ \underline{\sigma}^k & \underline{0} \end{pmatrix}, \quad (\text{E.2})$$

with properties $(\gamma^0)^\dagger = \gamma^0$, $(\gamma^k)^\dagger = -\gamma^k$, $(\gamma^0)^2 = 1$ and $(\gamma^k)^2 = -1$ based on the conventional definition of Pauli matrices

$$\underline{\sigma}^1 = \begin{pmatrix} 0 & 1 \\ 1 & 0 \end{pmatrix}, \quad \underline{\sigma}^2 = \begin{pmatrix} 0 & -i \\ i & 0 \end{pmatrix}, \quad \underline{\sigma}^3 = \begin{pmatrix} 1 & 0 \\ 0 & -1 \end{pmatrix}. \quad (\text{E.3})$$

Here the matrices

$$\underline{1} \equiv \begin{pmatrix} 1 & 0 \\ 0 & 1 \end{pmatrix} \quad \text{and} \quad (\text{E.4a})$$

$$\underline{0} \equiv \begin{pmatrix} 0 & 0 \\ 0 & 0 \end{pmatrix} \quad (\text{E.4b})$$

are used, the matrices γ^μ are thus four-dimensional.

Finally we require to implement Dirac bispinors normalized to $2m$ as¹

$$u_+^{(1)}(\vec{p}) = \sqrt{E(\vec{p}) + m} \begin{pmatrix} \begin{pmatrix} 1 \\ 0 \end{pmatrix} \\ \frac{\vec{\sigma}\vec{p}}{E(\vec{p}) + m} \begin{pmatrix} 1 \\ 0 \end{pmatrix} \end{pmatrix}, \quad (\text{E.5a})$$

$$u_+^{(1)}(\vec{p}) = \sqrt{E(\vec{p}) + m} \begin{pmatrix} \begin{pmatrix} 0 \\ 1 \end{pmatrix} \\ \frac{\vec{\sigma}\vec{p}}{E(\vec{p}) + m} \begin{pmatrix} 0 \\ 1 \end{pmatrix} \end{pmatrix}. \quad (\text{E.5b})$$

The matrix elements we finally want to evaluate as complex numbers are organized as objects. They provide various functions as for example²

- void square(),
- double sumAndAverageSCALAR(),
- double sumAndAverageSPINOR(),
- double sumAndAverageSquaredSCALARQED(),
- double getPolarizationSCALAR(int epsilonNumber),
- double getSpinResult(int spinIN1, int spinOUT1),
- complex<double> getMatrixElementSPINOR(int spinIN1, int spinOUT1, int polarization, int colourIN1, int colourIN2, int colourOUT1, int colourOUT2, int colourGLUON),

for the inelastic matrix elements specified for the potential model.

These matrix elements keep track of all colour configurations as well as spin arrangements via an array of complex numbers. The arrays, meaning the matrix elements, can easily be summed by the overwritten "+" operator. Generally this allows a powerful handling of a set of diagrams, where the squaring, averaging and summing procedures, a task with a considerable number of nested loops, is actually hidden inside the construction of the matrix element objects. They are to be given the completely determined momenta in order to evaluate the built-in products of Feynman rules. Therefore prepared functions are called, as can be seen in Appendix B. The limits $\epsilon \rightarrow 0$ in Appendix B are not carried out but substituted in the program by $\epsilon = 0$. The colour structure is calculated separately and paired up with the colourless parts afterwards.

¹We do not need v for the calculation.

²We do not discuss this in detail, but mention that the return types are given, the basic meaning of these functions is self-explanatory.

Besides this there are two other groups of functions available. Firstly these are kinematical functions where the remaining moments, given a set of initial conditions, are obtained from, e.g.³

- `int kinematicsPotentialSingleScatteringOneGluonPlus (ContraVector& momIN1, ContraVector& momOUT1, ContraVector& momGLU, ContraVector& momTRANS).`

On the other side the selection of polarization states in different gauges is performed by

- `int getPolarization(string gaugename, ContraVector& epsilon0, ContraVector& epsilon1, ContraVector& gluon, double checkBound),`

as the transformation of polarization states is, too,

- `int changeLinearToCircularPolarization(ContraVector& epsilon0, ContraVector& epsilon1, ContraVector& gluon, double checkBound).`

Parameters which are not supplied to a function are adjusted via an external definition in the main program. Particularly these are the gauge parameter λ for the gluon propagator, a label A^+ , A^- , A^0 as naming of the polarization gauge and for double scattering a whole set of integration parameters. For numerical tests of kinematical, gauge and on-shell conditions additional relative and absolute check boundaries are introduced on a global level.

³The "Plus" in the naming scheme always stands for forward scattering. Most of these function return integers which contain information on the correctness of various checks saying that for a return value "0" no problems were found.

Appendix F Conventions and Notations

At this place we declare and comment on some conventions which are applied throughout this work. General remarks on notations are stated and additional remarks to the numerical calculation are given.

The Feynman diagrams considered here are restricted to tree level processes, thus the coupling $\alpha = g^2/4\pi$ is constant. The radiation amplitude defined in Section 3.2.2 is shown in units of g^2 in our figures, in the calculation this is realized by $g = 1$. The actual though constant value of g does not play a significant role since we only compare different situations for the angular dependence of the radiation amplitude.

Mainly the calculations are carried out using scalar QCD rules since this spin effect can be neglected in the high-energy limit. For the reason to keep the diagrammatic correspondence to spinor QCD the sea gull vertex is not included, of course.

The attentive reader may also question the neglect of exchange diagrams in spinor calculations. However one should keep in mind that we would have a mixture of different preferred light quarks the heavy charm quark is passing and thus we do not focus on effects for identical particles, although we sometimes use equal mass parameters for projectile and target.

We contrast the case of light and heavy quarks. Therefore we usually apply the mass parameters $m_d = 0.007 \text{ GeV}/c^2$ for the down quark and $m_c = 1.5 \text{ GeV}/c^2$ for the charm quark as typical representatives of these two distinct cases.

We work in natural units $c = \hbar = 1$. The sum convention is used, thus expressions have to be summed up over equal indices.

Lorentz indices are denoted by Greek letters μ, ν, σ, \dots

Colour indices are termed in small Latin letters a, b, c, \dots

Capital Latin letters A, B, C, \dots label colour states of the quarks.

With this we follow the conventions in [Wan95].

Appendix G Dead Cone Factor for Arbitrary Angles

In Section 2.2 we have introduced the concept of a suppression factor that can strongly reduce the probability for gluon emission in projectile direction. This factor was given by Dokshitzer and Kharzeev [Dok01] for small angles, see Eq. (2.1), and should correct the matrix elements derived in the approach of Gunion and Bertsch [Gun82], see Appendix D. For completeness we remember that the factor (2.1) is

$$F = \frac{k_{\perp}^2}{k_{\perp}^2 + \omega^2 \theta_0^2} = \frac{\sin^2 \theta}{\sin^2 \theta + \theta_0^2}, \quad (\text{G.1})$$

where $\theta_0 = m/E$, m indicates the mass and E the energy of the incident heavy projectile quark.

This appendix is intended to offer insight how the dead cone factor arises technically. It aims to present a simple derivation of this factor for arbitrary emission angles.

Correction Factor for Arbitrary Angles for the Pre-Projectile Emission Diagram

In general, the dead cone effect arises from the screening of a divergence due to a non-zero mass parameter in the corresponding propagator. Within the considered contributions to one gluon emission, Fig. D.4, there is the internal propagator of the exchanged gluon which remains massless and causes a divergence in quark-quark scattering. The internal quark propagator, however, yields a divergent matrix element only in the Gunion and Bertsch approach of massless quarks [Gun82]. For the case of the pre-emission process, Fig. D.4(a), we present a derivation of the dead cone factor.

We rewrite the pre-projectile matrix element Eq. (D.8)

$$M_{\text{prePro}}^{\text{scalar}} = C_{\text{prePro}} \cdot ig^3 \frac{(p_f + p_i - k)(p'_f + p'_i) \cdot (2p_i - k)\epsilon}{[(p_i - k)^2 - m^2] \cdot (p'_f - p'_i)^2} \quad (\text{G.2})$$

in order to obtain the correction factor

$$M_{\text{prePro}}^{\text{scalar}} = C_{\text{prePro}} \cdot ig^3 \left(-\frac{p_i \epsilon}{p_i k} \right) \left(\frac{(p_f + p_i)(p'_f + p'_i)}{(p'_f - p'_i)^2} - \frac{k(p'_f + p'_i)}{(p'_f - p'_i)^2} \right). \quad (\text{G.3})$$

The on-shell conditions $p_i^2 = m^2$, $k^2 = 0$ and the Lorentz condition $\epsilon k = 0$ are applied, thus the elastic matrix element Eq. (D.2)

$$M_{\text{elastic}}^{\text{scalar}} = C_{\text{elastic}} \cdot ig^2 \frac{(p_f + p_i)(p'_f + p'_i)}{(p'_f - p'_i)^2} \quad (\text{G.4})$$

can be substituted if the four momentum of the gluon is negligible in the kinematical calculation, that is to say the final momenta of the quarks are assumed to be identical in the inelastic as well as in the elastic scattering situation

$$\frac{M_{\text{prePro}}^{\text{scalar}}}{M_{\text{elastic}}^{\text{scalar}}} = \frac{C_{\text{prePro}}}{C_{\text{elastic}}} \cdot g \left(-\frac{p_i \epsilon}{p_i k} \right) \left(1 - \frac{k(p'_f + p'_i)}{(p_f + p_i)(p'_f + p'_i)} \right). \quad (\text{G.5})$$

We use light-cone coordinates and express the polarisation vectors in A^+ -gauge

$$k = \left[2px, \frac{k_{\perp}^2}{2px}, \vec{k}_{\perp} \right], \quad (\text{G.6})$$

$$\epsilon = \left[0, \frac{\vec{\epsilon}_{\perp} \vec{k}_{\perp}}{xp}, \vec{\epsilon}_{\perp} \right]. \quad (\text{G.7})$$

An expansion in the mass of the projectile is carried out

$$p_i = \left(\sqrt{p^2 + m^2}, 0, 0, p \right) \approx \left(p + \frac{m^2}{2p}, 0, 0, p \right), \quad (\text{G.8})$$

$$p_i = [p_0 + p_z, p_0 - p_z, \vec{p}_{\perp}] \approx \left[2p, \frac{m^2}{2p}, \vec{0}_{\perp} \right]. \quad (\text{G.9})$$

The suppression factor follows from the part $\frac{p_i \epsilon}{p_i k}$. In the Gunion and Bertsch approach for $m = 0$

this yields the term $\frac{2\vec{\epsilon}_{\perp} \vec{k}_{\perp}}{k_{\perp}^2}$ and the second bracket in the factorised matrix element in Eq. (G.5) corresponds to the term $(1 - x)$. This is not calculated here but for a non-zero mass there are additional corrections in this part. Note, that a similar factorisation is possible using spinor rules which yield the same result for the suppression factor [Wan95].

$$\frac{p_i \epsilon}{p_i k} = \frac{2\vec{\epsilon}_{\perp} \vec{k}_{\perp}}{k_{\perp}^2 + x^2 m^2} \quad (\text{G.10})$$

Hence the Gunion and Bertsch matrix element has to be corrected by a factor

$$F = \frac{k_{\perp}^2}{k_{\perp}^2 + x^2 m^2} = \frac{\sin^2 \theta}{\sin^2 \theta + \theta_0^2 \left(\frac{1 + \cos \theta}{2} \right)^2} = \frac{\sin^2 \theta}{\sin^2 \theta + \theta_0^2 \cdot \cos^4(\theta/2)}. \quad (\text{G.11})$$

Furthermore, only the momentum of the initial projectile is chosen, that means the results for this diagram are not restricted to a specific Lorentz frame, which accounts for the fact that numerical results in CMS and in LAB frame are in agreement with the dead cone correction factor.

Finally, this factor shows the missing symmetry between forward and backward emission of the gluon. For small angles in forward direction it reduces to the factor of Dokshitzer and Kharzeev, on the contrary, for angles $\theta \rightarrow \pi$ the Gunion and Bertsch result ($F \rightarrow 1$) is reproduced.

The effect of this dead cone factor on the radiation amplitude depends of course on all other possible diagrams. The same form of this suppression factor can be found in the post-emission and in the three-gluon contribution only for specific kinematical situations. The interplay of different contributions is a main subject of Chapter 4.

Appendix H Scalar versus Spinor Calculation

In this thesis the discussion of radiation amplitudes was mainly concerned with results obtained from scalar Feynman rules. However the program package is organized to deal with spinor rules as well. Although we do not present this in detail, comparisons of both calculation methods were in agreement if light particles with high energies, small momentum transfers and soft radiation were assumed. Thus the program allows further investigations into effects of spins.

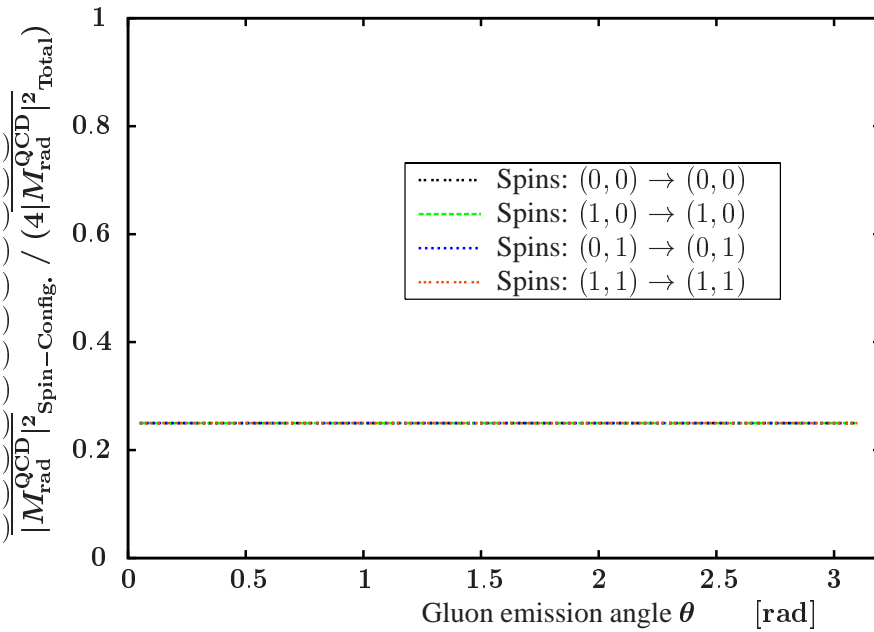


Figure H.1: Relative contributions from different spin configurations to the summed and averaged squared matrix element for gluon emission in the scattering of two down quarks from spinor QCD as a function of the emission angle θ . The non-vanishing contributions fall together. The parameters are $m_1 = m_2 = m_d = 0.007$ GeV, $\vec{p}_1 = (0, 0, 5)$ GeV, $\vec{p}_2 = (0, 0, -5)$ GeV, $\omega = 0.001$ GeV, $\theta = 0 \dots \pi$, $\phi = \pi/2$, $\vec{q}_\perp = (0, 0.01)$ GeV, $\sqrt{s} = 10$ GeV.

Exemplary we present results for spin flip effects in the process of single scattering with one-gluon emission. In Figs. H.1 and H.2 therefore the relative contributions from different spin configurations to the total squared and averaged matrix element are displayed as a function of the gluon emission angle θ . For the case of two equally light quarks in CMS, Fig. H.1, one finds four non-vanishing contributions with the same weight. They correspond to spin configurations where no spin is changed. In general there are sixteen different possibilities for spin configurations of initial and

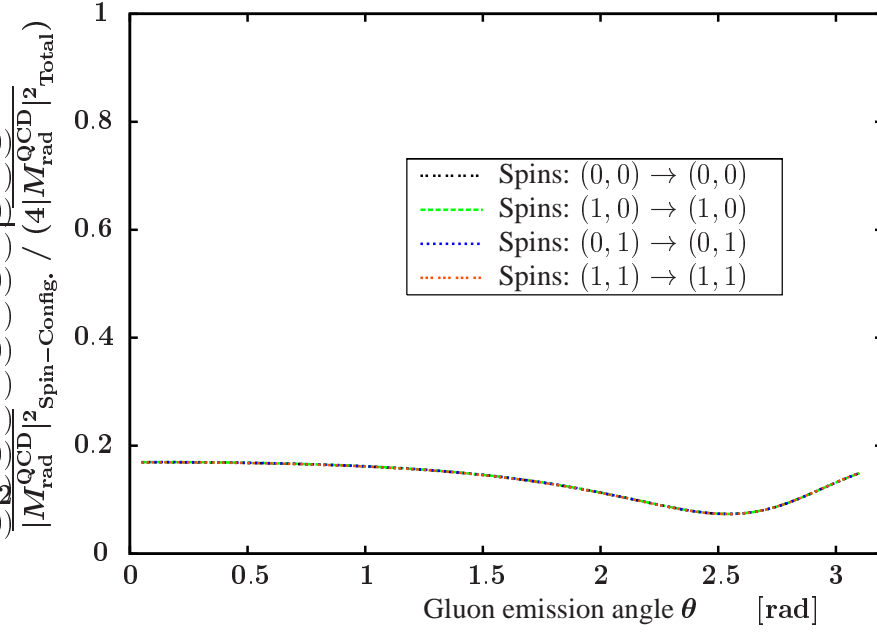
final states of two quarks, which are denoted by

$$(\text{initial projectile spin, initial target spin}) \rightarrow (\text{final projectile spin, final target spin}).$$

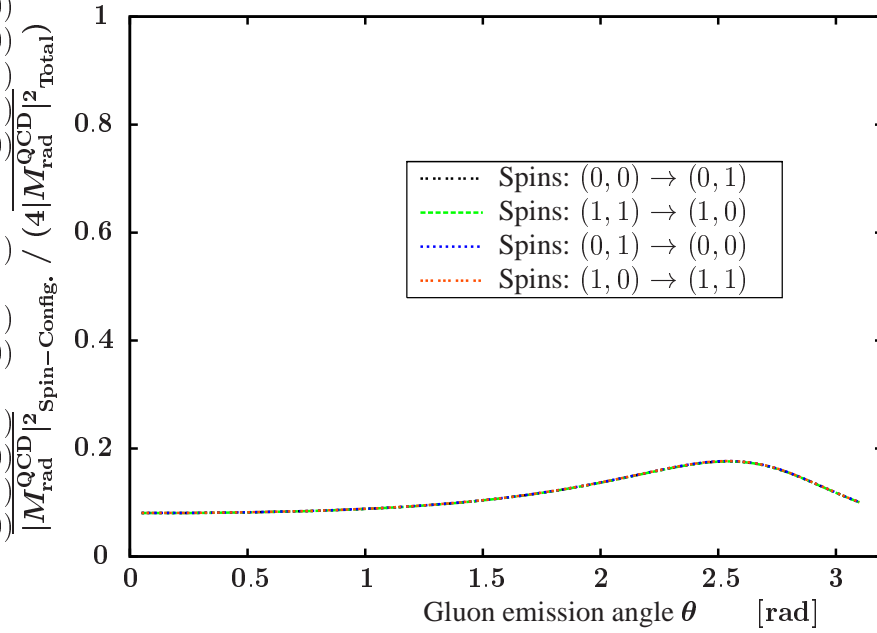
The distinct spin states of each particle are termed with arbitrary numbers 0 and 1. Note that the factor 4 in the denominator of the displayed ratios is due to the average over initial spins and is required to ensure that the sum of all ratios equals 1.

In Fig. H.2 we exhibit the non-vanishing contributions in the case that a heavy projectile scatters on a light target at rest. Besides configurations where the spins are not changed, Fig. H.2(a), also situations with one spin being modified become relevant. This is depicted in Fig. H.2(b). Moreover this calculation shows, that only configurations where the spin of the light target is changed are non-zero.

In closing, we have seen that as in our second case spin effects may be important for the emission processes of gluons. Note for example there appears an angular dependence in Fig. H.2, which remains a question to further investigation. This second case is closely related to the calculation in Section 4.5 for Fig. 4.30(a), thus possible improvements of the potential model should be contrasted with spin effects.



(a) Configurations where no spin is changed.



(b) Configurations where the spin of the target is changed.

Figure H.2: Relative contributions from different spin configurations to the summed and averaged squared matrix element for gluon emission in the scattering of a heavy on a light quark from spinor QCD as a function of the emission angle θ . The non-vanishing contributions in each plot fall together. The parameters are $m_1 = m_c = 1.5$ GeV, $m_2 = m_d = 0.007$ GeV, $\vec{p}_1 = (0, 0, 5)$ GeV, $\vec{p}_2 = (0, 0, 0)$ GeV, $\omega = 0.001$ GeV, $\theta = 0 \dots \pi$, $\phi = \pi/2$, $\vec{q}_\perp = (0, 0.01)$ GeV, $\sqrt{s} = 1.524$ GeV.

Bibliography

- [Adc02a] K. Adcox *et al.* [PHENIX Collaboration], Phys. Rev. Lett. **88** (2002) 022301.
- [Adc02b] K. Adcox *et al.* [PHENIX Collaboration], Phys. Rev. Lett. **88** (2002) 192303.
- [Adc03] K. Adcox *et al.* [PHENIX Collaboration], Phys. Lett. B **561** (2003) 82.
- [Adl03] S.S. Adler *et al.* [PHENIX Collaboration], Phys. Rev. Lett. **91** (2003) 072301.
- [App86] D. A. Appel, Phys. Rev. D **33** (1986) 717.
- [Bai95] R. Baier, Y.L. Dokshitzer, S. Peigne, D. Schiff, Phys. Lett. B **345** (1995) 277.
- [Bai96] R. Baier, Y.L. Dokshitzer, A.H. Mueller, S. Peigne, D. Schiff, Nucl. Phys. B **478** (1996) 577.
- [Bai97a] R. Baier, Y.L. Dokshitzer, A.H. Mueller, S. Peigne, D. Schiff, Nucl. Phys. B **483** (1997) 291.
- [Bai97b] R. Baier, Y.L. Dokshitzer, A.H. Mueller, S. Peigne, D. Schiff, Nucl. Phys. B **484** (1997) 265.
- [Bai98a] R. Baier, Y.L. Dokshitzer, A.H. Mueller, D. Schiff, Phys. Rev. C **58** (1998) 1706.
- [Bai98b] R. Baier, Y.L. Dokshitzer, A.H. Mueller, D. Schiff, Nucl. Phys. B **531** (1998) 403.
- [Bai98c] V.N. Baier, V.M. Katkov, V.M. Strakhovenko, *Electromagnetic processes at high energies in oriented single crystals*, World Scientific, Singapore, 1998.
- [Bai99] R. Baier, Y.L. Dokshitzer, A.H. Mueller, D. Schiff, Phys. Rev. C **60** (1999) 064902.
- [Bai00] R. Baier, D. Schiff, B.G. Zakharov, Ann. Rev. Nucl. Part. Sci. **50** (2000) 37.
- [Bai01a] R. Baier, Y.L. Dokshitzer, A.H. Mueller, D. Schiff, Phys. Rev. C **64** (2001) 057902.
- [Bai01b] R. Baier, Y.L. Dokshitzer, A.H. Mueller, D. Schiff, JHEP **0109** (2001) 033.
- [Bai03] R. Baier, Nucl. Phys. A **715** (2003) 209.
- [Bar01] H.W. Barz, B. Kämpfer, Nucl. Phys. A **683** (2001) 594.
- [Bjo90] J. D. Bjorken, S. D. Drell, *Relativistische Quantenfeldtheorie*, Wissenschaftsverlag, Mannheim, 1990.
- [Bla86] J.P. Blaizot, L.D. McLerran, Phys. Rev. D **34** (1986) 2739.

- [Djo03a] M. Djordjevic, M. Gyulassy, Phys. Lett. B **560** (2003) 37.
- [Djo03b] M. Djordjevic, M. Gyulassy, nucl-th/0305062.
- [Dok01] Y.L. Dokshitzer and D. E. Kharzeev, Phys. Lett. B **519** (2001) 199.
- [Dok03] Y.L. Dokshitzer, G. Marchesini, JHEP **0303** (2003) 040.
- [Gal64] V.M. Galitzky, I.I. Gurevich, Nuovo Cimento **32** (1964) 1820.
- [Gal03] K. Gallmeister, B. Kämpfer, O.P. Pavlenko, Nucl. Phys. A **715** (2003) 705.
- [Gun82] J. F. Gunion, G. Bertsch, Phys. Rev. D **25** (1982) 746.
- [Gyu94] M. Gyulassy, X.N. Wang, Nucl. Phys. B **420** (1994) 583.
- [Gyu99] M. Gyulassy, P. Levai, I. Vitev, Nucl. Phys. A **661** (1999) 637.
- [Gyu00a] M. Gyulassy, P. Levai, I. Vitev, Nucl. Phys. B **571** (2000) 197.
- [Gyu00b] M. Gyulassy, P. Levai, I. Vitev, Phys. Rev. Lett. **85** (2000) 5535.
- [Gyu01] M. Gyulassy, P. Levai, I. Vitev, Nucl. Phys. B **594** (2001) 371.
- [Gyu01b] M. Gyulassy, I. Vitev, X.N. Wang, Phys. Rev. Lett. **86** (2001) 2537.
- [Gyu02a] M. Gyulassy, P. Levai, I. Vitev, Phys. Rev. D **66** (2002) 014005.
- [Gyu02b] M. Gyulassy, P. Levai, I. Vitev, Phys. Lett. B **538** (2002) 282.
- [Gyu03] M. Gyulassy, I. Vitev, X.N. Wang, B.W. Zhang, nucl-th/0302077, to appear in *Quark Gluon Plasma 3*, editors: R.C. Hwa, X.N. Wang, World Scientific, Singapore, 2003.
- [Han01] S. Hands, Contemp. Phys. **42** (2001) 209.
- [Hic03] K.H. Hicks, talk at "Masses of Hadrons" course, Bad Honnef, 2003.
- [Hua92] K. Huang, *Quarks, Leptons and Gauge Fields, 2nd ed.*, World Scientific, Singapore, 1992.
- [Jac98] J.D. Jackson, *Classical electrodynamics, 3rd ed.*, Wiley, New York, 1998.
- [Käm00] B. Kämpfer, O.P. Pavlenko, Phys. Lett. B **477** (2000) 171.
- [Kra02] F. Krauss, R. Kuhn, G. Soff, JHEP **0202** (2002) 044.
- [Kov01] A. Kovner, U.A. Wiedemann, Phys. Rev. D **64** (2001) 114002.
- [Kov03] A. Kovner, U.A. Wiedemann, hep-ph/0304151, to appear in *Quark Gluon Plasma 3*, editors: R.C. Hwa, X.N. Wang, World Scientific, Singapore, 2003.
- [Lan80] L. D. Landau, E. M. Lifschitz, Lehrbuch der Theoretischen Physik, Vol. 4, *Relativistische Quantentheorie*, Akademie-Verlag, Berlin, 1980.
- [Lev02] P. Levai, G. Papp, G. Fai, M. Gyulassy, G.G. Barnafoldi, I. Vitev, Y. Zhang, Nucl. Phys. A **698** (2002) 631.

- [Mol01] D. Molnar, "*Datong 2001, Multiparticle dynamics*", 211.
- [Mül99] W. Müller, "*Untersuchungen zum Landau-Pomeranchuk-Migdal-Effekt in QED und QCD*", Diplomarbeit, Dresden, 1999.
- [Mül03] B. Müller, Phys. Rev. C **67** (2003) 061901.
- [Pav97] O.P. Pavlenko, copies of a talk at the Forschungszentrum Rossendorf, 1997.
- [QM02] *Quark Matter 2002, proceedings*, editors: H. Gutbrod, J. Aichelin, K. Werner, Nucl. Phys. A **715** (2003) 1.
- [Sal03] C.A. Salgado, U.A. Wiedemann, Phys. Rev. D **68** (2003) 014008.
- [Ter72] M.L. Ter-Mikaelian, *High-energy electromagnetic processes in condensed media*, Wiley, New York, 1972.
- [Tit99] A.I. Titov, B. Kämpfer, Phys. Rev. C **59** (1999) 999.
- [Wan92] X.N. Wang, M. Gyulassy, Phys. Rev. Lett. **68** (1992) 1480.
- [Wan95] X.N. Wang, M. Gyulassy, M. Plümer, Phys. Rev. D **51** (1995) 3436.
- [Wan01a] X.N. Wang, Phys. Rev. C **63** (2001) 054902.
- [Wan01b] E. Wang, X.N. Wang, Phys. Rev. Lett. **87** (2001) 142301.
- [Wan02] E. Wang, X.N. Wang, Phys. Rev. Lett. **89** (2002) 162301.
- [Wed00] S. Wedner, "*Verifizierte Bestimmung singulärer Integrale - Quadratur und Kubatur*", Dissertation, Karlsruhe, 2000.
- [Wie99] U.A. Wiedemann, M. Gyulassy, Nucl. Phys. B **560** (1999) 345.
- [Wie00a] U.A. Wiedemann, Nucl. Phys. B **582** (2000) 409.
- [Wie00b] U.A. Wiedemann, Nucl. Phys. B **588** (2000) 303.
- [Wie01] U.A. Wiedemann, Nucl. Phys. A **690** (2001) 731.
- [Wie02a] U.A. Wiedemann, Nucl. Phys. A **698** (2002) 615.
- [Wie02b] U.A. Wiedemann, talk at "Strong and Electroweak Matter" workshop, Heidelberg, 2002, hep-ph/0302194.
- [Won94] C.Y. Wong, *Introduction to High-Energy Heavy-Ion Collisions*, World Scientific, Singapore, 1994.
- [Yak89] S. Yakowitz, F. Szidarovszky, *An Introduction to Numerical Computations, 2nd ed.*, Macmillan, New York, 1989.
- [Zak98] B.G. Zakharov, Phys. Atom. Nucl. **61** (1998) 838, Yad. Fiz. **61** (1998) 924.
- [Zak01] B.G. Zakharov, JETP Lett. **73** (2001) 49.

Declaration/Selbständigkeitserklärung

I declare, that I have written this diploma thesis on my own without the help of others and without using further not named help. All statements taken from the work of others either directly or indirectly are explicitly referenced. This work has not been submitted for any other qualification.

Hiermit erkläre ich, die vorliegende Arbeit selbständig ohne unzulässige Hilfe Dritter und ohne Benutzung anderer nicht angegebener Hilfsmittel angefertigt zu haben. Alle Gedanken, die aus Quellen direkt oder indirekt übernommen wurden, sind als solche gekennzeichnet. Diese Arbeit wurde noch keiner anderen Prüfungsbehörde vorgelegt.

Dresden, 27.11.2003

Acknowledgements

I thank my supervisors Prof. Dr. Gerhard Soff and Prof. Dr. Burkhard Kämpfer for continuous support and their helpful comments on the presentation of these results. I am grateful to Prof. Dr. Burkhard Kämpfer for expert guidance while I was working on this topic. The discussions I had with him and with O.P. Pavlenko were very helpful. I also thank Prof. Dr. Gerhard Soff and the group "Theory of hadrons and nuclei" for discussions as well as the whole Institute for Theoretical Physics for the pleasant working atmosphere. The excellent conditions of work, which are also due to the Forschungszentrum Rossendorf, are gratefully acknowledged.